Charge separation and recombination in novel polymeric absorber materials for organic solar cells – a photophysical study

JOHANNES GUTENBERG
UNIVERSITÄT MAINZ

Dissertation
zur Erlangung des Grades
"Doktor der Naturwissenschaften"
im Promotionsfach Chemie
am Fachbereich Chemie, Pharmazie und Geowissenschaften
der Johannes Gutenberg-Universität
in Mainz

Hannah Mangold
geboren in Geislingen/Steige

Oktober 2013

Hannah Mangold

Charge separation and recombination in novel polymeric absorber materials

SUMMARY

This thesis presents an investigation of charge carrier generation and recombination processes in novel polymeric absorber materials for organic solar cells. The understanding of these processes is essential for the development of new photoactive material systems that achieve higher power conversion efficiencies and enable organic solar cells to become a competitive renewable energy technology. The main experimental technique used in this thesis is transient absorption spectroscopy, a powerful technique to study photophysical processes on the 100 fs to 1 ms timescale. We introduce a soft-modeling technique which aids the determination of the photophysical processes from the observed transient absorption data matrix in general cases where little a priori knowledge of reaction kinetics is available. Three different donor:acceptor systems are investigated; each of these systems represents a different approach to optimize materials in terms of light absorption over a broad wavelength range, efficient free charge carrier generation and fast charge carrier transport. In the first system, we investigate a terpolymer comprised of separate units for light absorption and charge carrier transport. We demonstrate that it is possible to guide excited-state flow from the chromophore onto the transport unit. In the second part, the influence of crystallinity on free charge carrier generation is investigated with a series of ternary blends containing different amounts of amorphous and semi-crystalline polymer. We find that both the amount of geminate charge recombination is enhanced and non-geminate recombination is faster with increasing amorphous polymer content. Finally, we investigate a system where both donor and acceptor material are polymers, leading to enhanced light absorption properties. Sub 100 ps charge-transfer state recombination is the dominant loss mechanism in this system, as free charge carriers can only be generated at interfaces where donor and acceptor polymer are oriented face-to-face relative to each other. Moreover, we observe that another 40–50% of the charge carriers are lost through recombination of interfacial states geminately reformed from mobile charge carriers.

Hannah Mangold

Ladungstrennung und -rekombination in polymeren Absorbermaterialien

ZUSAMMENFASSUNG

In dieser Dissertation wird die Ladungsträgergeneration und -rekombination in neuen polymeren Absorbermaterialien für organische Solarzellen untersucht. Das Verständnis dieser Prozesse ist wesentlich für die Entwicklung neuer photoaktiver Materialsysteme, die hohe Effizienzen erzielen und organische Solarzellen konkurrenzfähig im Bereich der erneuerbaren Energien machen. Experimentell verwendet diese Arbeit hauptsächlich die Methode der transienten Absorptionsspektroskopie, die sich für die Untersuchung photophysikalischer Prozesse auf einer Zeitskala von 100 fs bis 1 ms als sehr leistungsfähig erweist. Des Weiteren wird eine *soft-modeling* Methode vorgestellt, die es ermöglicht, photophysikalische Prozesse aus einer gemessenen transienten Absorptions-Datenmatrix zu bestimmen, wenn wenig *a priori* Kenntnisse der Reaktionskinetiken vorhanden sind. Drei unterschiedliche Donor:Akzeptor-Systeme werden untersucht; jedes dieser Systeme stellt eine andere Herangehensweise zur Optimierung der Materialien dar in Bezug auf Lichtabsorption über einen breiten Wellenlängenbereich, effiziente Ladungstrennung und schnellen Ladungstransport. Zuerst wird ein Terpolymer untersucht, das aus unterschiedlichen Einheiten für die Lichtabsorption und den Ladungstransport besteht. Es wird gezeigt, dass es möglich ist, den Fluss angeregter Zustände vom Chromophor auf die Transporteinheit zu leiten. Im zweiten Teil wird der Einfluss von Kristallinität auf die freie Ladungsträgergeneration mit einer Folge von ternären Mischungen, die unterschiedliche Anteile an amorphem und semi-kristallinem Polymer enthalten, untersucht. Dabei zeigt es sich, dass mit steigendem amorphen Polymeranteil sowohl der Anteil der geminalen Ladungsträgerrekombination erhöht als auch die nicht-geminale Rekombination schneller ist. Schlussendlich wird ein System untersucht, in dem sowohl Donor als auch Akzeptor Polymere sind, was zu verbesserten Absorptionseigenschaften führt. Die Rekombination von Ladungstransferzuständen auf der unter 100 ps Zeitskala stellt hier den hauptsächliche Verlustkanal dar, da freie Ladungsträger nur an Grenzflächen erzeugt werden können, an denen Donor und Akzeptor *face-to-face* zueinander orientiert sind. Darüberhinaus wird festgestellt, dass weitere 40–50% der Ladungsträger durch die Rekombination von Grenzflächenzuständen verloren gehen, die aus mobilen Ladungsträgern geminal gebildet werden.

This dissertation is the result of my own work carried out at the Max Planck Insitute for Polymer Research, Mainz between October 2010 and October 2013. I hereby declare that I wrote this dissertation submitted without any unauthorized external assistance and used only sources acknowledged in the work. Nevertheless, I will write in the first person plural instead of singular (we instead of I) to make the text more readable. In carrying out this research, I complied with the rules of standard scientific practice as formulated in the statutes of the Johannes Gutenberg-University Mainz to insure standard scientific practice. This dissertation has not been submitted in whole or in part for the award of a degree at this or any other university.

Hannah Mangold

Contents

List of Figures

LIST OF FIGURES

Chapter 1

Introduction

Recently, the Intergovernmental Panel on Climate Change (IPCC) published an update on the scientific knowledge about climate change. It is now clear that global warming is unequivocal and it is *extremely likely* that human influence is the dominant cause for it.[1] With fossil fuel sources becoming depleted at the same time, renewable sources of energy need to be developed to meet the global energy consumption and decrease carbon dioxide levels. Harvesting solar energy is a promising way to do this, however, until now its potential has not been fully exploited, as electricity generated from photovoltaic technologies accounts for only about 0.1% of total energy generation worldwide,[2] and 1.1% in Germany.[3] So far, inorganic materials (mainly silicon, but also GaAs, CdTe and CIGS) are used in commercially available photovoltaic devices. They can achieve power conversion efficiencies exceeding 20% and exhibit long lifetimes. However, their production process is expensive and energy intensive. Organic solar cells are a promising emerging photovoltaic technology as they are unrivaled in terms of their processing cost and speed.[4, 5] Other advantages include the possibility of producing lightweight and flexible solar cell modules which, for instance, enables their application in portable electronic devices.[6] Moreover, as organic solar cells are semi-transparent and their color can be varied, they could be used in building-integrated photovoltaics, where large windows could be coated with the solar cells and thus used for power generation.[7] Record efficiencies of >9% for single junction solar cells [8] and >10% for tandem solar cells [9] have been achieved.

However, in terms of commercialization, large-scale production and long-term stability is still an issue.

The design and synthesis of new photoactive materials is the major force driving the improvement of organic solar cells at present. A suitable solar cell material should absorb a large amount of the incoming photons, and convert them into electrons that can be extracted into an external circuit. At the same time, the optical energy of the incoming light should be retained in the electrical energy of the electrons. It follows from these requirements that different parameters need to be engineered in order to enhance the efficiency. These include enhanced light absorption properties, improved energy levels and higher charge carrier mobilities.[10, 11] Moreover, achieving an optimum morphology of the photoactive layer is pivotal for device performance. In order to be able to improve the materials in a systematic fashion and control the resulting solar cell properties, it is vital to understand the fundamental processes in an organic solar cell and to establish structure-function relationships. A powerful method to do this is transient absorption spectroscopy as it covers the complete time range from 100 fs to 1 ms, when processes of charge carrier generation and recombination take place.[12] Thus it is possible to track and understand excited-state flow in a given material system and correlate the charge generation efficiency with the physical properties of the material used.

This thesis aims to provide a more detailed understanding of the charge carrier generation and recombination processes in organic solar cells. Several ways to improve absorption properties and engineer excited-state flow and thus enhance the power conversion efficiency of an organic solar cell are investigated. Three different material systems, each with a particular approach to improve the photoactive material properties for free charge carrier generation, are investigated in terms of the processes happening after light absorption and leading to charge carrier extraction (and thus photocurrent generation) or charge carrier recombination (and thus charge carrier loss).

To start with, Chapter 2 provides a brief review of the theoretical background needed to understand the photophysical processes in conjugated polymers and in organic solar cells. It then introduces ultrafast spectroscopy and finally offers a

detailed description of transient absorption data analysis methods. The experimental methods used in this thesis are briefly reviewed in Chapter 3. Chapter 4 examines a set of polymeric donor materials which were designed to separate light absorption and transport properties onto different monomer units and thus enable step-wise material optimization. It further demonstrates that guiding excited-state flow along the polymer backbone is possible. Chapter 5 presents an investigation of the influence of crystallinity on free charge carrier generation. By increasing the amount of amorphous polymer in an amorphous/semi-crystalline donor polymer mixture, the amount of geminate charge carrier recombination is increased which leads to lower quantum efficiencies. Finally, Chapter 6 shows a detailed analysis of charge generation and recombination in a blend system, wherein both donor and acceptor material are conjugated polymers. Here, the morphology of the heterojunction interface determines the amount of fast charge-transfer state recombination. Moreover, further charge carriers are lost through recombination of interfacial states geminately reformed from mobile charge carriers. The thesis closes with Chapter 7, where the results are summarized and an outlook with suggestions for further work is presented.

Chapter 2

Background

2.1 Optical and electronic properties of conjugated polymers

2.1.1 Conjugated π-bonds

The Nobel prize for chemistry in 2000 was awarded to A.J. Heeger, A.G. Mc Diarmid and H. Shirakawa "for the discovery and development of conductive polymers" [13]. Since their discovery of conductivity in doped polyacetylene in 1977 [14], much research has gone into finding new types of optoelectronically active polymers and developing them to be suitable for applications such as organic field effect transistors (OFETs), organic light emitting diodes (OLEDs) and organic solar cells (OSCs). The characteristic feature of semiconducting polymers is a conjugated π-system of sp^2-hybridized carbon atoms with one electron in the p_z-orbital of each carbon atom. Whereas the sp^2-orbitals form localized σ-bonds that have a large energetic difference between bonding and anti-bonding orbital, the electrons in the p_z-orbital form π-bonds that are delocalized in the orthogonal plane to the σ-bonds. The longer the conjugation length of a molecule is, the smaller the energy difference between highest occupied molecular orbital (HOMO) and lowest unoccupied molecular orbital (LUMO) gets (see figure 2.1). However, the delocalization of the π-electrons in a conjugated polymer is limited by chemical chain defects, kinks, and twists which make the effective conjuga-

tion length much shorter than the polymer chain length, typically around 5 to 15 monomer units.[15] This means that the polymers behave as semiconductors. Even in the ideal case of infinitely long conjugation length a band-gap would remain due to the Peierls distortion: One-dimensional metals are unstable with respect to distortion and therefore an energy gap opens at the Fermi level leading to semiconducting behavior.[16]

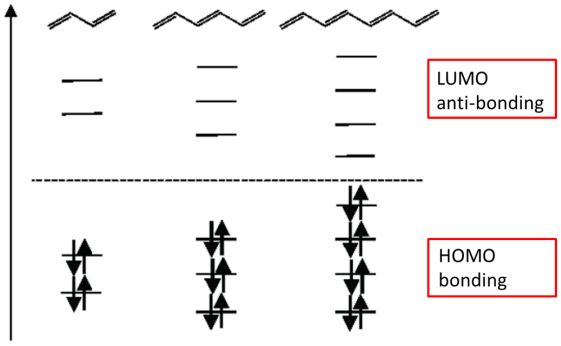

Figure 2.1: As the conjugation length gets longer, the gap between HOMO and LUMO gets smaller and more energy levels are formed converging eventually in the case of a polymer into continuous bands, however still separated by a band-gap.

2.1.2 Excited states in conjugated polymers

Upon excitation of a conjugated polymer an electron is promoted from the HOMO into the LUMO. However, this electron and the corresponding hole are still bound due to the Coulombic force. This state is called an exciton, from the combination of '**excit**ation' and 'on', Greek for particle. Three different kinds of excitons are distinguished depending on the extent of their delocalization (see figure 2.2): Frenkel excitons are localized on small molecules or conjugated segments of a polymer chain; Mott-Wannier excitons on the contrary, are highly delocalized and exist mainly in inorganic semiconductors. In charge-transfer excitons the charge carriers are located on two adjacent sites, be it on the same polymer chain or on neighboring molecules. Excitons can be further distinguished by the

orientation of the spins of their charge carriers. If the spins are anti-parallel, the total spin is 0 and they are termed singlet excitons, if the spins are parallel, the total spin is 1 and they are termed triplet excitons.

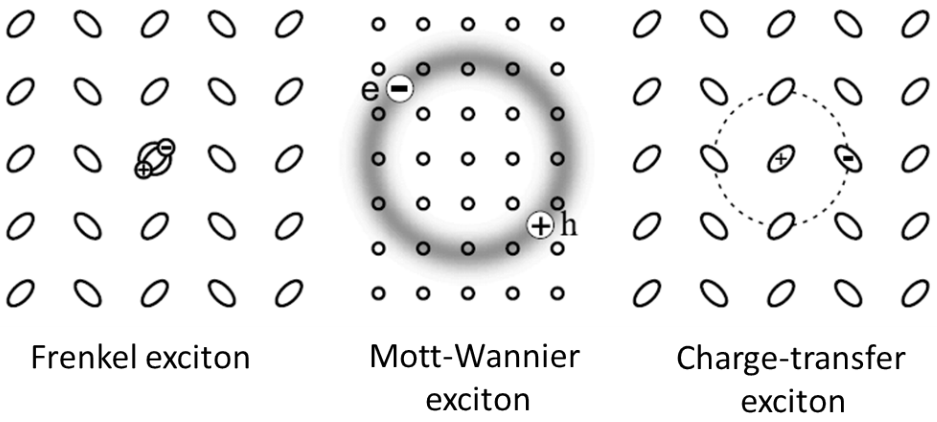

Figure 2.2: Frenkel excitons possess radii comparable to the inter-site distance, whereas the radii are much larger for Mott-Wannier excitons; charge-transfer excitons are in between. Reproduced from [17, p. 150] with permission.

Conjugated polymer chains can also have charged excitation states that are formed by adding or taking away an electron. These states are termed polarons, they consist of not only the charge itself but also a deformation of the molecular structure as surrounding atomic nuclei are displaced by the charge.

A more detailed review of excited states in conjugated polymers can be found in [17–19].

2.1.3 Optical processes

Learning about excited states in molecules is best done by probing them with light, i.e. doing spectroscopy (from Latin *spectrum*=image and Greek *skopein*=to look), this will be dealt with in chapter 2.3. To understand spectroscopical results we need to understand the interaction of light and matter, such as absorption and emission and also subsequent processes, such as energy transfer.

2.1.3.1 Light absorption

Optical absorption takes place when a transition between symmetry-allowed electronic states is possible and the energy of the absorbed photon is equal to the energy difference between these states. The intensity of this transition can be calculated taking into account the Franck-Condon principle. This principle assumes that the electronic transition occurs so rapidly (on the timescale of 10^{-15} s) that the nuclei do not change their position during the transition (the timescale of a vibration being 10^{-12}-10^{-10} s). Therefore an electron which is in the lowest vibronic level of the ground state might be promoted into a higher vibronic level of the excited state, as illustrated in figure 2.3(a), depending on the structure of the excited state.

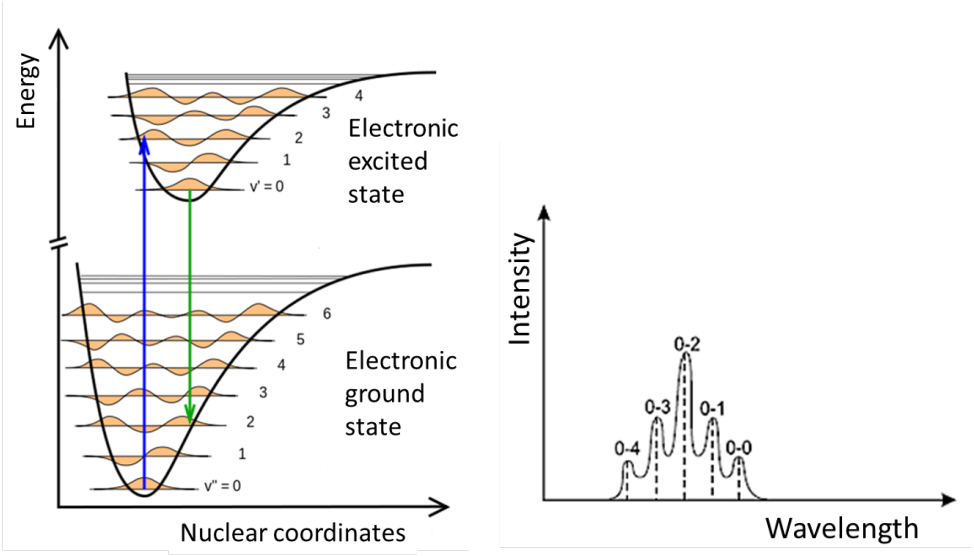

(a) (b)

Figure 2.3: Panel (a) shows the potential energy diagram of electronic ground and excited state and their vibrational modes as a function of nuclear distance with the arrows indicating possible transitions. Panel adapted from [20]. Panel (b) shows a schematic of a corresponding absorption diagram.[21, p. 32]

The transition probability P_{ul} between the states u (upper) and l (lower) can

be described as the following product:

$$P_{ul} \propto \left|\left\langle \Psi_u|\vec{M}|\Psi_l \right\rangle\right|^2 \cdot |\langle\chi_u|\chi_l\rangle|^2 \cdot |\langle S_u|S_l\rangle|^2 \tag{2.1}$$

The individual terms of this product describe the selection rules for allowed and forbidden electronic transitions. Four types of selection rules can be distinguished:

- $\left|\left\langle \Psi_u|\vec{M}|\Psi_l \right\rangle\right|$ must have an even symmetry ("gerade") to obtain a non-zero integral. As the dipole moment operator $\vec{M}$ is an odd operator, Ψ_u and Ψ_l must be of opposite parity, i.e. one being *gerade* the other *ungerade*.
- Ψ_u and Ψ_l need to have spatial overlap, the magnitude of the transition probability depends on the overlap of the orbital functions.
- The factor $|\langle\chi_u|\chi_l\rangle|^2$ relates to the Franck-Condon principle discussed above and describes the excitation probability of a vibronic transition.
- $|\langle S_u|S_l\rangle|^2$ describes the conservation of spin which is necessary for a transition to occur, i.e. transitions between pure singlet and triplet states are strictly forbidden.

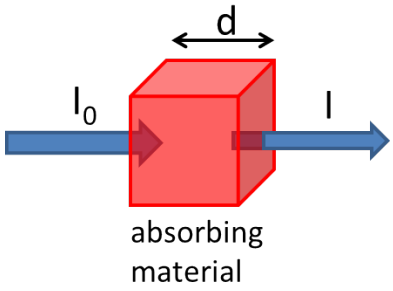

Figure 2.4: Schematic diagram illustrating the absorption of light passing through a material.

Experimentally we measure the transmission of light through a sample (see figure 2.4). Making the assumptions that no light is scattered by the material,

non-linear processes do not occur and emission in the direction of transmission is negligible, we can calculate the amount of absorbed light. The change in light intensity can be described by

$$dI_\omega = -\alpha_\omega(z)dz \tag{2.2}$$

giving the Lambert-Beer law:

$$I = I_0 e^{-\alpha d} \tag{2.3}$$

where α is the absorption coefficient and d the distance through which the light passes as illustrated in figure 2.4.

2.1.3.2 Radiative and non-radiative decay processes

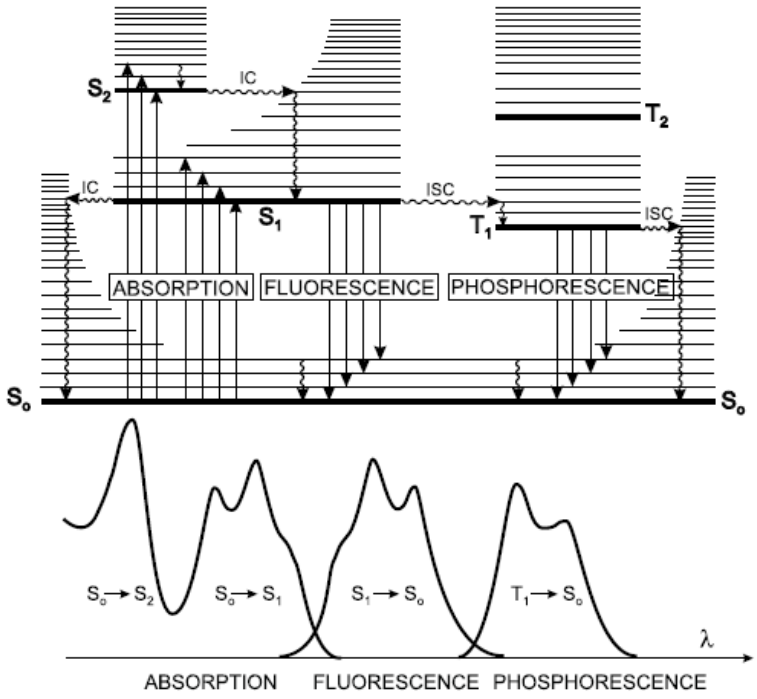

Figure 2.5: Jablonski diagram with transitions and corresponding schematic spectra. Reproduced from [21, p. 35] with permission.

The Jablonski diagram shown in figure 2.5 illustrates the possible processes after photon absorption. Singlet states are denoted with S_0, S_1, and S_2, triplets with T_1 and T_2 and for each electronic level the corresponding vibrational levels are shown. After absorption, which usually occurs from the lowest vibrational level of S_0, the following processes are possible:

Internal conversion Internal conversion (IC) occurs between two states of the same spin multiplicity. It is non-radiative and often followed by vibrational relaxation to the ground state. Internal conversion from S_1 to S_0 is less efficient than from S_2 to S_1 as the energy gap is much larger in the former case. Fluorescence and intersystem crossing are competing processes.

Fluorescence Fluorescence is the relaxation from S_1 to S_0 accompanied by the emission of a photon. The transition between the lowest vibronic levels is the same for absorption and emission, however, the fluorescence spectrum is usually red-shifted compared to the absorption spectrum. This is due to the vibrational relaxation being faster than the emission (see table 2.1) and therefore the transitions are usually from the lowest vibronic level of S_1 into higher vibronic levels of S_0. The gap between the maximum of absorption and fluorescence spectrum is called *Stokes shift*. As the difference of the vibronic levels is similar in the ground and the excited state for rigid molecules, the absorption and the fluorescence spectra display mirror symmetry in these cases. This is usually the case in conjugated polymers.

Intersystem Crossing A transition between two electronic states of different multiplicities is called intersystem crossing (ISC). This is a non-radiative transition and it usually takes place between two isoenergetic vibrational levels. In principle this transition is forbidden, but spin-orbit coupling can make it possible, this is especially efficient for heavy atoms.

Relaxation from the triplet state Relaxation from T_1 can occur radiatively or non-radiatively through intersystem crossing back to a high vibrational level of S_0. The radiative pathway is called phosphorescence. As these relaxations

are in principle spin-forbidden processes, they occur very slowly and therefore the triplet decay rate is much slower than that of singlet excitons. Compared to fluorescence, phosphorescence is red-shifted as the lowest vibrational level of T_1 is lower in energy than S_1.

If the concentration of triplets is very high, triplet-triplet annihilation can occur, which forms a ground state singlet S_0 and either an excited state singlet S_1 or triplet T_1. If an excited state singlet is formed, delayed fluorescence is possible.

Table 2.1 summarizes the processes and their corresponding timescales described in this section.

absorption	$10^{-15}s$	
vibrational relaxation	$10^{-12} - 10^{-10}s$	
lifetime of the excited state S_1	$10^{-10} - 10^{-7}s$	$\rightarrow$ fluorescence
intersystem crossing	$10^{-10} - 10^{-8}s$	
internal conversion	$10^{-11} - 10^{-9}s$	
lifetime of the excited state T_1	$10^{-6} - 1s$	$\rightarrow$ phosphorescence

Table 2.1: Characteristic timescales of absorption and subsequent processes.[21]

2.1.4 Energy transfer processes

Besides the various relaxation processes described above, excited molecules can also return to their ground state by transfering the energy onto a second molecule. This energy transfer between an energy donor (D) and an energy acceptor (A) is described by: $D^\star + A \rightarrow D + A^\star$.

Two different energy transfer mechanisms can be distinguished, leading to two different excited states. In terms of quantum mechanics the inital state of two specific electrons 1 and 2 is described by the wavefunction $\Psi_i = \Phi_{D^\star}(1) \cdot \Phi_A(2)$.

The **Förster mechanism** (also called Coulomb mechanism or Förster resonance energy transfer (FRET)) leads to the final state $\Psi_{fc} = \Phi_D(1) \cdot \Phi_{A^\star}(2)$.

The **Dexter mechanism** (also called exchange mechanism) on the other hand leads to the final state $\Psi_{fe} = \Phi_D(2) \cdot \Phi_{A^\star}(1)$.

To put that into words, in case of the Förster mechanism, electrons 1 and 2 stay on their original molecules while they are exchanged in case of the Dexter mechanism.

Both energy transfer mechanisms have several properties in common:

- The energy transfer between D and A occurs over a short distance, typically less than 10 nm, with Dexter being even shorter range than Förster.
- Spectral overlap between the fluorescence emission band of D and the absorption band of A is necessary.
- The energy transfer is radiationless, it does **not** occur through emission and re-absorption of light.
- Energy transfer opens an additional deactivation channel for the excited donor molecule decreasing the lifetime of the excited state strongly.

However, as the energy transfer mechanism is different, this has implications for the rate constants and the allowed transitions:

The Förster mechanism [22] is based on the interaction of the dipoles of the molecules occuring via electromagnetic fields through space. The radiation field of the dipole transition of the donor molecule induces a dipole transition in the acceptor molecule, therefore a spatial overlap between the wavefunctions is not required. The rate constant decreases to the sixth power of the distance between the molecules (R). An approximation for the Förster rate is given by:

$$k_{D^\star \to A} = \frac{1}{\tau_D} \left(\frac{R_0}{R} \right)^6 \tag{2.4}$$

Here τ_D is the lifetime of D in the absence of A and R_0 is called the Förster radius at which the rate constant $k_{D^\star \to A}$ is equal to the sum of the rate constants of all other relaxation channels. This value is typically between 4 and 10 nm for dye molecules in solution. It can be determined from spectroscopic data and is given by:

$${R_0}^6 = \frac{C \kappa^2 \Phi_D}{n^4} \int I_D(\lambda)\, \epsilon_A(\lambda)\, \lambda^4 d\lambda \tag{2.5}$$

where C is a constant factor containing basic quantities, κ is the orientational factor, Φ_D is the fluorescence quantum yield of D in absence of A, n is the refractive index, I_D is the fluorescence spectrum of D and ϵ_A is the molar absorption coefficient of A.

The Dexter mechanism [23] is based on quantum mechanical exchange interaction and can only occur if D and A exhibit strong spatial overlap. The distance over which the energy transfer can happen is therefore much shorter, typically 0.5-1 nm. The rate constant $k_{D^\star \to A}$ shows an exponential dependence on the distance R between D and A:

$$k_{D^\star \to A} \propto exp\left(-2\frac{R}{L}\right) \int f'_D\left(\tilde{\nu}\right) \epsilon'_A\left(\tilde{\nu}\right) d\tilde{\nu} \tag{2.6}$$

where f'_D is the emission of D, ϵ'_A is the absorption of A, and L is the van-der-Waals distance. In contrast to the Förster mechanism, Dexter transfer also enables energy transfer of triplet and polaron states.

2.1.5 Stark effect

The optical properties of an atom or molecule are influenced by external electric fields as first described by Johannes Stark in 1913.[24]

For a transition involving two electronic states, the field $\vec{F}$ perturbs the absorber's transition dipole $\vec{m}$ (proportional to its oscillator strength and absorption cross-section) and peak position $\bar{\nu}_{max}$. This is termed classical Stark effect as opposed to the non-classical Stark effect where the reaction dynamics of a process and thus the line shape of the absorption is affected by an electric field.[25] The changes in both $\vec{m}$ and $\bar{\nu}_{max}$ can be expressed by a second order Taylor expansion. The change in transition dipole is given by:

$$\vec{m}\left(\vec{F}\right) - \vec{m} = \underline{A} \cdot \vec{F} + \vec{F} \cdot \underline{B} \cdot \vec{F} \tag{2.7}$$

where $\underline{A}$ is the transition polarizability and $\underline{B}$ is the transition hyperpolarizability. The change in transition frequency $\Delta\nu$ is given by:

$$\bar{\nu}_{max}\left(\vec{F}\right) - \bar{\nu}_{max} = -\Delta\vec{\mu} \cdot \vec{F} - \frac{1}{2}\vec{F} \cdot \underline{\Delta\alpha} \cdot \vec{F} \tag{2.8}$$

where $\Delta\vec{\mu}$ is the change in dipole moment and $\Delta\alpha$ is the change in polarizability between ground and excited state.

In this thesis the Stark effect of a photoinduced field created by charges is investigated. Chapter 6.7 deals with the effect of the field on the electronic transitions in a conjugated donor-acceptor polymer. It is found that $\Delta\vec{\mu}$ is often the dominant contribution to the Stark effect.[25] Conjugated polymers, especially donor-acceptor polymers, exhibit a big dipole moment and also structural change in the excited state, leading to a substantial change in dipole moment from ground to excited state. Therefore, in our analysis we assume as a first approximation that the change in dipole moment is the predominating factor and the change in transition dipole $\Delta\vec{m}$ and the change in polarizability $\Delta\alpha$ can be neglected. We will demonstrate in chapter 6.7 that this approximation works well to fit the data. In the following we will therefore focus on the linear Stark effect on the peak position, i.e. the term $\Delta\nu = -\Delta\vec{\mu}\cdot\vec{F}$ which is linear in the electric field. Here, three distinct cases of alignment of change in dipole moment $\Delta\vec{\mu}$ and field $\vec{F}$ can be distinguished: preferential alignment in parallel (see figure 2.6(a)), anti-parallel (see figure 2.6(b)), and an isotropic distribution of $\Delta\vec{\mu}$ with respect to the field.

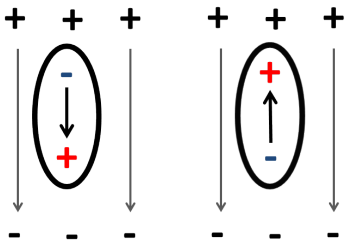

(a) (b)

Figure 2.6: Orientation of a change in dipole moment $\Delta\vec{\mu}$ (a) in parallel with the electric field and (b) anti-parallel with the electric field.

Figure 2.7 shows the corresponding linear Stark effect on the absorption spectra. If the change in dipole moment $\Delta\vec{\mu}$ of a molecule is oriented in parallel to the

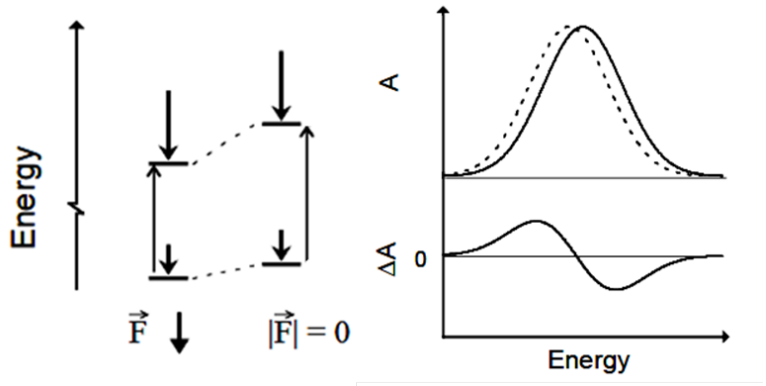

(a)

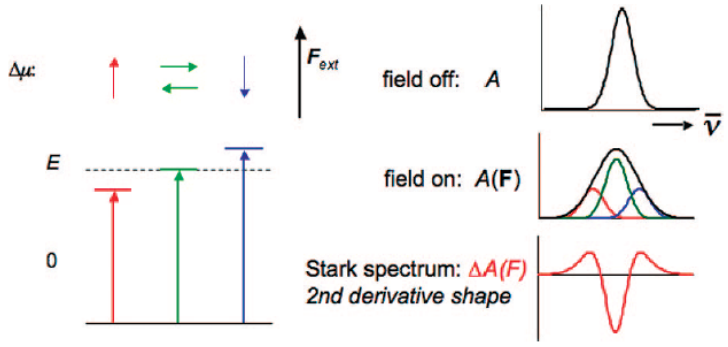

(b)

Figure 2.7: Linear Stark effect of an applied field on the absorption spectrum. Panel (a) shows the interaction of an electric field with the change in dipole moment aligned with the field. The corresponding shifted absorption spectrum is shown on the right with dotted lines, the spectrum without field is represented by a solid line. This results in the difference of the absorption ΔA having a first derivative lineshape. Panel adapted from [26] with permission. Panel (b) shows the case for an isotropic sample where the changes in dipole moment are oriented randomly with respect to the field. Both red- and blue-shift of the absorption spectrum is observed, resulting in ΔA having a second derivative lineshape. Panel reproduced from [25] with permission.

electric field (figure 2.6(a)), the energy levels are shifted to more negative energies as the states become more energetically favorable (shown in figure 2.7(a)). This results in the absorption being red-shifted and the difference in transmission $\frac{\Delta T}{T}$ being proportional to the positive first derivative of the absorption with respect to wavelength. On the other hand, when $\Delta\vec{\mu}$ and field are aligned anti-parallel (figure 2.6(b)), the absorption is blue shifted, the transition becomes energetically less favorable and $\frac{\Delta T}{T}$ is proportional to the negative first derivative of the absorption with respect to wavelength. In the case of $\Delta\vec{\mu}$ and the field being oriented randomly, blue-shift, red-shift and no shift at all are observed (depicted in figure 2.7(b)). This leads to broadening of the absorption and $\frac{\Delta T}{T}$ being proportional to the negative second derivative of the absorption.

Taking these absorption shifts into account we can analyze spectra in terms of the orientation of dipoles with respect to the field and compare the extent and the direction of the dipole orientation in different samples.

2.2 Photophysical processes in organic solar cells

The basic principle of a solar cell is the conversion of solar into electrical power. The steps involved in that process in an organic solar cell are schematically illustrated in figure 2.8 and will be discussed in this section. First, the generation of charges at an interface of a donor and an acceptor material will be discussed (section 2.2.1), then their transport to the electrodes (section 2.2.2) and finally we will take a closer look at recombination mechanisms which limit solar cell performance (section 2.2.3). Comprehensive reviews are found in [27–30].

2.2.1 Charge generation

2.2.1.1 Exciton diffusion and quenching by charge transfer

The photoactive layer of a bulk heterojunction organic solar cell consists of two materials with different electron affinities and ionization potentials. Light is absorbed in one of the materials and an exciton is generated (see section 2.1.2). It is separated into charges at the interface with the other material. A common

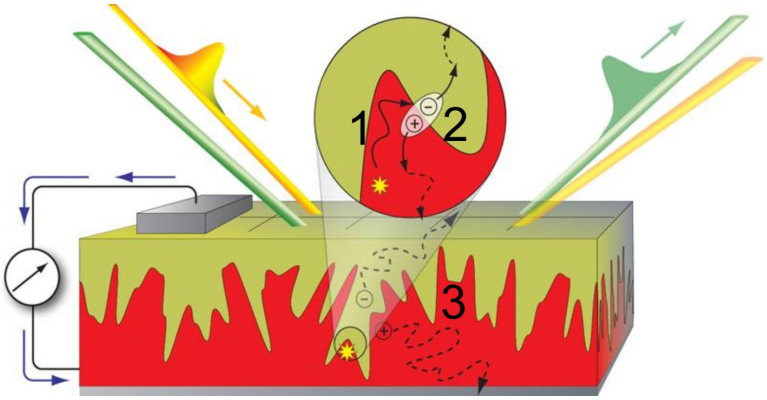

Figure 2.8: Charge generation process in an organic solar cell: (1) Upon absorption of light an exciton is created that diffuses to the donor-acceptor interface and forms a charge-transfer exciton (2) which is then split up and the charges are transported to the electrodes (3). The optical pump beam (shown in green) and probe beam (shown in yellow) illustrate the transient absorption experiment that will be introduced in section 2.3. Figure reproduced from [31].

material combination consists of an electron-donating polymer and the electron-accepting fullerene PCBM (phenyl-C61-butyric acid methyl ester). The absorption of PCBM is negligible in the visible wavelength range, which means that light is absorbed mainly in the polymer. Therefore, the more electropositive material is usually called 'donor', the electronegative material 'acceptor'. However, other electron acceptor materials, such as $PC_{71}BM$, perylenediimides (PDI) or polymeric acceptors, also absorb light and therefore act as a hole donor; we will see that this is the case in chapter 6.

As the exciton diffusion length is usually on the order of 10-20 nm [32] in semiconducting polymers, the donor and the acceptor material are blended to form an interpenetrating network. For efficient exciton dissociation the phase separation should in principle be as small as possible, otherwise excitons decay before reaching the interface. However, for the subsequent steps, such as electron-hole separation and transport to the electrodes, a coarse phase separation is needed. An optimum trade-off between these oppositional requirements has to be found for each material combination individually. The percentage of excitons that

are quenched at the interface can be estimated with photoluminescence quenching experiments where the steady-state PL of the blend compared to the pristine material is measured.[33, 34]

The charge-transfer reactions at the interface of donor and acceptor are illustrated in figure 2.9. After light absorption in the donor material, an electron is transferred to the acceptor material (see figure 2.9(a)). If light is absorbed in the acceptor material, a hole is transferred to the donor material (see figure 2.9(b)). Another possible pathway after light absorption in the acceptor material is Förster energy transfer of the exciton to the donor material (see section 2.1.4), subsequently the exciton can be quenched by electron transfer onto the acceptor material (see figure 2.9(c)). Energy transfer from donor to acceptor and subsequent hole transfer is also possible.

Exciton quenching and charge generation is often found to take place on the timescale of 100 fs.[35–38] As this is much faster than the time it takes an exciton to diffuse to the interface, Banerji and coworkers suggested that the exciton is initially delocalized, this would also reduce its binding energy and thus assist charge separation.[29, 30, 39] A different explanation was put forward by Durrant and coworkers: They suggested that charge generation takes place in domains where donor and acceptor are mixed very intimately making diffusion unnecessary; for subsequent charge separation also crystalline domains are necessary.[40]

2.2.1.2 Charge-transfer states

Charge transfer at the interface can result in either spatially separated free charges or in charge-transfer (CT) states. In a charge-transfer state, the electron and hole are still coulombically bound, this attraction has to be overcome to form free charges. Experimentally, the energy level of the charge-transfer state is usually determined with electroluminescence (EL), where charge carriers are injected to form a CT state which decays radiatively.[41, 42] Also, PL or absorption measurements of a donor-acceptor blend might show additional features compared to the individual components, indicating the presence of a charge-transfer state.[43]

The energetics of the intermediate charge-transfer state which is formed at the interface after exciton quenching and its role in free charge generation has

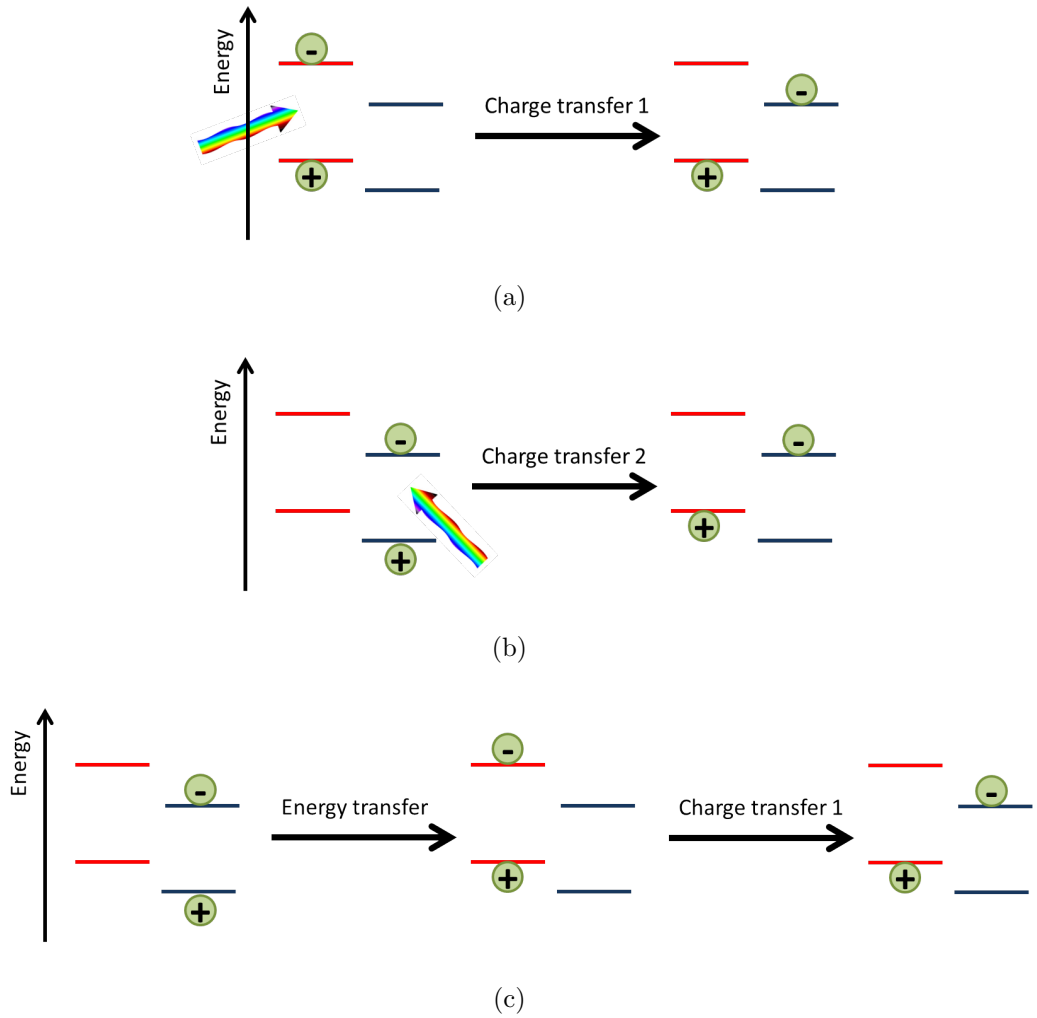

Figure 2.9: Typical charge transfer reactions after an exciton has reached the donor-acceptor interface. The donor material is shown with red energy levels, the acceptor material with blue energy levels. Panel (a) depicts light absorption in the donor material and electron transfer onto the electron acceptor. Panel (b) depicts light absorption in the acceptor material and hole transfer onto the donor material. Panel (c) illustrates Förster energy transfer to the donor material after light absorption in the acceptor material and subsequent electron transfer onto the acceptor.

been the subject of recent debate. Howard and coworkers found that after 100 fs two populations are present in P3HT:PCBM blends: bound charges and free charges. The bound charges recombine within 2 ns while the free charges can be extracted into an external circuit. Recent experiments by Bakulin and coworkers have shown that free charge generation occurs via a delocalized CT state; relaxed CT states thus represent a loss channel as they cannot overcome their coulombic binding energy.[44] This was shown with a pump-push-probe experiment, where an infrared push pulse was used to excite relaxed CT_0 states into higher-lying (by 0.3-1 eV) delocalized CT_n states (see figure 2.10). An increase in photocurrent due to free charge carrier generation was measured. Similar results concerning the role of the CT state were found by Grancini and coworkers using transient absorption spectroscopy on PCPDTBT:PCBM blends.[45] They found that both interfacial CT states and free charges were generated in the first tens of femtoseconds. The higher-lying, more delocalized CT states were more likely to be separated into free charges, while the relaxed CT state constituted a loss channel.

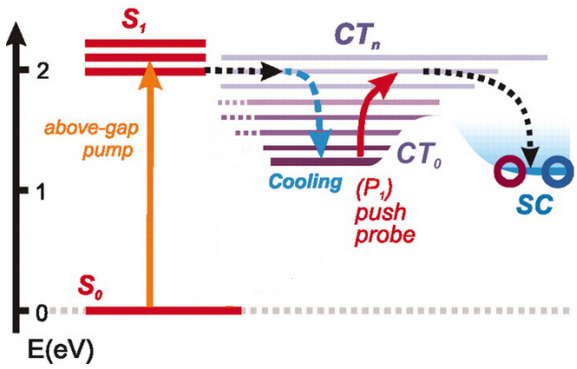

Figure 2.10: Energy diagram of free charge carrier generation in a typical donor-acceptor system in an organic solar cell. With an optical pump pulse localized CT_0 states are pushed into higher lying energy levels (CT_n) and can be separated into free charges (SC) from there. Figure adapted from [44] with permission.

In polymer:polymer blends, a very high density of charge-transfer states was observed by Howard and coworkers.[31] Here, the charge-transfer states were long-lived and decayed on a timescale of 100 ns.

2.2.1.3 The role of morphology and field

Morphology plays a huge role in the charge generation process. As discussed above, the mesoscale morphology, i.e. the lengthscale of phase separation between donor and acceptor component, determines efficient exciton quenching and charge transport. Optimizing the mesoscale morphology of two given materials is usually done by the choice of solvent(s) and annealing conditions. A well-known example is the PTB7:$PC_{71}BM$ system, where the phase separation is significantly decreased by using 1,8-diiodoctane (DIO) as a co-solvent, the power conversion efficiency is thus increased from 3.9% to 7.4%.[46] Morphology on an even smaller lengthscale plays an important role as well: Besides the domain size, the domain purity [47–50], the cristallinity of the components [51, 52], and the orientation of the molecules at the interface [43, 50, 53, 54] are important factors influencing free charge generation.

In an organic solar cell, the field dependence of the photocurrent has a critical influence on device performance as it affects the fill factor. Two different processes can be responsible for the bias dependence, the field-activated charge-transfer state splitting and the competition between extraction and non-geminate recombination.[55] Kniepert and coworkers adopted a method to probe the field dependence of charge generation.[56] In this time-delayed collection field (TDCF) experiment free charges are generated by a short laser pulse and extracted by a rectangular voltage pulse. By applying a variable DC voltage during charge generation, the field dependence of generation is directly probed by the change in the total amount of extracted charges. They found different results depending on the photoactive material: While charge carrier generation in P3HT:PCBM blends is not field-dependent,[56] the low-bandgap polymer PCPDTBT blended with $PC_{71}BM$ exhibits a strong field dependence of free charge carrier generation.[57] The reason for the field dependence of the photocurrent in P3HT:PCBM devices was shown with time-delayed double pump experiments by Mauer and coworkers.[55] Here, the current-voltage characteristics of a solar cell during illumination with two laser pulses are measured and by changing the time delay between the pulses the charge carrier dwell time can be calculated. They find that

the field dependence of the photocurrent is determined by the competition between carrier extraction and non-geminate recombination: at higher fields, charge carriers are swept out faster, therefore less charge carriers recombine.

2.2.2 Charge transport

Once free charge carriers are created in the photoactive layer of the organic solar cell their transport to the electrodes must be accomplished, while recombination processes are competing loss channels (see section 2.2.3). Different models describing the charge transport and its dependence on field and temperature exist, such as hopping, polaron transport and trapping/detrapping models.[58] In the following, the Gaussian Disorder Model will be discussed in more detail, as it is able to explain experimental properties to a large extent.

Hopping in a Gaussian Disorder Model. The distribution of conjugation lengths in organic semiconductors discussed in section 2.1.1 leads to an energy level distribution. This is described by a density of states (DOS) that is mathematically expressed by a normal distribution as suggested by Bässler:[59]

$$\rho\left(E\right) = \frac{1}{\sqrt{2\pi\sigma^2}} \cdot exp\left(-\frac{E^2}{2\sigma^2}\right) \tag{2.9}$$

where $\sigma\left(E\right)$ is the standard deviation of the Gauss distribution. It is also called *disorder parameter* and is roughly between 50 and 100 meV for most organic semiconductors.[60] The transport of charge carriers involves hopping among localized states in the DOS, which is a phonon-assisted tunneling process. The hopping rate ν_{ij} between two sites i and j can be calculated with the Miller-Abrahams equation:[61]

$$\nu_{ij} = \nu_0 \cdot \exp(-2\alpha R_{ij}) \cdot \begin{cases} \exp\left(-\frac{E_j - E_i}{kT}\right), & E_j > E_i \\ 1, & E_j < E_i \end{cases} \tag{2.10}$$

where ν_0 is the phonon vibration frequency, α the inverse localization length (roughly equal to the π-electron delocalization length) and R_{ij} the electronic wave function overlap. For jumps upwards in energy ($E_j > E_i$) a Boltzmann factor is included. We can immediately see that for T$\rightarrow$0 K the hopping rate becomes

negligible, thus freezing charge transport. As the first exponential depends on the distance between the sites, it is clear that adjacent sites are favored compared to distant sites. For states with the same energy, the same transition rate applies to a jump to and from the site. As this is not the case for states with an energetic offset, sites that are very low in energy can act as charge carrier traps.

With regard to macroscopic charge transport it has to be taken into account that a charge carrier visits a large number of sites with different energetic states (lying in the DOS) and spatial distances. Assuming Gaussian distributions for the site energies and the jump distances (with the width Σ), the macroscopic measurable mobility can be described depending on field and temperature:

$$\mu(T,F) = \mu_0 \cdot \exp\left[-\left(\frac{2\sigma}{3kT}\right)^2\right] \cdot \exp\left[\left(C\left(\frac{\sigma}{kT}\right)^2 - \Sigma^2\right)\sqrt{F}\right] \tag{2.11}$$

where C is an empirically determined constant and μ_0 is the mobility at zero field and infinite temperature. However, the dependence of charge carrier mobility on charge carrier density is not taken into account with equation 2.11.[62] Also, equation 2.11 is only valid at temperatures between the glass transition temperature T_g and a critical temperature T_c ($T_g > T_c$) , which is dependent on the energetic disorder σ and the length of the charge transport distance L_0 (i.e. the film thickness):

$$\left(\frac{\sigma}{kT_c}\right)^2 = 44.8 + 6.7 \cdot log\left(L_0\right) \tag{2.12}$$

Below T_c charges will not reach a dynamic equilibrium as their transit time through the sample is faster than the equilibration process and the mobility would then depend on the sample thickness.

Charge carrier mobilities. The experimentally determined charge carrier mobility μ is the most widely used parameter to compare charge transport properties of different materials. Several methods exist to determine it, and its value depends strongly on the type of measurement. Therefore care has to be taken when comparing mobilities or choosing a method for determining the mobility for a specific problem as each method has its advantages and limitations. Some of the most widely used methods include:

- Time of flight
- Field effect transistors
- Space charge limited current
- Photogenerated charge extraction by linearly increasing voltage
- Pulsed-radiolysis time-resolved microwave conductivity

2.2.3 Charge recombination

In the previous sections the processes contributing to the photocurrent, i.e. charge generation and charge transport, were discussed. However, at all stages of the charge carrier generation and extraction process, competing charge recombination processes limit the efficiency. Figure 2.11 gives an overview of the loss processes:

- Exciton decay: internal conversion or radiative decay before the exciton has found an interface (see section 2.1.3.2)
- Geminate recombination of bound charge pairs
- Non-geminate recombination of free charges
- Trap-assisted recombination of free and trapped charges

Experimentally, geminate and non-geminate recombination processes can be distinguished by their intensity dependence (see also section 2.3.4). As the charges undergoing geminate recombination come from the same tightly-bound state, it is a monomolecular and concentration-independent process, i.e. its rate is proportional to the number of bound charge pairs present: $\frac{dn}{dt} = kn$. On the other hand, charges undergoing non-geminate recombination are free and therefore it is a charge carrier concentration dependent process: $\frac{dn}{dt} = \mu n^{2+x}$.

Non-geminate recombination as a random process of opposite charge carriers meeting can be described by Langevin's equation, which was originally developed for the recombination of ions in gases.[63] Here, the Langevin recombination rate R is proportional to the product of electron (n) and hole (p) density which must be equal for photogenerated charges ($n = p$):

$$R = \gamma_l \cdot n \cdot p = \gamma_l \cdot n^2 \tag{2.13}$$

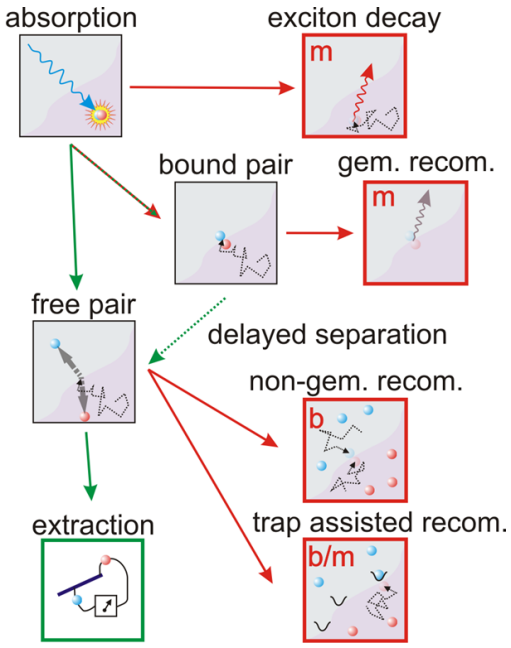

Figure 2.11: Overview of the charge generation and loss processes in an organic solar cell. Loss processes are depicted with red arrows, desired processes with green arrows. The order of the recombination process is indicated with m=monomolecular and b=bimolecular. Figure reproduced from [12] with permission.

The bimolecular rate constant γ_l depends on the sum of hole (μ_h) and electron (μ_e) mobility :

$$\gamma_l = \frac{e\,(\mu_e + \mu_h)}{\epsilon\epsilon_0} \tag{2.14}$$

However, organic semiconductors do not strictly behave like ions in gases as they are not three dimensionally isotropic and completely homogeneous. For instance, in blends of donor and acceptor, the hole and electron are confined to their respective phase which limits the recombination to the interface of both materials. This leads to a reduction in the rate of recombination which can be characterized by a prefactor ξ. ξ is usually on the order of $10^{-1} - 10^{-3}$.[64, 65] In many cases for organic heterojunctions the recombination rate has an order greater than 2.[36, 66, 67] The reasons are still discussed, possible explanations include a charge density dependence of the mobility,[68] morphology-restricted

charge carrier diffusion [69] or a distribution of traps.[70] The modified Langevin recombination rate taking into account these corrections is:

$$R = \xi \frac{e\left(\mu_e + \mu_h\right)}{\epsilon\epsilon_0} n^{\lambda+1} = \psi_m n^{\lambda+1} \tag{2.15}$$

Trap-assisted recombination is monomolecular if the trapped charge density is constant, but can also follow more complex behaviours if this is not the case.[12]

2.3 Ultrafast spectroscopy

To investigate photophysical processes like charge carrier generation and recombination as discussed in the previous section, ultrafast spectroscopy is an invaluable tool. The term *ultrafast* refers to processes happening in the picosecond and femtosecond time range and in this section the techniques enabling the access to this time range will be introduced. In order to track excited states with transient absorption spectroscopy (see section 2.3.4), an ultrashort pulse of variable wavelength is needed to excite the sample (see section 2.3.3) and an ultrashort broad white light pulse is needed to probe the sample after excitation (see section 2.3.2).

2.3.1 Ultrafast pulse generation and amplification

In order to time-resolve ultrafast events, ultrafast laser pulses are necessary. The technique used for creating ultrashort pulses from lasers is called mode locking, where laser beams with different frequencies are superimposed with a fixed phase relation φ_m as shown in figure 2.12.

This is done in the resonant cavity of the laser as shown in figure 2.13(a). The length of the laser cavity L determines the cavity round-trip time $T_R = \frac{2L}{c_g}$ where c_g is the group velocity, i.e. the propagation velocity of the peak of the pulse intensity. The inverse of the cavity round-trip time is the pulse repetition rate ν_R. In figure 2.13(b) the corresponding pulse train is schematically depicted. In order to achieve short pulses the spectral bandwidth $\Delta\omega$ has to be large as, due to the uncertainty principle, $\Delta t \propto \frac{1}{\Delta\omega}$. The bandwidth is widened when the number of locked modes is increased.

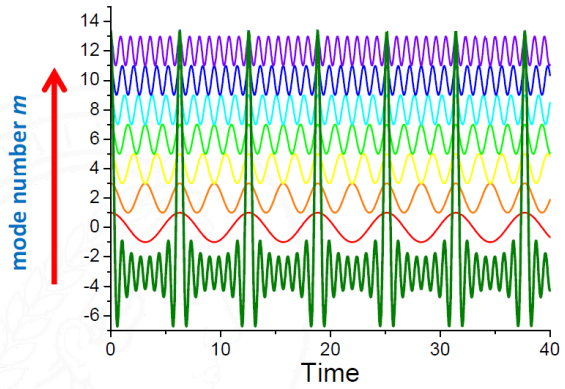

Figure 2.12: Mode locking of laser beams with different frequencies, but a fixed phase relation φ_m leads to short laser pulses. Figure adapted from [71].

In a laser system mode locking can be realized actively or passively, however, much shorter pulses are obtained with passive mode locking, where the light in the cavity is used to cause a change in an intracavity element which in turn modulates the intracavity light. The most common technique is Kerr lens mode locking which allows mode locking of a very large bandwidth and thus pulses down to the sub-5fs regime.[72] Its principle is based on a medium with a nonlinear refractive index, i.e. a material in which the refractive index changes with light intensity (optical Kerr effect). In such a material, light with high intensity is focused differently from low-intensity light and thus can be separated geometrically. The material of choice for ultrafast pulse creation is titanium sapphire as it exhibits both strong self-focusing and good gain properties; its center wavelength is at 800 nm.

The laser pulses can be further modified, if higher energy or shorter pulse length is necessary. Pulses exhibit a prolongation due to chirp which is caused by the frequency dependence of the Kerr effect and chromatic dispersion. Compression can be done with dielectric mirrors. The pulses can also be further amplified. This can be done by first stretching the pulse to prevent damage in the optics from high energies, then amplifying it in a gain medium and then compressing it again to its original femtosecond pulse shape. The stretching and compression are usually done with grating setups and the amplification is done by seeding

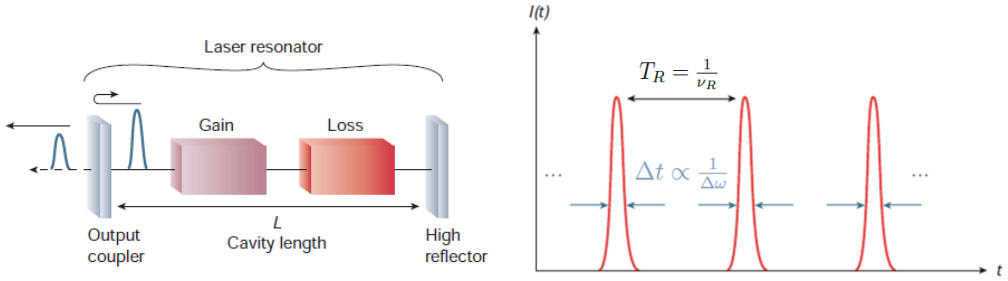

(a) (b)

Figure 2.13: Figure (a) depicts a typical laser cavity used for mode locking. The resulting pulse train is shown in figure (b). Panel reproduced from [72] with permission.

a second Ti-sapphire cavity with the ultrafast pulse train. The injection and extraction in the amplifier cavity are controlled by Pockels cells.

2.3.2 Supercontinuum white light generation

Coherent supercontinuous white light can be generated by focusing a strong ultrashort laser pulse into an optically highly non-linear medium, such as sapphire (α-Al_2O_3), yttrium aluminum garnet (YAG, $Y_3Al_5O_{12}$) or yttrium vanadate (YVO_4).[73] Figure 2.14 shows a typical experimental setup. Depending on the non-linear medium used and the wavelength of the seed pulse, white light ranging from 400 nm to >1800 nm can be created. The duration of the white light pulse is not longer than the excitation pulse.

2.3.3 Optical parametric amplification

For ultrafast spectroscopical experiments it is very useful to be able to generate short laser pulses at various wavelengths and not only at 800 nm which is the fundamental output of the Ti:sapphire laser. This can be achieved in an optical parametric amplifier (OPA), as schematically depicted in figure 2.15. Here, a signal and a strong pump (e.g. the 800 nm output from the Ti:sapphire laser) are overlapped under phase-matching conditions in a non-linear optical medium

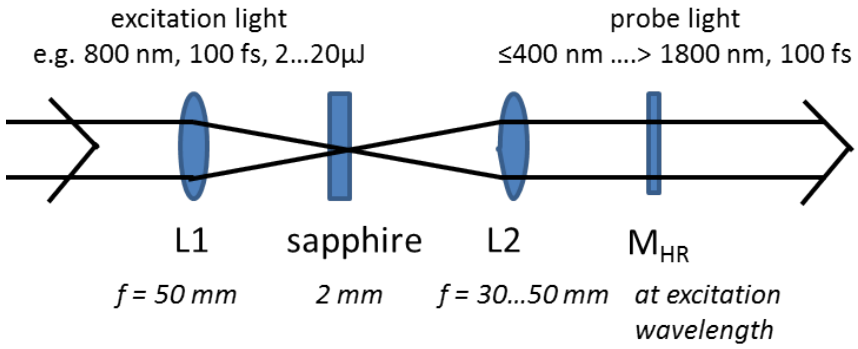

Figure 2.14: Experimental setup for generation of white light with fs duration. The seed pulse, e.g. from a Ti:sapphire laser, is focused with L1 into the sapphire. The white light is generated within the sapphire due to non-linear effects and is then collimated with L2. M_{HR} filters out the residual excitation pulse.[74, p. 590]

(e.g. β-BaB_2O_4). The signal is amplified at the expense of the pump and additionally an idler beam is created whose frequency equals the difference between the frequencies of pump and signal.

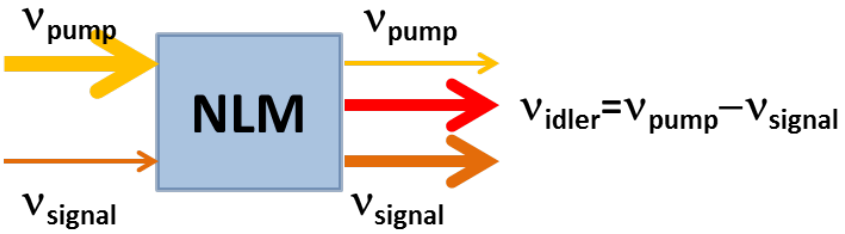

Figure 2.15: Schematic illustration of an optical parametric amplifier. The signal is amplified by overlapping it with a strong pump in a non-linear medium (NLM). An additional idler beam is created due to the principle of energy conservation.[74, p. 194]

In order to access a wide range of amplified wavelengths, a supercontinuum white light seed can be used and by adjusting both phase matching and delay between white light and pump, the wavelength to be amplified can be chosen.

Moreover, sum frequency mixing and second harmonic generation is possible and thus a wavelength range of ultrashort laser pulses from UV to IR can be accessed with optical parametric amplification.

2.3.4 Signals in transient absorption spectroscopy

Transient absorption spectroscopy is a powerful technique to track excited state dynamics. The transmission of a sample after excitation with an ultrashort pump pulse T_{exc} is measured with a white light pulse and compared to the transmission without previous excitation T_{GS} (ground state transmission). By introducing a variable time delay between pump and probe pulse, the temporal evolution of the excited states can be tracked. For a transient absorption spectrum, $\Delta T/T$ is calculated with the following equation:

$$\Delta T/T\,(\lambda, t) = \frac{T_{exc}\,(\lambda, t) - T_{GS}\,(\lambda)}{T_{GS}\,(\lambda)} \tag{2.16}$$

Three different mechanisms are responsible for the excited-state spectrum: ground state bleach (GSB), stimulated emission (SE) and photoinduced absorption (PIA). Their origin in terms of transition between states is illustrated in figure 2.16(a), their spectral position is schematically depicted in figure 2.16(b).

When excited states are populated due to the pump pulse, the ground state S_0 is depleted. Therefore the transmission in the region where previously the ground state was absorbing is increased, $\Delta T/T$ is positive, we find a **ground state bleach**. In this region the dynamics of the sum of all excited states can be tracked as they all bleach the ground state.

If the pump pulse populates fluorescent excited states, their radiative decay into the ground state can be stimulated by the probe pulse. This additional **stimulated emission** in the region of the sample's fluorescence causes a positive $\Delta T/T$ signal and can be used to monitor emissive excited-state populations.

When higher lying states such as S_1 are populated, they in turn can be excited to even higher lying states. This **photoinduced absorption** decreases the transmission in the wavelength region corresponding to that transition, we therefore find a negative $\Delta T/T$ signal. Not only primary excited states, but also

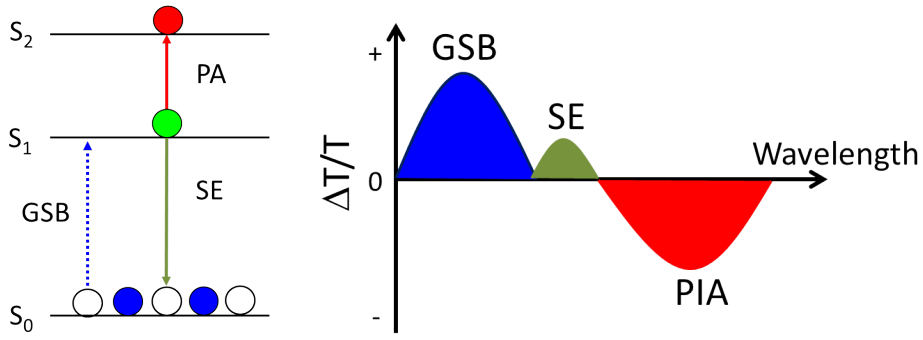

(a) (b)

Figure 2.16: Typical signals found in transient absorption measurements: GSB: ground state bleach, SE: stimulated emission, PIA: photoinduced absorption. Figure (a) depicts the processes corresponding to the signals (dotted arrow means fewer transitions), figure (b) shows a schematic representation of the resulting spectrum.

charge-transfer states, free charges and triplets can be tracked by their PIA signal. As the spacing between electronic states tends to decrease, these PIA signals extend into the near infrared (NIR).

In the linear absorption regime, i.e. at low pump fluences where non-linear effects can be neglected, the signals are proportional to the number of absorbing species. ΔT/T for a transition between an initial state i and a final state f can then be expressed by the following equation:

$$\Delta \mathrm{T/T}\left(\lambda, t\right) = -\sum_{i,f} \sigma_{if}\left(\lambda\right) \Delta N_i\left(t\right) d \tag{2.17}$$

where σ_{if} is the cross section of the probed transition, ΔN_i is the population change of the initial state and d the film thickness.[75] In equation 2.17 the GSB would be described by a $0 \rightarrow f$ transition, SE by a $f \rightarrow 0$ transition and PIA by $i \rightarrow f$ where $i \neq 0$.

As the signal is directly proportional to the population of an excited species, the population of an excited state can be tracked directly if a wavelength region is found without overlapping signals from different species. However, as this is usually not the case, we need data analysis methods to approximate population

flows from the measured transient absorption surfaces. These are discussed in section 2.4.

Section 2.2.3 introduced the intensity dependence of decay processes of excited species, and by varying the pump intensity in a transient absorption experiment it is possible to distinguish between them. Figure 2.17 shows simulated data of normalized kinetics at different pump intensities at time delays starting from 500 ps. In case (a), the recombination dynamics are monomolecular, indicating recombination of bound charge pairs or trap-limited recombination. In (c) free charges recombine, leading to intensity dependent recombination dynamics. Figure 2.17(b) depicts kinetics of a signal which stems from both bound and free charge carriers (in a 50:50 ratio).

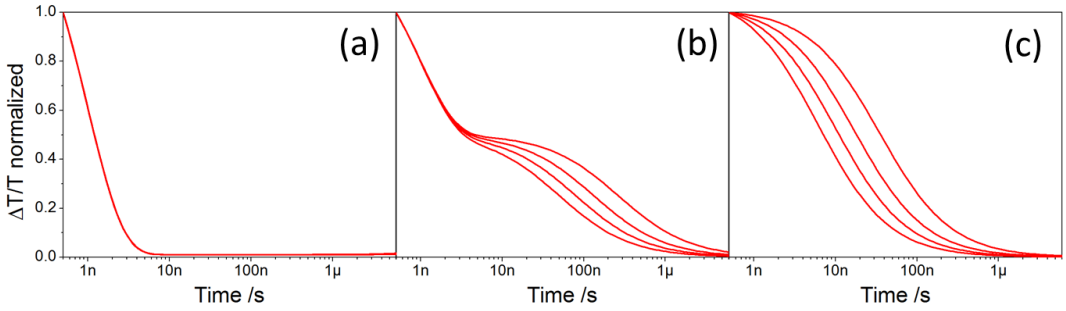

Figure 2.17: Simulated normalized kinetics of different recombination processes: (a) monomolecular recombination of bound charge pairs (c) bimolecular recombination of free charge carriers and (b) recombination of 50:50 bound and free charge carriers.

Experimental details of transient absorption spectroscopy can be found in section 3.4.1, we now take a deeper look at data analysis methods of more complex signals.

2.4 Transient absorption data analysis

The result of modern transient absorption experiments is a data matrix consisting of m rows each of which is the n long transient absorption spectrum (where n

corresponds to the number of illuminated pixels on the linear array detector behind the spectrograph) measured at the m^{th} time delay. The data matrix expresses ΔT/T as a function of wavelength and time, $\mathbf{D}(m,n) = \Delta\text{T/T}(t,\lambda)$, and is often plotted as a surface against these two variables. This is shown in the first panel of figure 2.18.

The goal of transient absorption data analysis is to determine the number of excited-state species, the evolution of the concentration of each excited-state species' population with time, and the ΔT/T spectrum of each excited-state species over the wavelength region measured. As long as the spectrum of each excited-state species does not change with time, analysis of the transient absorption data corresponds to finding a bilinear decomposition of the measured data matrix with a given number, p, of excited-state species: $\mathbf{D} = \mathbf{CS} + \mathbf{E}$, where $\mathbf{C}$ is an $(m \times p)$ matrix in which the i^{th} column corresponds to the population of the i^{th} species at each of the m measured timepoints, $\mathbf{S}$ is a $(p \times n)$ matrix in which the i^{th} row represents the transient absorption spectrum of the i^{th} species (at the n wavelengths of the measured data), and $\mathbf{E}$ is an $(m \times n)$ matrix that represents the difference between the measured data and its idealized description (given by $\mathbf{CS}$) due to experimental noise. This is graphically illustrated in the first panel of figure 2.18. It is important to note, that the number of excited-state species, p, that are required to describe the experimental data corresponds to the rank of the data matrix. The matrix multiplication $\mathbf{CS}$ can be written as the series from $i = 1 \ldots p$ of the outerproducts between the i^{th} column of $\mathbf{C}$ and the i^{th} row of $\mathbf{S}$, $\mathbf{CS} = \sum_1^p \text{c}(i) \otimes \text{s}(i)$, where c($i$) and s($i$) are the i^{th} column of the concentration matrix and the i^{th} row of the spectral matrix respectively. Physically speaking, this means that the total transient absorption surface can be thought of as a sum of rank 1 surfaces each given by the outer product of the concentration profile of an excited-state species with that species' transient absorption spectrum. This is again shown graphically in the last two panels of figure 2.18.

Following from the results of the last paragraph, the goal of transient absorption data analysis is to factor the observed data matrix into the product of two matrices, which to reiterate are $\mathbf{C}$ an $(m \times p)$ matrix in which the i^{th} column gives the population of the i^{th} excited-state species as a function of time, and $\mathbf{S}$ a $(p \times n)$ matrix in which the i^{th} row gives the spectrum of the i^{th} excited-state species as

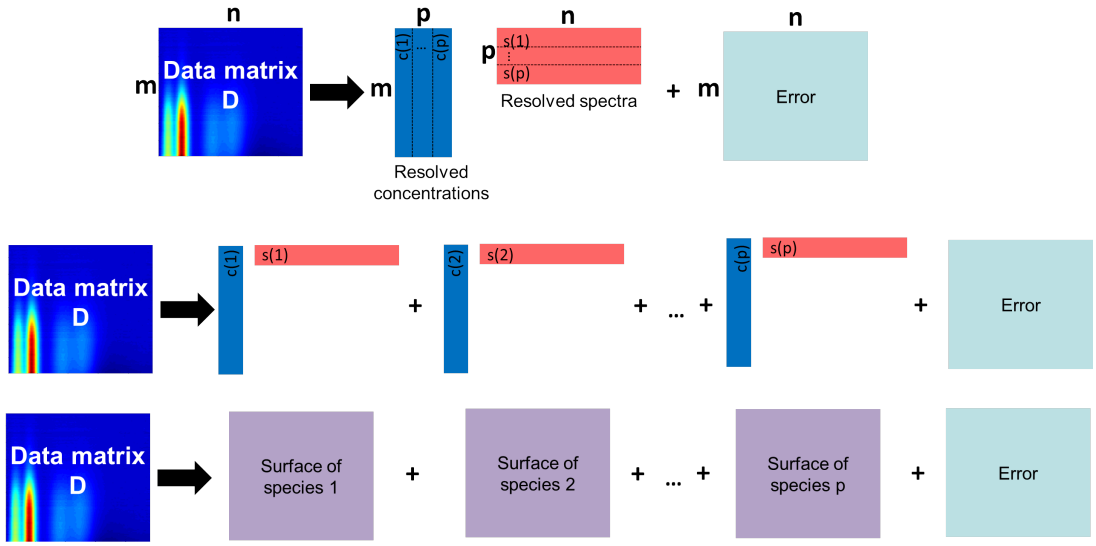

Figure 2.18: The upper panel shows a bilinear decomposition of a transient absorption data surface ($m \times n$) into resolved concentration ($m \times p$) and spectra ($p \times n$) profiles plus an error matrix ($m \times n$). This means that the data matrix can be represented by the summation of the outer products of the individual concentration and spectra profiles of the p components, shown schematically in the lower panels.

a function of wavelength. Finally, p is the number of excited-state species that contribute to the measured transient absorption surface. We will now for the moment assume that we can find (based on mathematical techniques) a decomposition **CS** that accurately describes the measured data, and consider whether or not this decomposition is unique. As it turns out, it is easy to show that the decomposition is not mathematically unique, which will mean that mathematical techniques alone are insufficient to determine the physically true **C** and **S** matrices that we will label with the subscript a (for actual) as $\mathbf{C_a}$ and $\mathbf{S_a}$. Equation 2.18 shows that any invertible matrix **T** and its inverse can be introduced between **C** and **S**.

$$\mathbf{D} = \mathbf{CS} = (\mathbf{CT})\left(\mathbf{T}^{-1}\mathbf{S}\right) = \mathbf{C}_{new}\mathbf{S}_{new} \tag{2.18}$$

As the product of **T** and its inverse is the identity matrix, their introduction does not change the result of the matrix multiplication at all. As matrix multiplication

is associative we can calculate the matrix product as $(\mathbf{CT})(\mathbf{T^{-1}S})$, as also shown in equation 2.18. The term in the first brackets $(\mathbf{CT})$ can be considered a new concentration matrix, $\mathbf{C_{new}}$, wherein each of the new columns (concentration profiles) is a mixture of the old columns (concentration profiles) determined by the elements of $\mathbf{T}$. Similarly, the second bracketed term, $(\mathbf{T^{-1}S})$, can be considered a new spectra matrix, $\mathbf{S_{new}}$, in which each of the rows (spectra) is a combination of the old rows (spectra) based on the elements in the inverse of $\mathbf{T}$. As we know that the product of $\mathbf{C_{new}S_{new}}$ describes the data identically well as the product $\mathbf{CS}$ we immediately see that the decomposition is not mathematically unique. Neglecting any physical constraints, we see that the real physical solutions $\mathbf{C_a}$ and $\mathbf{S_a}$ lie in a set of solutions that is infinitely large (given there are an infinite number of choices for $\mathbf{T}$). So based on this knowledge, we can now understand that the critical step in transient absorption data analysis boils down not to finding a decomposition of the data matrix, but rather finding the actual (physical) decomposition of the data matrix $\mathbf{C_a}$ and $\mathbf{S_a}$ from within the theoretically infinite set of equivalently valid mathematical decompositions.

In order to achieve the goal introduced in the preceding paragraph of finding the physical decomposition of the measured data matrix $\mathbf{C_a}$ and $\mathbf{S_a}$ which reveal the concentration evolutions and spectra of the excited-state species really present, constraints based on physical insights into the system measured must be introduced. In the next two sections we will consider two techniques for introducing such physical constraints, and using them to search out the physically meaningful decomposition. The first technique requires quite explicit knowledge of the system under study, namely that the functional form of the rate equations for all excited-state species are known. Due to the necessity for such explicit knowledge, we call this approach *hard-modeling*. In the second section we introduce a technique that uses less explicit knowledge, such as the requirement that concentrations be positive, along with insight gained from the mathematical analysis of the measured data surface (such as local-rank information) to search for the physical decomposition. We call this second technique *soft-modeling*, as it can be applied in general to transient absorption data, without any prior knowledge of the reacting species or their kinetics. For both cases we consider the question of estimating how certain one is that the true physical $\mathbf{C_a}$ and $\mathbf{S_a}$ were found,

and illustrate this by applying each of the techniques to simple simulated data sets. For the second case, we introduce the technique we have developed in order to quickly and powerfully examine the uniqueness and physicality of the found solution in the case of a two-excited-state decomposition wherein one spectrum can be constrained from the data (this is the case present in chapter 6, and actually often occurs in energy conversion reactions in which excited-state species of very disparate lifetimes are involved).

2.4.1 Global analysis

The first technique we consider to find the physically meaningful matrix decomposition $\mathbf{C_a}$ and $\mathbf{S_a}$ is global analysis. This technique has a long history in the analysis of transient absorption data, and a good review of its current status was recently presented by van Thor and coworkers. [76]

In broad strokes, the most common implementation of this technique can be described in the following fashion. Firstly, the functional form of the population flow between the (known number of) excited-state species along with the boundary conditions of the initial population of each species must be known *a priori*. A general form of these equations is given in equation 2.19, where C_i is the concentration of the i^{th} excited-state species, and F_i is a function that governs the dynamics of the i^{th} population which takes in a vector of parameters ($\vec{p}_i$) and the populations. An explicit example of such a scheme of kinetic equations for a case in which an initial population of excitons can either decay to the ground state or form a pair of free charges which can then bimolecularly recombine is shown in equation 2.20. In this example F_1 is the decay to the ground state and the transfer to charge pairs given by $-k_1C_1 - k_2C_1$, $p_1 = (k_1, k_2)$, F_2 is the growth of charge pairs from the exiton population and their decay due to bimolecular recombination $k_2C_1 - k_3{C_2}^2$, and $p_2 = (k_2, k_3)$. The global fit is performed by using a non-linear least squares minimization routine (*lsqnonlin* in Matlab) to vary the parameter vectors $\vec{p}_1 \ldots \vec{p}_p$ in order to find a minimum of the least squares residual between the model and the data. The model is calculated for each set of input parameters in a two step process. First the concentration matrix is found by finding the numerical solutions to the population equations (using a solver

such as ode15s in Matlab) with the current parameter set. Once the concentration matrix (for the given step) is known, the corresponding best possible spectra matrix is quickly determined using a linear least square approach (like a matrix division in Matlab). The model is then computed by the multiplication of the concentration and spectra matrices and the residual at this step is calculated. The minimization routine continues to adjust the input parameters until a minimum difference exists between the model and the data, at which point $\mathbf{C_a}$ and thereby also $\mathbf{S_a}$ are found (given the population equations and initial conditions are indeed correct).

$$\begin{aligned}
\frac{\mathrm{d}}{\mathrm{d}t}C_1 &= F_1(\vec{p}_1, C_1, C_2, \ldots, C_p) \\
\frac{\mathrm{d}}{\mathrm{d}t}C_2 &= F_2(\vec{p}_2, C_1, C_2, \ldots, C_p) \\
&\vdots \\
\frac{\mathrm{d}}{\mathrm{d}t}C_p &= F_p(\vec{p}_p, C_1, C_2, \ldots, C_p)
\end{aligned} \tag{2.19}$$

$$\begin{aligned}
\frac{\mathrm{d}}{\mathrm{d}t}C_1 &= -k_1 C_1 - k_2 C_1 \\
\frac{\mathrm{d}}{\mathrm{d}t}C_2 &= k_2 C_1 - k_3 {C_2}^2
\end{aligned} \tag{2.20}$$

2.4.1.1 Global analysis applied to a simple example

In order to illustrate the global analysis technique, a simple example of a simulated dataset is considered here. It is assumed that two species are present in the dataset and that the decay of a species is proportional to its concentration. Two different models are applied to analyze the data: In the parallel model both species A and B are present from the start with the initial condition $C_A(t=0) = C_B(t=0) = 1$ while in the sequential model only A is present in the beginning and B is formed from A (initial condition: $C_A(t=0) = 1;\ C_B(t=0) = 0$). The following schemes of kinetic equations describe these simple models:

Parallel model:

$$A \xrightarrow{k_1} GS$$
$$B \xrightarrow{k_2} GS$$

$$\begin{aligned} \frac{\mathrm{d}}{\mathrm{d}t} C_A &= -k_1 C_A \\ \frac{\mathrm{d}}{\mathrm{d}t} C_B &= -k_2 C_B \end{aligned} \tag{2.21}$$

Sequential model:

$$A \xrightarrow{k_1} B \xrightarrow{k_2} GS$$

$$\begin{aligned} \frac{\mathrm{d}}{\mathrm{d}t} C_A &= -k_1 C_A \\ \frac{\mathrm{d}}{\mathrm{d}t} C_B &= k_1 C_A - k_2 C_B \end{aligned} \tag{2.22}$$

The results of the global analysis with the rate equations from equation 2.21 and 2.22 are presented in figure 2.19. Both parallel and sequential model fit the data equally well as can be seen from the solid lines overlaying the data points in figure 2.19. This means that both decompositions **CS** describe the data matrix **D** with the same accuracy. So in order to know that the decomposition obtained by global analysis is the physically correct decomposition into $\mathbf{C_a}$ and $\mathbf{S_a}$, one must be completely certain that the rigorously correct system of equations was chosen, and that the boundary conditions applied were correct.

In conclusion, global analysis is a useful tool to decompose an experimental data matrix. However, to obtain the physically meaningful decomposition into $\mathbf{C_a}$ and $\mathbf{S_a}$ it is crucial that the correct set of kinetic equations and boundary conditions are used. As seen in this simple example, it is often the case that more than one set of rate equations (and also more than one set of initial conditions) can lead to decompositions that give a high quality fit of the data. Therefore, the fact that a given kinetic model leads to a good fit of the data after global analysis is, in and of itself, not adequate evidence that the kinetic model is correct, or that the decomposition is indeed $\mathbf{C_a}$ and $\mathbf{S_a}$.

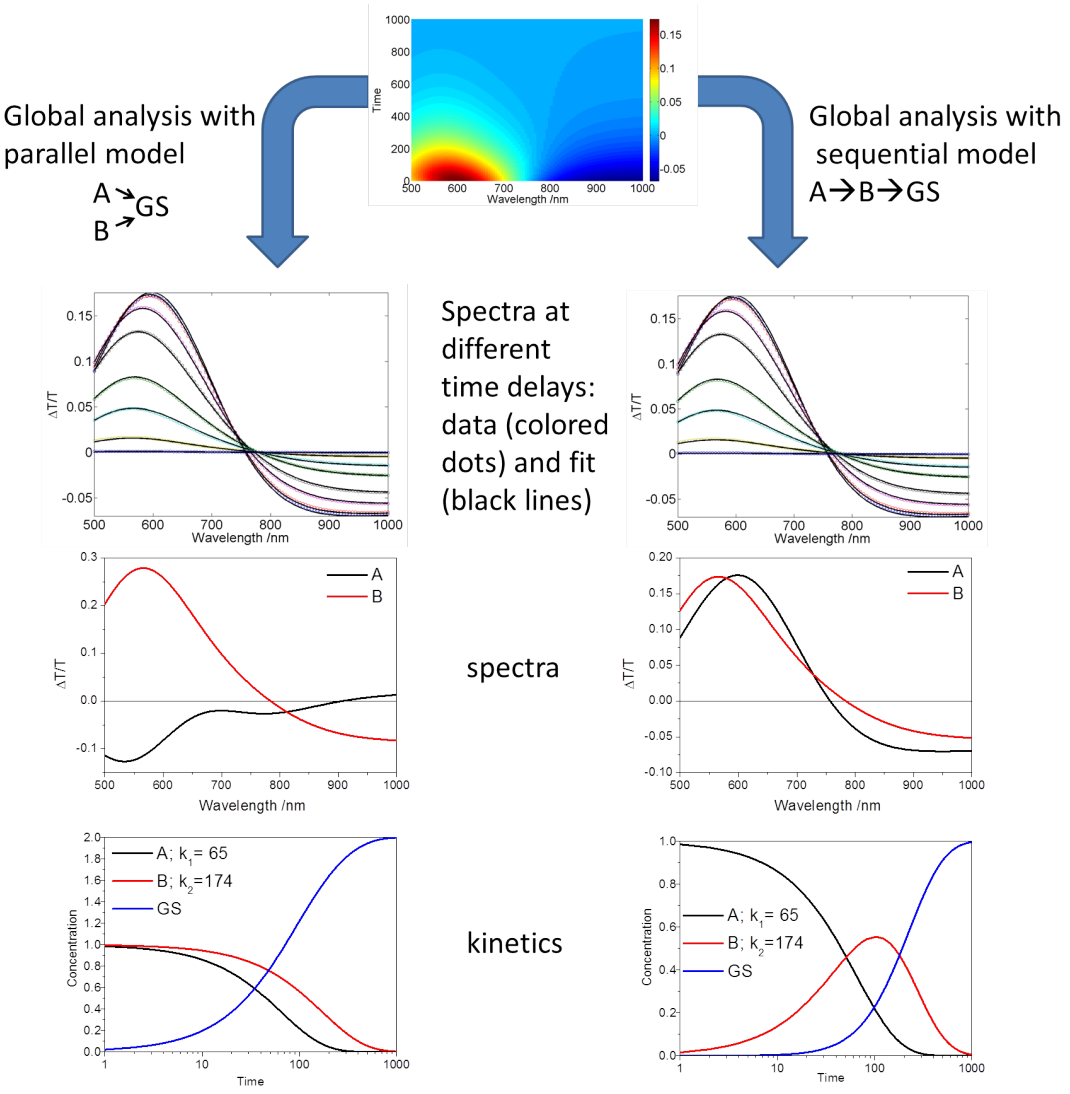

Figure 2.19: Result of global analysis on a simulated dataset. On the left-hand side the data matrix is fitted with a parallel model with two components A and B which both decay mono-exponentially with the respective decay constants k_1 and k_2. The right-hand side presents the fit with a sequential model with A and B also exhibiting mono-exponential decay with k_1 and k_2. The first panel on each side shows a comparison between the data (colored dots) and the fit (black lines) at time delays of 1, 10, 50, 100, 200, 300, 500 and 1000. Both models fit the data equally well. The ΔT/T spectra of the two components are shown in the second panel, the corresponding kinetics in the lower panel. GS denotes the ground state where ΔT/T=0 for all wavelengths.

In the next section we will investigate a data analysis approach that does not require such specific *a priori* knowledge of the population kinetics. It also provides an approach to examining the range of decompositions that accurately reproduce the observed data and satisfy the known physical constraints. This allows the experimenter to determine the bands of reasonable decompositions in which the physically true $\mathbf{C_a}$ and $\mathbf{S_a}$ must lie. In certain cases these bands can be quite narrow, and $\mathbf{C_a}$ and $\mathbf{S_a}$ can be precisely determined.

2.4.2 Multivariate curve resolution

Here we investigate how a physically meaningful decomposition can be approached by soft-modeling using constraints that can be obtained from basic physical knowledge and mathematical investigation of the observed data structure. This section presents the application of a multivariate curve resolution (MCR) method developed by Tauler and coworkers [77–80] to transient absorption data.

2.4.2.1 Initial guess

A schematic flowchart of the steps of the MCR process is shown in figure 2.20, in the following these steps will be explained in detail. First, information about the number of components and an initial guess of the concentration profiles is needed. This is done with evolving factor analysis (EFA), which is based on singular value decomposition (SVD). The singular value decomposition of a matrix $\mathbf{D}$ is a mathematical technique that factors any matrix into the product of three matrices:

$$\mathbf{D} = \mathbf{USV}^* \tag{2.23}$$

where $\mathbf{U}$ is a $(m \times m)$ matrix, $\mathbf{S}$ is a diagonal $(m \times n)$ matrix, and $\mathbf{V}^*$ (conjugate transpose of $\mathbf{V}$) is a $(n \times n)$ matrix. The diagonal elements of $\mathbf{S}$ are the singular values which are the square roots of the eigenvalues of $\mathbf{DD}^*$ arranged in decreasing order. The number of significant values in $\mathbf{S}$ gives the rank of $\mathbf{D}$. The columns of $\mathbf{U}$ and $\mathbf{V}$ are the singular left and right singular vectors of $\mathbf{D}$ which are the eigenvectors of $\mathbf{DD}^*$ and $\mathbf{D}^*\mathbf{D}$ respectively. In evolving factor analysis we will use SVD to do something similar to estimating matrix rank, so we will be concerned only with the values along the diagonal of $\mathbf{S}$.

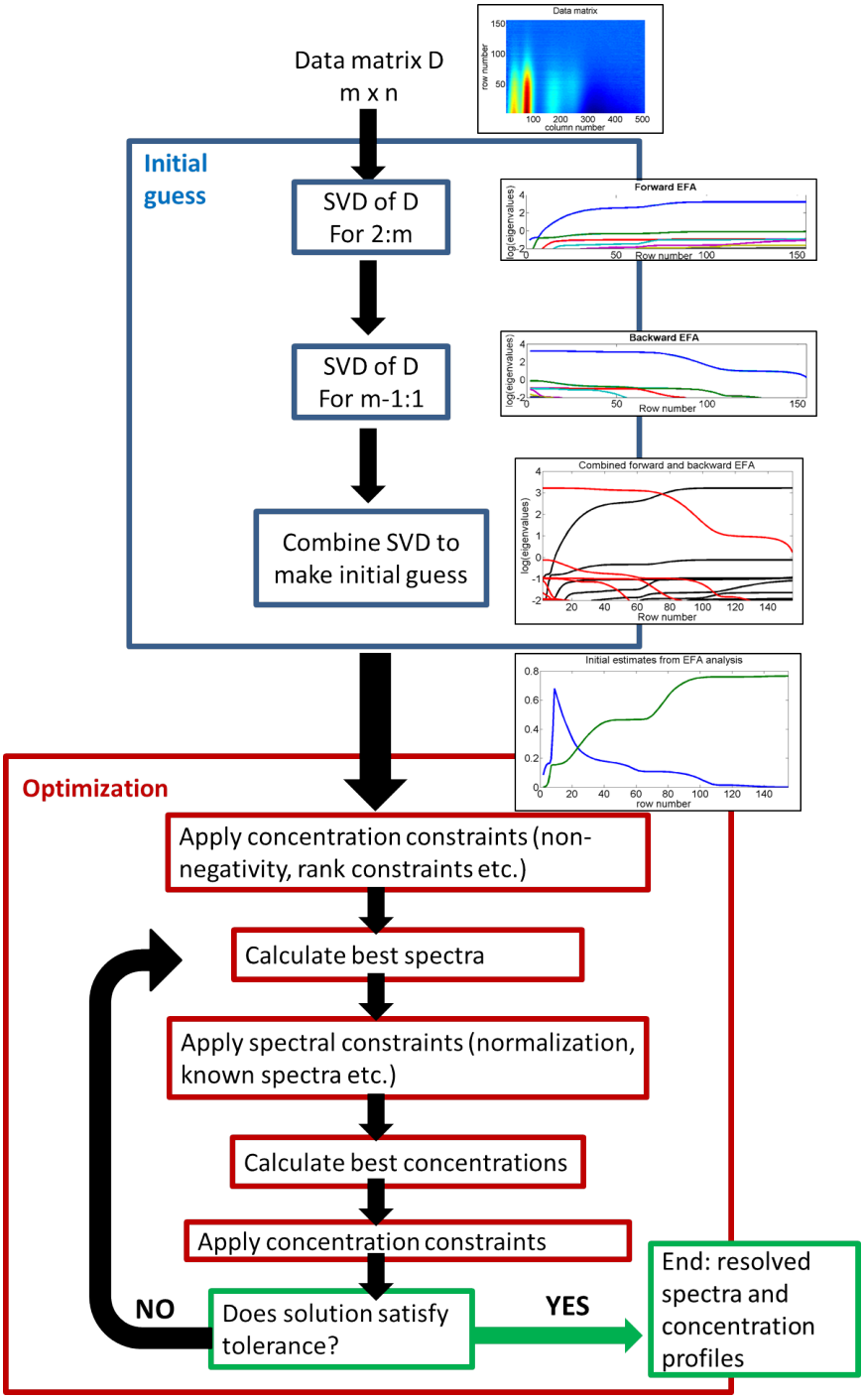

Figure 2.20: Schematic flowchart of the analysis done with MCR. The initial guess is obtained with evolving factor analysis, in doing a singular value decomposition on gradually enlarged datasets in the forward and backward direction. The optimization procedure involves the application of constraints and an iterative linear least square algorithm.

The basis of evolving factor analysis is to do SVD analysis on a sequence of submatrices and use the singular values to estimate how populations of excited states evolve with time. To start with, an SVD of a submatrix containing the first two columns of the data matrix is carried out and the singular values are plotted as points with their value as the y-value and an x-value of 1. Then SVD is done on the first 3 columns, and the singular values are again plotted but this time with an x-value of 2. This procedure of adding one more column, taking the SVD, then plotting the singular values at the next integer on the x-axis is repeated until there are no more columns to add. Lines are then drawn connecting the biggest singular value at every x point, the second-largest, third-largest, etc. This is called the forward-going EFA, and the increase of the second, third, etc., singular value with x (or timepoint) is indicative of the grow in of additional excited-state species at the times when the respective singular value line increases. In order to complete the EFA, a second graph is made in the backward-going direction. This is made by starting with only the last two columns, and adding one column to the left after each iteration. Looking at when the second, third, etc. component increase in this plot shows when excited-state species disappear from the data matrix. In order to make an approximate guess of the concentration profiles for a starting position of the MCR-ALS algorithm, it is assumed that the species first present in the data are the first to disappear. Looking at the EFA and the motion of singular value lines relative to the noise level, an estimate of the number of excited-state species, p, is made. The initial concentrations are then estimated by iterating i from 1 to p and taking the ith component of the forward-going EFA until it intersects with the (p-i+1)th component of the backward-going EFA from which time the (p-i+1)th component of the backward-going EFA is taken to give the excited-state concentration. From EFA we can also identify if a region at late time exists where one component is sufficient to describe the data matrix. If only one singular value is necessary to describe the data matrix for a long time in the backward-going EFA, then it can be concluded that only a single species accounts for the absorption left at long time. Such information is very useful, as will be shown later.

2.4.2.2 Optimization process

This initial guess for the concentration profiles is then used in the optimization process: First, the constraints are applied to the concentration profiles. Possible constraints are that the concentrations should always be positive (non-negativity constraint), have only one peak (unimodality constraint) or rank constraints which can be obtained from EFA. With these concentration profiles, the best spectra are calculated in Matlab with a right matrix division $\mathbf{S}^T=\mathbf{C}/\mathbf{D}$. This is done with a least square calculation which is equivalent to finding the pseudoinverse of the concentration ($\mathbf{C}^+$): $\mathbf{S}^T=\mathbf{C}^+\mathbf{D}^*$. The calculated spectra can be adjusted by constraints such as normalization, or known spectra of one or a number of excited-state species. From there the concentration profiles are calculated again using the least square method. Subsequently, the constraints are applied to the concentration profiles and it is assessed whether the solution satisfies the tolerance. If this is not the case, the next fitting round starts by calculating the spectra. If the tolerance is satisfied, then the current spectra and concentration profiles are shown, as they adequately describe the data and meet all of the physical constraints. These are then a decomposition that is physically reasonable, however we do not yet know whether or not this decomposition has given us $\mathbf{C_a}$ and $\mathbf{S_a}$. Depending on the soft constraints and the data, these concentration and spectra may be practically unique (ignoring scale uncertainty) or it may still be possible to find some invertible matrices, see equation 2.18 on page 35, which mix the components of the solution found by the MCR-ALS procedure and result in new concentration and spectra profiles that still satisfy the physical constraints. We will examine some methods for considering the uniqueness of the solution found by MCR-ALS in the coming sections. This will develop the understanding of whether the solution gives reliable insight into the true physical processes or whether a band of possible processes could all describe the experimental observations equally well.

2.4.2.3 Data augmentation

Before we turn to determining the uniqueness of the MCR-ALS solution, we will present a method that is broadly useful for making the solution as unique as pos-

sible. This technique relies on the fact that often some reaction rates that affect the transient absorption data surfaces are non-linear. This means that they occur at different rates after different initial population densities are created after excitation with different pulse fluences. Thus, by taking transient absorption surfaces for the same sample at a series of different excitation fluences, we can create an 'augmented' transient absorption surface by placing the individual surfaces on a common wavelength axis and an extended time axis as shown in figure 2.21. Performing MCR-ALS on this augmented data set is possible, the spectra of the species are the same for all of the individual experiments, and the concentration profiles, although different, are found as augmented vectors wherein the unique evolutions of the species for the different fluences are appended to each other (just as the surfaces were). Usually, the data is normalized before augmentation to weight variances during optimization more equally. The fact that the various concentration profiles for each experiment must all simultaneously satisfy the soft constraints imposes a greater constraint on this overall augmented solution. This constraint means that the range of possible solutions is decreased, and that more precise insight into the physical decomposition can be gained.

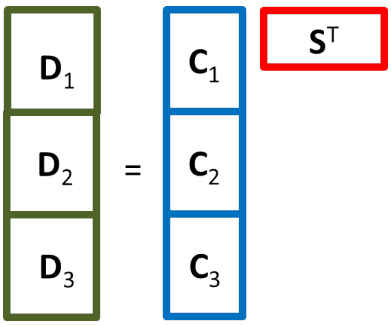

Figure 2.21: Column-wise augmentation of datasets merging into one data matrix which is represented by common spectra and individual concentration profiles.

2.4.2.4 Exploring the linear transformation ambiguity

As introduced in equation 2.18 on page 35 we can create new spectra and concentration profiles that are identically mathematically valid by taking linear superpo-

sitions of the found concentration and spectra vectors using an invertible matrix **T**. In this section we present some methods for exploring how many **T** matrices exist that mix the concentration and spectra vectors found by MCR-ALS and result in new vectors which still satisfy the known soft constraints. We do not, as of yet, know of a general solution to this problem for an arbitrary number of components. However, we present results that are useful for commonly occurring cases where only two excited-state species are present. These special cases cover a large number of cases in energy conversion reactions.

Let us now consider the form of the linear transformation matrix **T**. Specifically, we will see that it is useful to split **T** into the product of a mixing matrix **M** and a scaling matrix **F**, both of which must be invertible. The scaling matrix is a diagonal matrix with constants along its diagonal, $\mathbf{F_{ii}} = a_i$, and zero off-diagonal elements. The mixing matrix then has a diagonal of ones, and off-diagonal elements are each a constant. The scaling matrix represents a scaling of a concentration profile by a given constant, and the associated spectra by the inverse of the same constant. This clearly leaves the surface created from the outerproduct of that spectra and concentration profile unchanged. In order to settle the scale uncertainty, some absolute information regarding the species cross section or population boundary conditions are necessary. However, we are often interested in establishing the normalized concentration evolution and spectral shape (if just as a first step). Therefore, in the first step we are not interested in the scaling matrix, but in the mixing matrix (that actually changes the normalized concentration and spectral profiles). We can learn about the uniqueness of the (normalized) solution with respect to the mixing matrix, without considering the exact scaling. In the following subsections, the practical utility of this separation will be demonstrated.

Linear Transformation with Two Populations

If the transient absorption surface can be described by two excited-state species then **T** must be a 2×2 matrix with a non-zero determinant. It can be expressed in terms of **M** and **F** as shown in equation 2.24. The inverse of **T** can also be expressed in terms of **M** and **F** as shown in equation 2.25. Equation 2.26 illustrates how the data surface is generated from the obtained concentration

and spectral profiles, and how an equivalent surface can be generated by new matrices given by the product of the original vectors and the mixing matrix (and its inverse). In this case, the scaling vectors are multiplied together and give the identity matrix. In order to compare solutions, we generally renormalize the spectra after rotation to have unit length, and also make the appropriate rescaling of the concentration profile. This allows convenient visual comparison of the mixed vectors, whose forms are shown in equation 2.27.

$$\mathbf{T} = \mathbf{MF} = \begin{pmatrix} 1 & b \\ c & 1 \end{pmatrix} \begin{pmatrix} a & 0 \\ 0 & d \end{pmatrix} \tag{2.24}$$

$$\mathbf{T}^{-1} = \mathbf{F}^{-1}\mathbf{M}^{-1} = \begin{pmatrix} \frac{1}{a} & 0 \\ 0 & \frac{1}{d} \end{pmatrix} \frac{1}{1-bc} \begin{pmatrix} 1 & -b \\ -c & 1 \end{pmatrix} \tag{2.25}$$

$$\begin{aligned} &\mathbf{CS} = \begin{pmatrix} \vec{C}_1, & \vec{C}_2 \end{pmatrix} \begin{pmatrix} \vec{S}_1 \\ \vec{S}_2 \end{pmatrix} = \vec{C}_1 \otimes \vec{S}_1 + \vec{C}_2 \otimes \vec{S}_2 = \mathbf{Surf}_1 + \mathbf{Surf}_2 = \dots \\ &\dots = \mathbf{CTT}^{-1}\mathbf{S} = \mathbf{CMFF}^{-1}\mathbf{M}^{-1}\mathbf{S} = \dots \\ &\dots = \begin{pmatrix} \vec{C}_1 + c\vec{C}_2, & b\vec{C}_1 + \vec{C}_2 \end{pmatrix} \begin{pmatrix} \vec{S}_1 - b\vec{S}_2 \\ -c\vec{S}_1 + \vec{S}_2 \end{pmatrix} \frac{1}{1-bc} \end{aligned} \tag{2.26}$$

$$\begin{aligned} \vec{C}_{1new} &= \vec{C}_1 + c\vec{C}_2 \\ \vec{C}_{2new} &= b\vec{C}_1 + \vec{C}_2 \\ \vec{S}_{1new} &= (\vec{S}_1 - b\vec{S}_2)\frac{1}{1-bc} \\ \vec{S}_{2new} &= (-c\vec{S}_1 + \vec{S}_2)\frac{1}{1-bc} \end{aligned} \tag{2.27}$$

Examining the form of the mixed vectors shown in equation 2.27, we can make some general observations. First, in order that the determinant is non-zero $bc \neq 1$. If both b and c are large, then $\vec{C}_1$ is switched with $\vec{C}_2$ and $\vec{S}_1$ with $\vec{S}_2$. This is a trivial case. As b and c both approach 1 (or -1), then the concentration profiles become very similar, and the spectra approach a mirroring of each other through the x-axis. With the similarity of the concentrations, this parameter choice leads to the most parallel-like solutions. In order to judge the physicality of these solution, constraints regarding the shape of the spectra are useful. For example if the states have a common absorption bleach, observing when this feature stops looking similar in the two spectra is useful. For the case

of approaching -1, then positivity of the concentration profiles is also useful. To make solutions more sequential-like, rotations can be found that push the initial population of one concentration profile towards zero, and the other towards a higher level at early time. Depending on which population profile one wishes to push towards zero, b and c can be selected by looking at the initial conditions of the resolved $\vec{C_1}$ and $\vec{C_2}$. A standard analysis procedure is to calculate the mixed vectors over a mesh of b and c values and highlight the regions where the non-negativity constraints are satisfied. This reveals all the possible concentration and spectra profiles which can describe the observations. From this, one gains a detailed insight into how certain one can be regarding the concentration evolution and spectra of given components.

In energy conversion reactions, it is not uncommon that one species is much longer-lived than the others. For example, when an exciton population (with an un-quenched lifetime on the sub-nanosecond scale) creates long-lived charges, we know that the signal left after a nanosecond comes exclusively from the long-lived charges. That means we know exactly what the (normalized) spectrum of the charges is. This knowledge of the spectral shape of a single component significantly simplifies the examination of the linear mixing ambiguity. First of all, when we do the MCR-ALS analysis, we can constrain the spectral shape of one of the species (let us assume that we constrained the first species to represent the charges). Then, we know that $\vec{S_1}$ is the correct spectrum, so that b must equal zero. This has the immediate consequence that the population evolution of the other species, that is $\vec{C_2}$, is precisely known! This rather surprising result can be very useful, as we will see in the coming sections. On the other hand, the spectra of the other species $\vec{S_2}$, and the population evolution of the species with the known spectra, $\vec{C_1}$, can still be changed by mixing. The validity of the mixed solutions can be in this case checked by running a linear sweep of c from positive to negative values. This will be demonstrated in the next section.

Such an analysis can be extended for greater number of components, although it is clear that as the number of components grows, the parameter space for mixed solutions quickly expands.

2.4.2.5 MCR applied to a simple example

In order to illustrate the process of analyzing a data matrix with MCR-ALS the simulated dataset which was analyzed in section 2.4.1.1 with global analysis is decomposed and investigated with MCR-ALS here. Figure 2.22 shows a flowchart of the analysis process: First, forward and backward evolving factor analysis are carried out, from which two components are identified to be sufficient to explain the dataset as their eigenvalue is distinctly larger than the eigenvalue of the other components. The initial guess is taken from EFA as described in section 2.4.2.1 and the ALS optimization is started, with the constraint that the concentrations should be non-negative. From EFA we know that the matrix is rank 1 at longer times, therefore only one species (A, shown in green) is known to be left in the end. Therefore we can introduce an additional constraint, namely that the spectrum of species A is known, as it is the spectra which is found in the data matrix at long time delays. From the optimization process as depicted in the lower panel of figure 2.20 we obtain the concentration profiles of the species A and B and the before unknown spectrum of species B (shown in the lower panels of figure 2.22).

Linear transformation ambiguity

However, the analysis is not complete at this point even though the quality of the fit in terms of residuals is very good. As discussed in the previous section, we have to investigate the ambiguity due to possible linear transformations. In the current example we found that the matrix becomes essentially rank 1 after 200 ps. This means that we know the spectrum of the long-lived component with certainty (it is the spectra measured at long times) and only have a single parameter c that influences the rotation. Figure 2.23 shows how the variation of this parameter affects the concentration and spectral profiles. We see that by choosing positive values of c the solution is rotated to a more parallel-like model, where the populations tend to monotonically decay. Rotation too far in this direction leads to spectral shapes that are mirror-images of each other, and are likely to be physically unreasonable, as either induced absorption or absorption bleach is often expected for both species in given wavelength ranges. Rotation with negative c values leads to more sequential-like models. The limit of negative

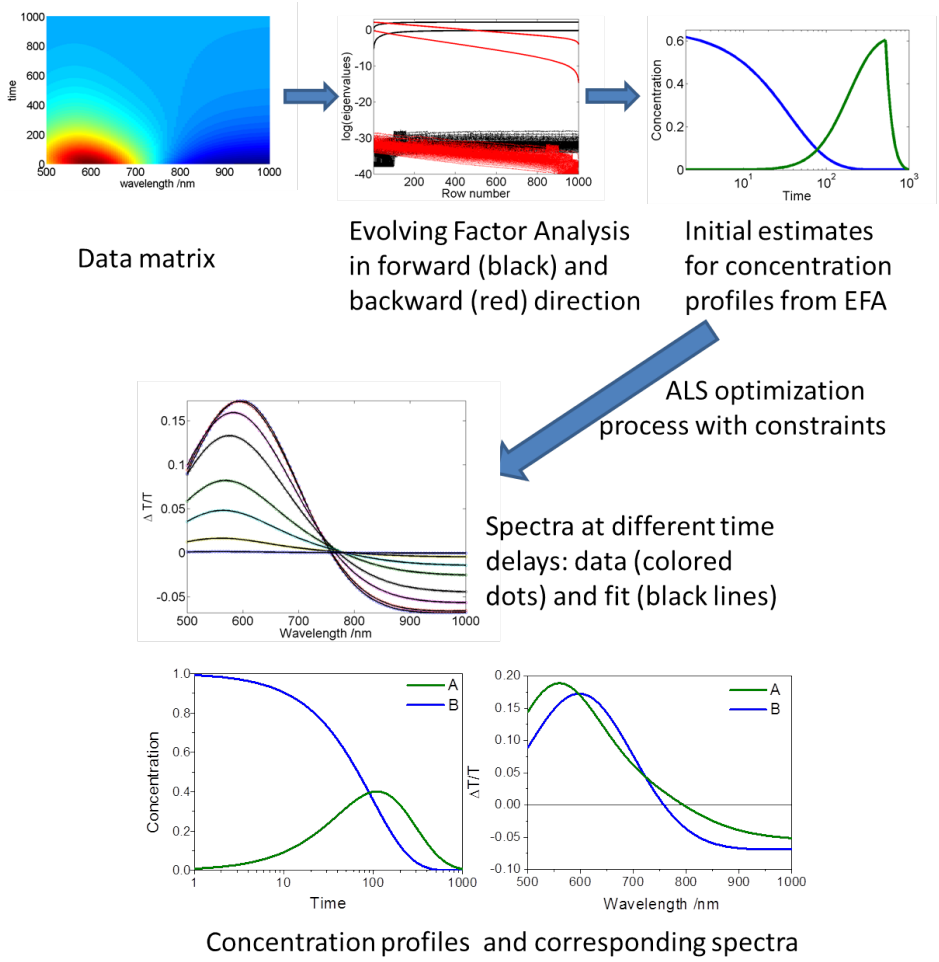

Figure 2.22: MCR-ALS analysis applied to a simulated dataset. EFA gives the initial estimates for the concentration profiles. The ALS algorithm incorporating constraints yields the spectra and concentration profiles shown in the bottom of the panel. The graph in the middle presents a comparison between the data (colored dots) and the fit (black lines) at time delays of 1, 10, 50, 100, 200, 300, 500 and 1000.

rotation is easy to find as a concentration profile starts to go negative at this threshold value. In this way, a clear band of possible factorizations (in which the true physical factorization will be contained) can be simply generated by this soft-modeling approach.

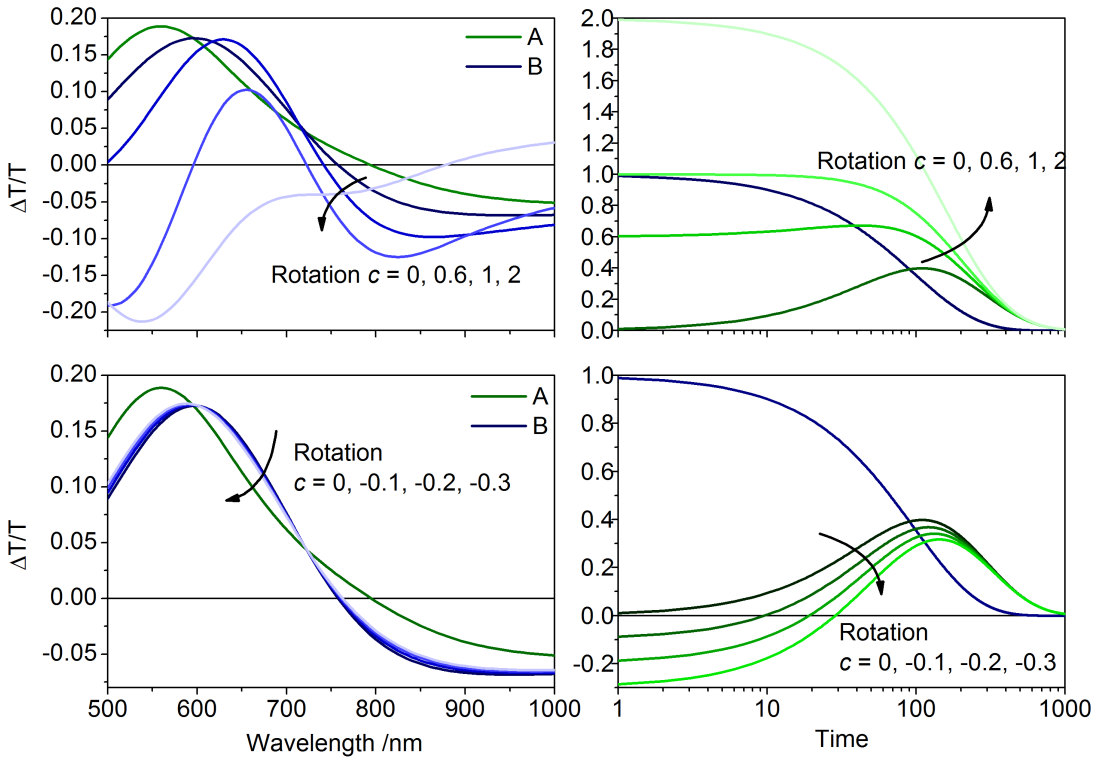

Figure 2.23: Determining the rotational ambiguity of the MCR-ALS analysis applied to a simulated dataset. The upper panel shows how positive c values rotate the solution to more parallel-like models. Rotation to the positive eventually leads to spectra that become almost mirror images of each other. These are rarely likely to be physically reasonable solutions. Rotations with negative values of c are shown in the bottom panel. These move the decomposition to a more sequential-like solution. In the current case, the resolved solution was the most sequential possible as we see that further rotation leads to negative populations. The plot of residuals is equal for all linear transformations.

2.4.3 General conclusions regarding hard and soft modeling

In this section we have examined two methods for extracting concentration and spectral profiles from transient absorption data. In the section on global analysis by hard-modeling we saw that good fits to the data surface could be generated using a system of parametrized rate equations. It is vitally important to note though, that many different systems of equations could fit a given dataset very well. So the simple observation that a given rate equation system yields a good fit in a global fitting approach is not sufficient evidence that the concentration profiles so-obtained are the physically correct ones! Global fitting only extracts the physically correct factorization if the system of rate equations are correct, this must be carefully considered and physically justified. Basing the argumentation of physical correctness on the goodness of the fit must be approached with extreme caution in the case of global analysis. Soft-modeling, on the other hand, finds a factorization which obeys some known soft constraints, such as non-negativity in the concentration profiles, and known spectral information if available. In the same way that many different systems of rate equations can lead to good global fits, the concentration and spectra profiles found by MCR-ALS are usually not unique. However, the uniqueness of the MCR-ALS solution can be explored by mixing the found solution with linear transformation matrices. This allows the researcher to see the full range of possible solutions that satisfy the most rigorously known constraints. From the solutions it is often possible to make further assumptions, for example relating to spectral form, which can lead to a better constrained estimate of the factorization. In any case, we feel that a general advantage of the soft-modeling technique is that the linear transformation uncertainty is clearly apparent throughout the analysis, and false 'certainty' in the factorization (often an unwanted by-product of global analysis) can thus be avoided. If the data surface can only be explained by a unique factorization, it can be found by soft-modeling. If additional insight is needed to find the physical decomposition, soft-modeling can provide clear insight into exactly how additional information can further constrain the solution bands. It provides a

useful analytic tool to guide experimental effort and rigorously determine the valid physical decomposition of transient absorption surfaces.

Chapter 3

Experimental Methods

3.1 Organic solar cells

3.1.1 Device preparation

The standard organic solar cell device structure is depicted in figure 3.1. A glass substrate is used with a transparent electrode made by a structured film of indium tin oxide (ITO). To prepare the cell, the substrate is cleaned in an ultrasonic bath with a series of solvents. After argon plasma-etching to clean and activate the ITO, a layer of PEDOT:PSS (poly(3,4-ethylendioxythiophene)-poly(styrenesulfonate); (Clevios P VP AI 4083, H.C. Starck)) is deposited by spincoating (3000 rpm, 40 s). The samples are transferred to the glovebox and subsequently annealed to remove residual water in the PEDOT film (150 °C, 20 min). PEDOT is a transparent, highly doped polymer which acts as a hole transporter. It compensates for the surface roughness in the ITO layer which could lead to short circuits in the cell. On the anode, the photoactive blend is spin cast from a common solution in an organic solvent onto the PEDOT layer. Aluminum electrodes (100 nm) are vacuum evaporated through a mask on top of the active layer to form the cathode. The active area of the pixels as defined by the overlap of anode and cathode area is 14 mm^2. If a solar cell needs to be measured several times, conductive silver paste is applied on the electrodes to protect them from scratches.

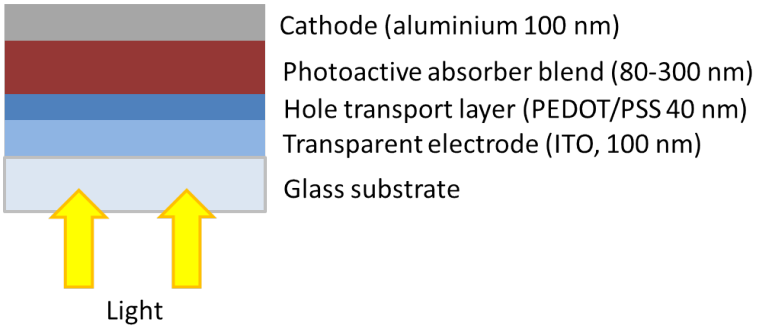

Figure 3.1: Standard assembly of an organic solar cell with typical layer thicknesses.

3.1.2 Device characterization

3.1.2.1 Current-voltage characteristics

The J-V curve, where the output current is measured as a function of the voltage applied to the electrodes under illumination, reveals the figures of merit that describe the performance of a solar cell. The standard illumination conditions which are typically used in laboratories correspond to a simulated air mass 1.5 (AM 1.5) solar spectrum at 25 °C with an irradiance of 1000 W/m^2 (= 100 mW/cm^2). AM 1.5 means a solar spectral irradiance that can be found as solar light has crossed 1.5 times of the atmosphere relative to that at the zenith at sea level. This is found at a zenith angle of 48.2 °.

Figure 3.2 shows an example of a J-V curve and the figures of merit:

- The open circuit voltage V_{OC} is the voltage where no net current flows in the external circuit (maximum voltage obtainable from device).
- The short circuit current density J_{SC} is the current when the applied voltage is 0 (maximum current extractable from device).
- The maximum power point (mpp) is the the point on the J-V curve where the power output P_{mpp}, the product of voltage V_{mpp} and current J_{mpp}, reaches a maximum.

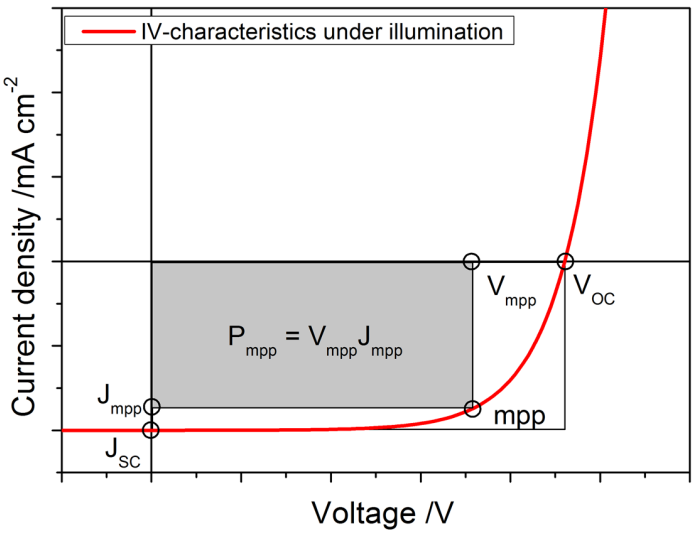

Figure 3.2: Current voltage characteristics of a solar cell under illumination. See text for details.

The most important figure of merit for a solar cell is its energy conversion efficiency η. It is defined as the ratio of the power output at the maximum power point to the input light irradiance P_{Light}:

$$\eta = \frac{J_{mpp} \cdot V_{mpp}}{P_{Light}} \tag{3.1}$$

The fill factor FF is defined as the ratio of the maximum, actually obtainable, power output at the mpp to the theoretical, but not actually obtainable, power output $J_{SC} \cdot V_{OC}$:

$$FF = \frac{P_{mpp}}{J_{SC} \cdot V_{OC}} = \frac{J_{mpp} \cdot V_{mpp}}{J_{SC} \cdot V_{OC}} \tag{3.2}$$

In this work, the solar cell performance is characterized with a commercial solar simulator (K.H. Steuernagel Lichttechnik GmbH, Germany) at an area power density of 70-80 mW/cm^2. The J-V curves are recorded with a Keithley 2400 digital source-measure unit.

3.1.2.2 External and internal quantum efficiency

The external quantum efficiency (EQE) is defined as the ratio of collected electrons N_{el} to the number of **incident** photons N_{ph}:

$$EQE(\lambda) = \frac{N_{el}(\lambda)}{N_{ph}(\lambda)} \tag{3.3}$$

The internal quantum efficiency (IQE) is a very useful tool as electronic properties are separated from optical properties. It is defined as the ratio of collected electrons to the number of **absorbed** photons N_{abs}:

$$IQE(\lambda) = \frac{N_{el}(\lambda)}{N_{abs}(\lambda)} \tag{3.4}$$

The EQE is straightforward to measure: the short circuit current I_{SC} is measured as a function of wavelength and divided by the number of incoming photons measured with a reference cell. In our setup the monochromatic light is generated with a tungsten halogen lamp and a TRIAX 180 monochromator. A calibrated silicon photodiode is used to measure the number of incident photons. Theoretically (if the cell is operating in the linear regime at J_{SC} up to solar illumination intensities), integrating the EQE over the whole wavelength range, J_{SC} should be obtained:

$$J_{SC} = \frac{e}{hc} \int \lambda \cdot EQE(\lambda) \cdot P_{AM1.5}(\lambda)\, d\lambda \tag{3.5}$$

However, as the light source for the EQE measurement is much lower in power than solar illumination, deviations due to loss mechanisms depending on charge carrier density might occur.

The IQE on the other hand is more difficult to determine; it can be calculated using the measured EQE if the exact absorbance $A(\lambda)$ of the active layer of the sample is known:

$$IQE(\lambda) = \frac{EQE(\lambda)}{1 - 10^{-A(\lambda)}} \tag{3.6}$$

However, measuring the absorbance of a sample, i.e. with an integrating sphere, is arduous as many effects have to be considered, such as parasitic absorption of other layers, reflection in the photoactive layer and interference effects. Therefore, a transfer matrix approach was used in this work which was developed by

Burkhard and coworkers.[81] In a transfer matrix approach the active layer absorption is modeled by taking into account the reflection and the transmission at each interface and the attenuation in each layer.[82, 83] To calculate the parasitic layer absorptions their n and k values (real and imaginary part of the index of refraction) are taken from the literature. For the photoactive layer $n = 2$ for all wavelengths is assumed, and k can be calculated from the absorption coefficient α (as introduced in equation 2.2 and 2.3 on page 10) with $k = \frac{\lambda\alpha}{4\pi}$. α is determined from a simple absorption measurement on a thin film of the photoactive materials: $\alpha = \frac{\mathrm{OD}\ \ln 10}{x}$, where OD is the optical density (also called absorbance) measured with the spectrometer and x is the film thickness determined by profilometry.

A sample result from the transfer matrix calculation is shown in figure 3.3. The IQE can now be calculated by simply dividing the EQE by the calculated absorption of the photoactive layer.

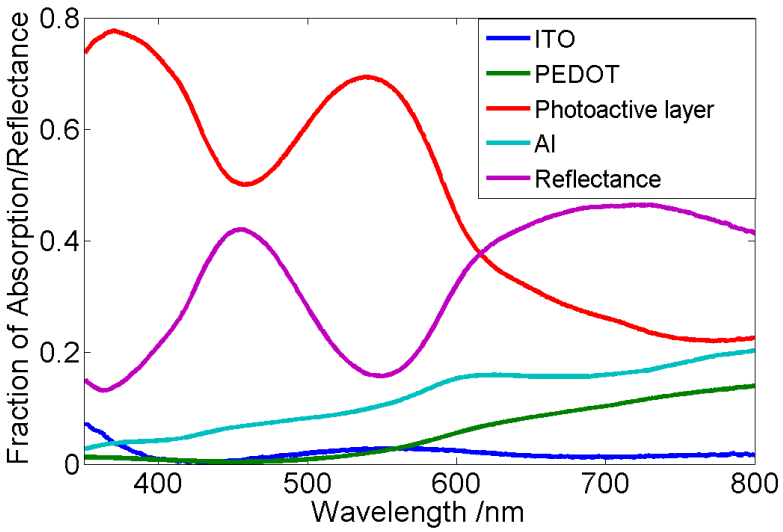

Figure 3.3: A sample result of transfer matrix calculations [81] for the absorption of the photoactive and parasitic layers and the reflection. The IQE is subsequently calculated by dividing the EQE by the absorption of the photoactive layer.

3.2 Pulsed charge extraction experiments

Pulsed charge extraction experiments are useful to investigate trapping and detrapping processes in organic solar cells which is of importance for the analysis in chapter 4. Similar techniques to the one employed here have been presented in the literature.[84, 85]

Samples are prepared as described in section 3.1.1 and measured in vacuum. A light emitting diode (LED) is positioned directly in front of the solar cell. The LED is triggered with a function generator (TTi, TGA 1242, 40 MHz Arbitrary Waveform Generator) and by varying the current supply, the LED intensity can be varied in the range of 0.01 to 0.7 equivalent suns. The calibration is done with a silicon photodiode and the rise/fall time of the light is thus determined to be less than 50 ns. The LED is operated in a pulsed mode, i.e. it is switched on for a certain time, e.g. 300 μs, then switched off for a defined time, e.g. 700 μs, then switched on again and so on. The photocurrent in the device is measured with a digitizing oscilloscope (Tektronix TDS 524A, 500 MHz) with an input impedance of 50 Ω. The electric circuit of the experiment is shown in figure 3.4(a). An example of the results for the illumination with different light intensities is given in figure 3.4(b): the upper panel shows the LED operation as measured by the reference diode (here the LED is switched on for 100 μs in each cycle), the corresponding measured photocurrent in the device is shown in the lower panel.

3.3 Time-resolved photoluminescence spectroscopy

Time-resolved photoluminescence (PL) spectroscopy is a powerful tool to measure radiative decay processes in an excited sample on timescales from few ps to 1 μs. Its working principle is schematically depicted in figure 3.5. For measurements in the short time range (few ps to 2 ns) the sample is excited with the output of a Ti:Sapphire ultrafast laser oscillator (Coherent Mira 900) with a repetition rate of 80 MHz and a pulse length of 100 fs. The oscillator is pumped by a diode pumped solid-state laser (Coherent Verdi V8). As excitation wavelength either the ~800 nm output or the frequency doubled ~400 nm is used. The light

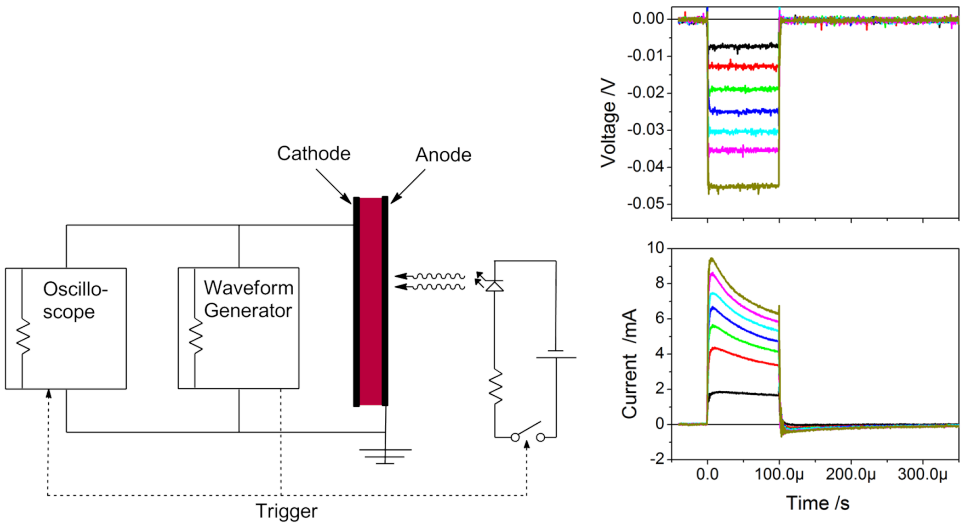

(a) (b)

Figure 3.4: Panel (a) shows the electric circuit diagram of the pulsed charge extraction experiment. Panel (b) depicts exemplarily the results of such an experiment at different LED intensities measured with a reference diode (upper panel) and the corresponding current transients in the device (lower panel). The different colors correspond to the different illumination intensities.

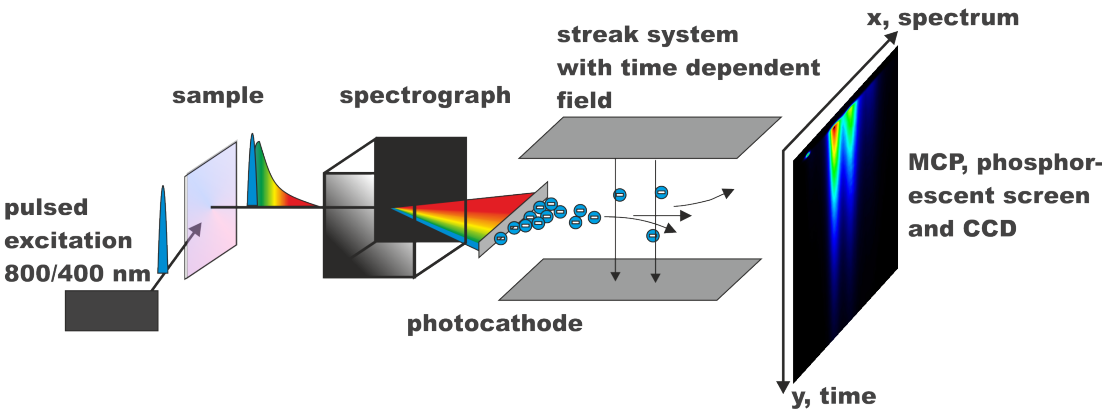

Figure 3.5: Schematic illustration of a time-resolved photoluminescence experiment.

emitted from the sample is collected with a telescope and then focused into a Hamamatsu Streak Camera system. In order to spectrally resolve the incoming light, it is diffracted by the spectrograph in the horizontal direction (as shown in figure 3.5). A photocathode then converts the photons into electrons. A time-dependent electric field in the y-axis is applied which deflects the electrons in different angles in the vertical direction depending on their time of arrival. A micro-channel plate is used to multiply the electrons which are then converted back into light on a phosphorescent screen; a two dimensional CCD camera finally records the number of photons. We thus obtain an image of the PL of the sample that is spectrally resolved in the x-axis and time-resolved in the y-axis.

3.4 Photoinduced absorption spectroscopy

3.4.1 Transient absorption spectroscopy

The signals measured in transient absorption (TA) spectroscopy were already introduced in section 2.3.4, this section presents the experimental setup as schematically depicted in figure 3.6.

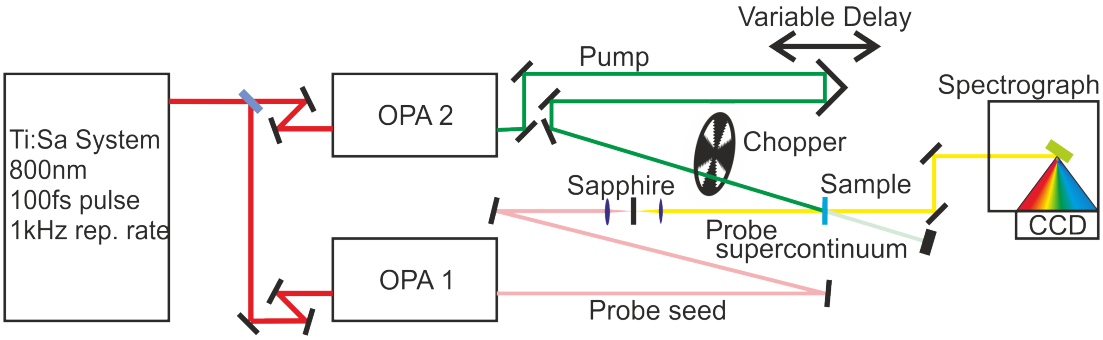

Figure 3.6: Experimental setup of our transient absorption experiment. Panel adapted from [86].

For white light generation the 800 nm output of a Ti:Sapphire laser system (Coherent Libra HE) with a pulse duration of 100 fs and a repetition rate of 1 kHz is coupled into an OPA (Coherent OPerA Solo Topas system) where signal

at 1300 nm and idler at 2100 nm are created (see section 2.3.3 for theoretical details). This output is then focused into a nonlinear medium (e.g. sapphire) creating the spectrally broad white light pulse (see section 2.3.2). For the visible to near infrared (NIR) wavelength region (450-1000 nm) the signal of the OPA is used, for the NIR to IR (1100-2000 nm) the idler is used to generate the white light.

For measurements in the short delay range (from 1 ps to 4 ns) a pump beam is generated with the second OPA. A wavelength range from 285-1130 nm can be accessed depending on the use of idler, signal, second and third harmonic signal or sum frequency signal. The variable time delay between pump and probe beam is realized with a broadband retro-reflector on a mechanical delay stage (Newport, 600 mm travel range). The pump beam is chopped to block every second pulse (with a frequency of 500 Hz) so that $\Delta T/T$ can be calculated from subsequent detector readings. For measurements in the long delay range (from 1 ns to 1 ms) an actively Q-switched Nd:YVO_4 laser (AOT Ltd. MOPA) operating at 532 nm is used. The time delay between pump and probe beam is introduced by an electronic delay generator (Stanford Research Systems DG535). Both in short delay and in long delay the polarization of the pump beam is set to magic angle (54.7°) with respect to the white light beam polarization to avoid measuring polarization relaxation influenced kinetics.

The white light is focused onto the sample and is overlapped with the pump beam. It is detected in a linear silicon array spectrograph (Hamamatsu NMOS linear image sensor S3901-256/512) for the visible and a Peltier-cooled linear extended InGaAs array (Entwicklungsbüro Stresing) for the NIR spectral region.

The TA measurements are performed at room temperature or at liquid nitrogen temperature (77 K) under dynamic vacuum at pressures $< 10^{-4}$ mbar. The samples are prepared on quartz substrates that are cleaned and plasma etched in the same way as the solar cell devices described in section 3.1.1. The materials are spin-coated from solution onto the substrate with the same conditions as in the solar cell devices.

3.4.2 Quasi steady-state PIA spectroscopy

In order to determine the spectra of long-lived ($\sim\mu$s) excited-state species, such as charges or triplets, photoinduced absorption (PIA) spectroscopy is carried out in quasi steady-state mode. Here, the detected signal at a given wavelength is proportional to the product of the number of excited-state species causing that signal and their lifetime.

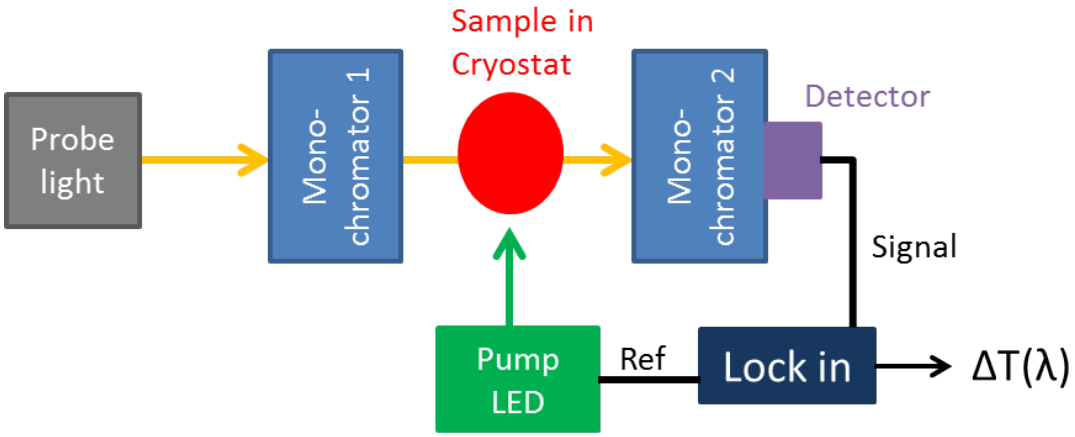

Figure 3.7: Experimental setup of the quasi steady-state photoinduced absorption measurement. For the transmission measurement a chopper is inserted behind the first monochromator which provides the reference for the lock-in.

The measurements are carried out at liquid nitrogen temperature (77 K) as decay processes are slowed down at that temperature and therefore a higher remaining signal can be measured. Helium is used as contact gas to ensure an inert atmosphere and avoid any condensation. A schematic diagram of the experimental setup for measuring PIA is shown in figure 3.7. The probe white light is provided by a 100 W tungsten halogen light source (Müller Elektronik Optik DUO150). A monochromator (LOT Oriel Omni-v 300) selects the wavelength to be measured in the range from 500 nm up to 4500 nm. The sample is excited with a high power green LED (Newport LED-527-HP) centered at 527 nm. Excitation and probe beam are perpendicular to each other. A second monochromator behind the sample ensures that only the selected probe wavelength is measured.

Three different detectors are available: an amplified silicon detector (Thorlabs PDA 100A) for the visible to NIR region (500-1100 nm), an amplified germanium detector (Thorlabs PDA 50B) for the NIR region (900-1700 nm) and an amplified nitrogen-cooled indium antimonide detector (Teledyne-Judson J10D) for the infrared part of the spectrum (1700-4500 nm). As signals tend to be small at the time delay of a PIA experiment (usually $\Delta T/T$ is on the order of 10^{-4}), the lock-in technique is used for amplification. For transmission measurements without previous excitation the probe light is optically chopped (Thorlabs MC1000A); for the PIA measurement the pump source is controlled by a standard function generator (Kontron Messtechnik Model 8201). The detector signal is measured by a dual channel lock-in (EG&G Princeton Applied Research Model 5210). In wavelength regions where PL might be expected, the signal after excitation but without probe pulse is measured and subtracted from the PIA signal.

Chapter 4

Terpolymers for Independent Absorption and Transport Optimization

The optimization of photoactive materials for organic solar cells is complicated by the fact that individual modifications concurrently affect several efficiency-limiting factors. For example, in donor-acceptor copolymers, the chemical optimization of the light absorption properties concurrently alters the charge transport properties and not necessarily in the desired direction. This interdependency frustrates step-wise optimization of materials for maximum power conversion efficiency. We therefore introduce a terpolymer with an additional triarylamine unit responsible for charge carrier transport. We find that decoupling of the light absorption and charge transport properties onto separate monomeric units is possible. The co- and terpolymers are then tested in organic solar cell devices, however, it is found that the triarylamine unit is not beneficial for device performance. We demonstrate that the reason for this is the triarylamine acting as a trapping site, thus assisting charge carrier recombination processes.

The main results of this chapter were published in Applied Physics Letters with the title "Controlled energy shuttling in terpolymers enabling independent optimization of absorption and transport properties in organic solar cell materials". Reprinted in part with permission from [87]. Copyright 2012, AIP Publishing LLC.

4.1 Introduction

While P3HT:PCBM had been the benchmark system for bulk heterojunction solar cells for many years, chemists have focused on synthesizing polymers that absorb more of the red part of the solar spectrum in recent years. As shown in figure 4.1 the absorption of P3HT extends only to about 650 nm, collecting at best 27% of the incoming photons,[88] which results in record efficiencies around 5%.[51, 89] Therefore, low-bandgap polymers were developed which have an absorption extending further into the red, such as PTB7.[46]

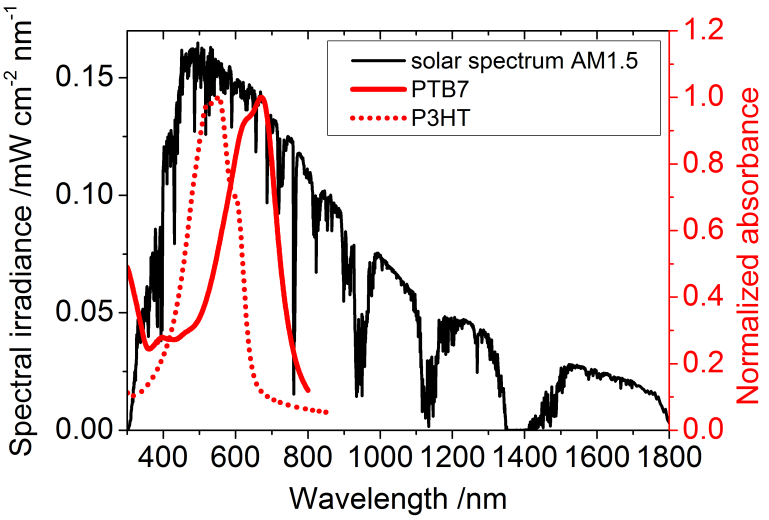

Figure 4.1: Comparison of the solar spectrum and the polymeric absorber materials P3HT and PTB7 (low-bandgap material).

Common strategies to lower the bandgap and design such polymers are quinoid structures and donor-acceptor structures. In quinoid polymers, the π-system consists of aromatic and quinoid rings. In the excited state the quinoid form is aromatized thus making this state more favorable and lowering the bandgap. However, this usually also lowers V_{OC}. An example for this type of low-bandgap polymer is PTB7 which has achieved a power conversion efficiency of 8.4% in optimized devices.[90] Figure 4.2 shows the structure of PTB7 with both aromatic and quinoid form. Donor-acceptor (D-A) polymers have proven to be the more popular approach in the last years.[91] Here, an electron-rich donor moiety and

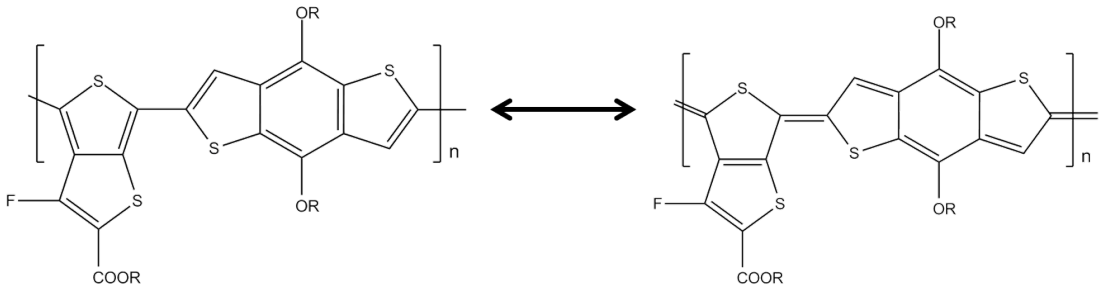

Figure 4.2: Aromatic and quinoid structure of PTB7. R=2-ethylhexyl.

an electron-deficient acceptor moiety are alternatingly connected. Orbital mixing between the donor and acceptor unit decreases the bandgap as shown in figure 4.3.[92] As partial internal charge transfer between the units take place, the double bond character between the units is increased, which leads to a more planarized structure facilitating π-electron delocalization. The outstanding advantage of this approach is that donor and acceptor moiety can be selected and combined in a huge variety of ways, enabling a fine tuning of HOMO (mainly located on the donor moiety) and LUMO (mainly located on the acceptor moiety).[93] Efficiencies over 7% have been achieved with a variety of donor-acceptor polymers in a blend with the acceptor material $PC_{71}BM$.[94–98] It is important to note that here usually the more expensive $PC_{71}BM$ is used instead of $PC_{61}BM$, as it absorbs in the visible range of the solar spectrum and complements the absorption of the D-A polymer.

The external quantum efficiency (EQE) of an organic solar cell, i.e. the ratio of collected electrons in the external circuit to the number of incident photons at a given wavelength, is determined by the product of three factors:

$$EQE\left(\lambda, V, I\right) = \eta_{Abs}\left(\lambda\right) \cdot \eta_{CG}\left(F\right) \cdot \eta_{ext}\left(F, I\right) \tag{4.1}$$

Here $\eta_{Abs}\left(\lambda\right)$ describes the fraction of photons absorbed depending on the wavelength (determined by the absorption spectrum of the photoactive components), $\eta_{CG}\left(F\right)$ is the free charge generation efficiency after photon absorption which can be influenced by an internal field F, and $\eta_{ext}\left(F, I\right)$ is the collection efficiency of the free charge carriers which also depends on the field F and additionally on the illumination intensity I.[99]

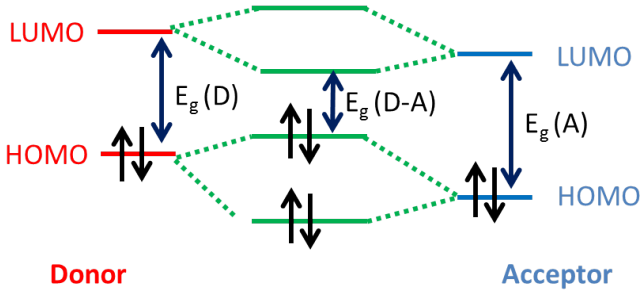

Figure 4.3: Orbital mixing in polymers where donor (D) and acceptor (A) moieties alternate to form a donor-acceptor polymer (D-A). This leads to a decrease in bandgap E_g.

When designing novel donor-acceptor polymers the focus is on maximizing η_{Abs} by extending the absorption into the infrared. However, when the chromophore is changed, not only η_{Abs} changes, but concurrently the charge generation and charge transport properties, thus affecting the charge extraction efficiency η_{ext}.[100] This interdependency complicates systematic material design as separate optimization of η_{Abs} and η_{ext} is not possible. We therefore introduce a terpolymer where the interdependency is broken by using separate parts for absorption and transport. This approach could enable a straightforward and systematic approach for the synthesis of new polymers as changing the chromophore would not affect the transport properties located on a different unit of the terpolymer. Here, we use a donor-acceptor polymer as chromophore and statistically copolymerize it with a triarylamine unit which is responsible for transport. Triarylamine units have often been used in light-emitting copolymers for OLED applications.[101] They are known to be good hole transport materials with a hole mobility on the order of $10^{-3}\,\mathrm{cm^2V^{-1}s^{-1}}$ (measured in OFETs) and they accept holes readily due to their comparably low oxidation potential.[102, 103]

Figure 4.4 illustrates the idea of separating absorption and transport properties: After light absorption and exciton formation on the donor-acceptor unit (panel 1) charges are generated, the electron is transferred to the electron acceptor material PCBM (phenyl-C61-butyric acid methyl ester)(panel 2). Subsequently, the hole is shuttled onto the triarylamine unit (panel 3 and 4).

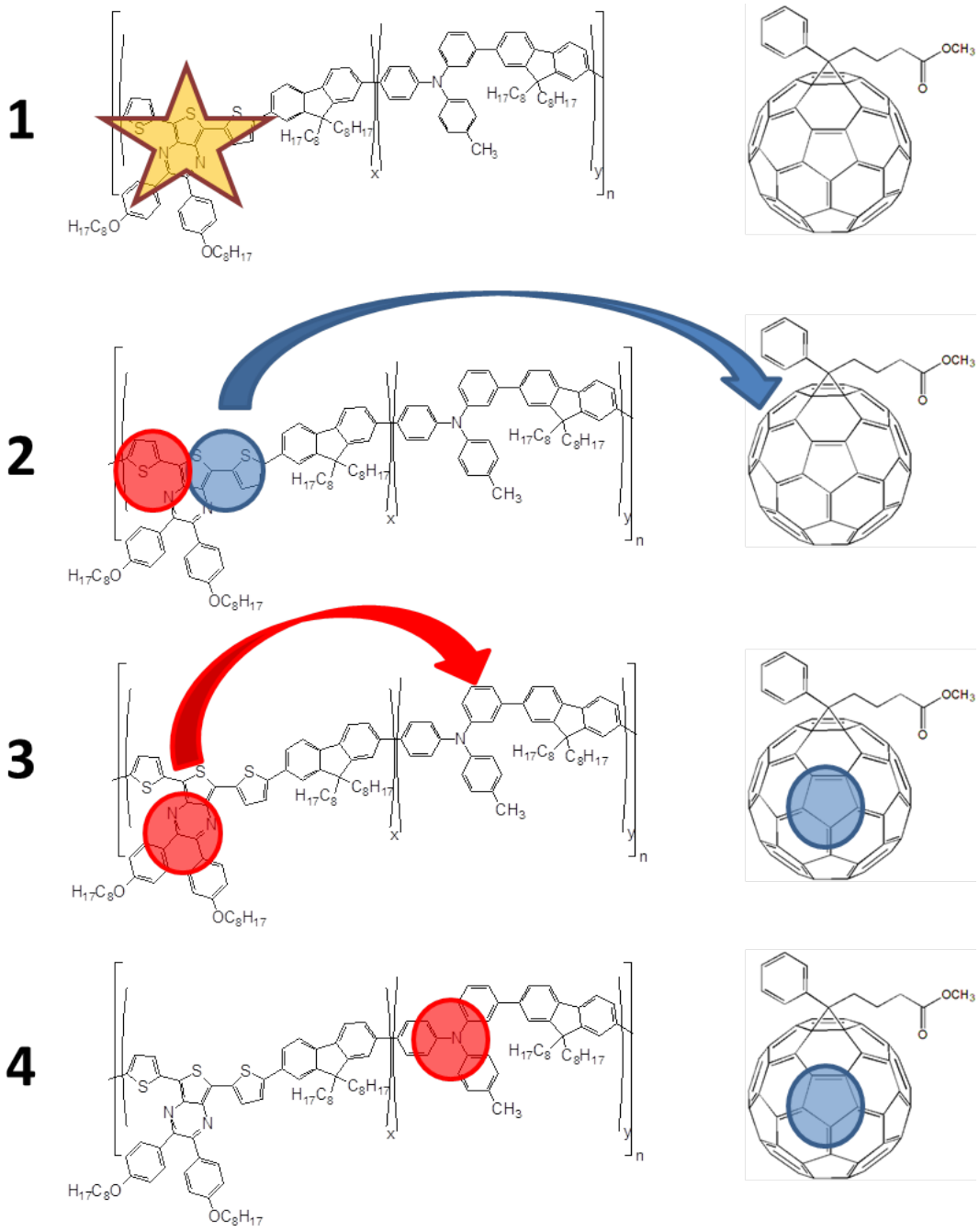

Figure 4.4: Upon absorption of light an exciton is formed on the donor-acceptor unit of the terpolmer (panel 1). Immediately, charges are created and the electron (blue dot) is transferred onto the electron acceptor material PCBM (panel 2). The hole (red dot) is then shuttled onto the triarylamine unit (panel 3 and 4).

4.2 Materials

In order to investigate this concept of separate absorption and transport properties, we examine four polymers. Two polymers have the same donor-acceptor unit respectively, however only one at a time contains the triarylamine transport unit. This concept is visualized in figure 4.5.

4.2.1 Molecular structures

Three of the donor-acceptor polymers, namely MR2/8, MR2/6 and MR3/4, were synthesized in the group of Silvia Janietz at the Fraunhofer Institute for Applied Polymer Research (IAP) in Potsdam. The results for the forth polymer, named APFO-Green 5 (APFO: alternating polyfluorene copolymer), were taken from a publication by Zhang and coworkers.[104] The structures of the polymers are shown in figure 4.5. The synthesis of the MR polymers was done via a Suzuki C-C-cross-coupling reaction with a $Pd(PPh_3)_4$ catalyst. A polymer very similar to MR2/8, with the only difference being the octyloxy side chains in meta and not in para position, was synthesized by Gadisa and coworkers and solar cells based on bulk heterojunctions with PCBM were reported in the literature with an efficiency of 3.5%.[105] The donor-acceptor unit of MR2/8 and MR2/6 is a dithienylquinoxaline, while the donor-acceptor unit of MR3/4 and APFO-Green 5 is a dithienylthienopyrazine. Here the only difference is the exchange of benzene (MR2/6 and MR2/8) for thiophene (MR3/4 and APFO-Green 5) in the condensed ring system which leads to a significant red shift in the absorption of MR3/4 and APFO-Green 5. The additional octyloxy side chains were introduced in both donor-acceptor systems to enable better solubility. The difference between MR2/8 and MR2/6 is the additional triarylamine unit responsible for transport introduced for MR2/6. This unit is also present in MR3/4, but not in APFO-Green 5. The ratio of donor-acceptor structure and triarylamine is 2:1 for both terpolymers, the components are distributed statistically. Table 4.1 summarizes the relative composition of the polymers and their molecular weights M_w and M_n which were determined by gel permeation chromatography (GPC) versus polystyrene (PS).

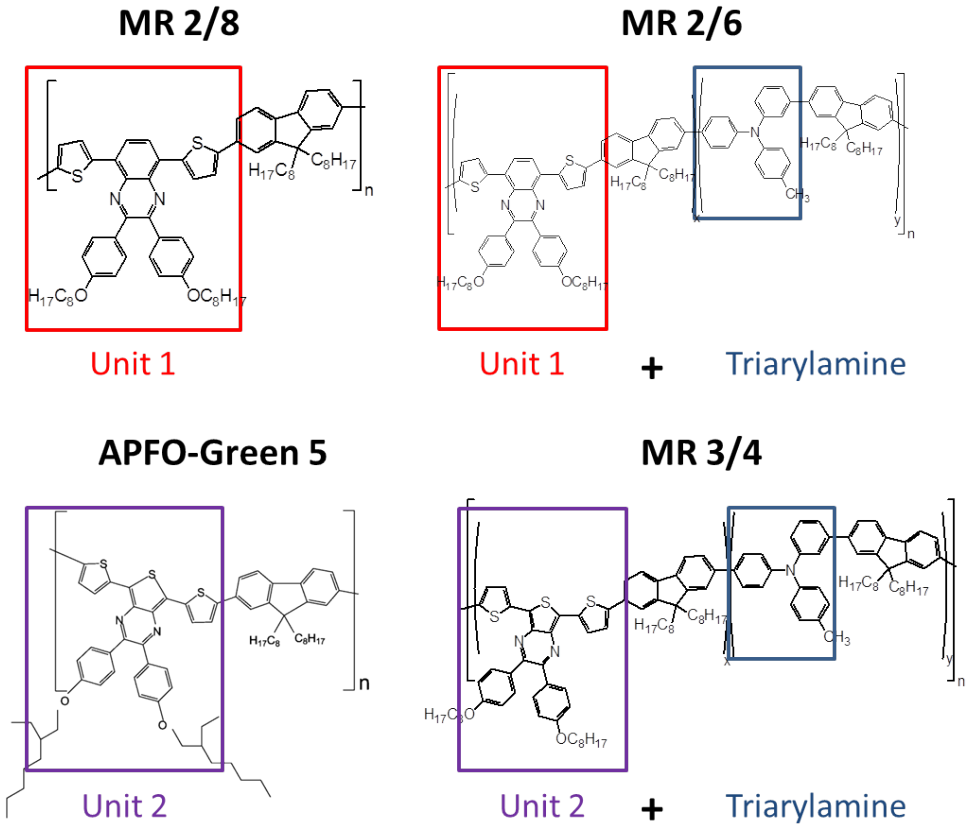

Figure 4.5: Structures of MR polymers and APFO-Green 5. For MR2/6 and MR3/4 x=2/3 and y=1/3.

4.2.2 Mobilities and energy levels

To characterize the polymers further, the hole mobility μ_{FET} was determined in organic field effect transistors; HOMO and LUMO were determined by cyclic voltammetry. These experiments were done at the Fraunhofer IAP, the results are summarized in table 4.2. The field effect mobilities are on the order of $10^{-3}\,\mathrm{cm}^2/\mathrm{Vs}$ for all four polymers. The same order of magnitude was found for field effect mobilities in PCBM.[107] The HOMO and LUMO levels are similar for MR2/6 and MR2/8 and for MR3/4 and APFO-Green 5 respectively, indicating that the inclusion of the triarylamine does not drastically alter the energy levels of the terpolymer. However, in the coming sections we will observe that there

	Fluorene	TAA	D-A unit	Molecular weight /g·mol^{-1}	
				M_w	M_n
MR2/8	1	0	1	22,300	10,400
MR2/6	1	1/3	2/3	38,200	16,800
MR3/4	1	1/3	2/3	91,800	20,500
APFO-Green 5	1	0	1	95,000	40,000

Table 4.1: Relative part of the components of the MR polymers (TAA: triarylamine) and their molecular weights as determined by GPC. The molecular weights of APFO-Green 5 were determined by size exclusion chromatography in trichlorobenzene relative to polystyrene standards and taken from the literature.[104]

	μ_{FET} cm^2/Vs	HOMO eV	LUMO eV
MR2/8	$1.6 \cdot 10^{-3}$	-5.8	-3.1
MR2/6	$2.3 \cdot 10^{-3}$	-5.8	-3.1
MR3/4	$1.1 \cdot 10^{-3}$	-5.6	-3.6
APFO-Green 5	$8 \cdot 10^{-4}$	-5.6	-3.6

Table 4.2: Hole mobilities were determined in OFETs. HOMO and LUMO were determined by cyclic voltammetry. HOMO and LUMO of APFO-Green 5 were reported in [106], its mobility in [104].

are subtle but important differences between the energy landscape of MR2/6 and MR2/8.

4.3 Influence of triarylamine on absorption

Figure 4.6 compares the absorption of the MR polymers and APFO-Green 5 (taken from [104]). The absorbance spectra are normalized to their peak value, which for all polymers is roughly around 400 nm. An additional peak is found further to the red with less extinction than the peak around 400 nm. Addition of

the triarylamine unit influences the shape of the absorbance spectrum, causing a relative decrease of the redder peak, but no additional features. ZINDO calculations (Zerners intermediate neglect of differential overlap) done for the copolymer have shown that the 400 nm region absorption is due to a $\pi - \pi^\star$ type transition involving change in electron density between the thiophene and fluorene subunits, while the redder absorption is due to a charge-transfer absorption involving the thiophene and benzo- or thienopyrazine units.[108]

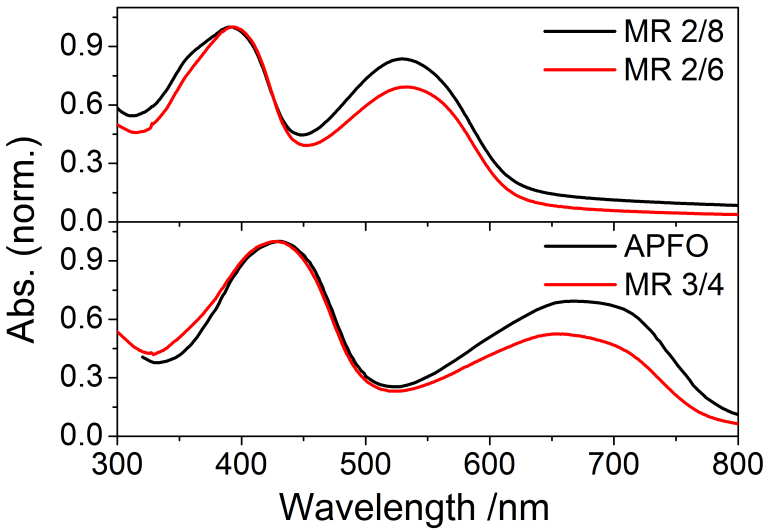

Figure 4.6: Absorption spectra of MR polymers and APFO-Green 5 normalized to the peak value of their absorbance. Polymers without triarylamine in black, with triarylamine in red.

Taking a closer look at the relative difference in peak intensity between the co- and terpolymers we have to take into account the statistic distribution of the respective monomer units. In the copolymers, each fluorene unit is attached to two thiophenes, while in the terpolymer, 2/3 of the fluorenes are attached to two thiophenes with 1/3 of the fluorenes being attached to only one thiophene. Therefore, arguing from the perspective of the Lambert-Beer law and chromophore density, we might approximate that the 400 nm absorption of the terpolymer is roughly 5/6ths that of the copolymer. The ratio of the absorption band stemming from the charge-transfer transition of terpolymer to copolymer should be 2/3, as only

2/3 of the terpolymer contain the D-A unit. Then the expected ratio between the red absorption peaks in the normalized terpolymer to copolymer spectrum is $2/3 \times 6/5 = 0.8$; which is roughly equivalent to the 0.83 and 0.76 ratios for the red peak absorption intensity between MR2/6 and MR2/8, and APFO-Green 5 and MR3/4, respectively.

Therefore, the entirety of the difference between the absorption spectrum of the copolymer and terpolymer can be explained in terms of dilution of the donor-acceptor-donor chromophore, indicating that the triarylamine unit can be incorporated into the polymer structure without influencing the charge-transfer chromophores optical properties.

4.4 Triarylamine as hole acceptor: optical proof of principle

As we have seen in the previous section, the triarylamine unit can be incorporated into the polymer structure without changing the optical properties of the donor-acceptor unit. We now examine whether the triarylamine unit can actually accept the hole from the chromophore after the electron is transferred onto PCBM in a bulk heterojunction morphology. To examine this we use transient absorption spectroscopy on the short time scale (1 ps to 3 ns), the experimental setup was presented in section 3.4.1.

4.4.1 Triarylamine as hole acceptor in MR3/4

A comparison of the transient absorption data of thin films of pristine MR3/4 (see figure 4.7(a)) and MR3/4:PCBM blend (see figure 4.7(b)) shows direct evidence of hole transfer. In pristine MR3/4 we measure the exciton dynamics: ground state bleach, stimulated emission (around 730 nm) and photoinduced absorption decrease simultaneously on a timescale of about 1 ns, after that no signal is left. In contrast, no stimulated emission is found in the MR3/4:PCBM blend; we therefore conclude that exciton quenching by electron transfer onto PCBM occurs within the 150 fs response time of our spectrometer.[109] Up to roughly 30 ps after photoexcitation, a constant positive absorption bleach signal between

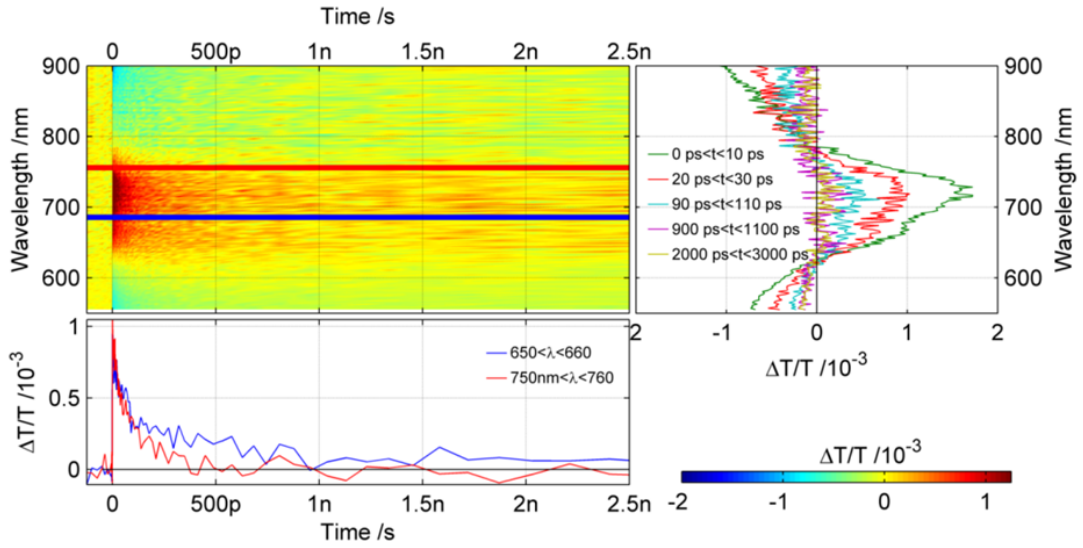

(a) MR3/4 pristine

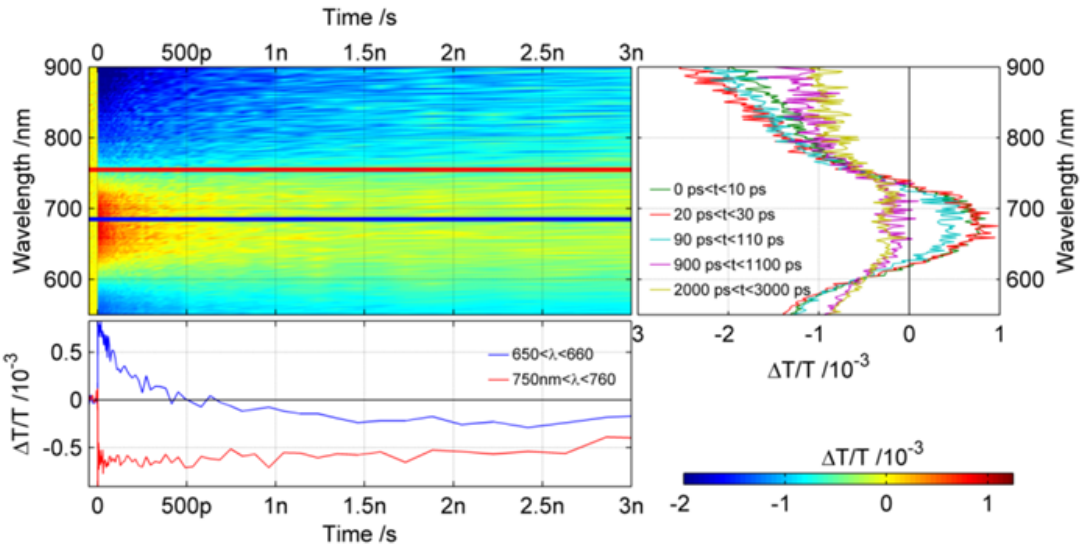

(b) MR3/4:PCBM blend

Figure 4.7: Transient absorption surface of (a) MR3/4 pristine thin film and (b) MR3/4:PCBM 1:2 blend thin film in the short time range up to 2.5 ns after excitation at 650 nm (pristine) and 400 nm (blend) respectively. Spectra at different time delays are shown on the right-hand side of the surface and below kinetic traces at selected wavelength ranges as indicated with blue and red lines in the surface. For pristine MR3/4 we find exciton dynamics, for the blend we find hole transfer from the chromophore unit to the hole transport unit.

600 and 720 nm is found, which indicates that the hole still resides on the chromophoric unit. However, this bleaching signal decreases and within about 500 ps, the bleach is overwhelmed by a photoinduced absorption as shown by the blue line (wavelength region 650-660 nm) in the kinetics plot. At the same time the signal at 750-760 nm remains constant until 1 ns. The presence of this isosbestic point while the absorption bleach decays indicates that the change is due to a transfer between two excited-state species, i.e. the decrease of the bleach cannot be explained by a population decrease due to electron-hole recombination. If excited state recombination is not the reason for the decrease of the absorption bleach to negative values, the only remaining explanation is transfer of the hole from the chromophore to the triarylamine unit. Thus the absorption properties of the chromophore are restored, while the hole still resides on the polymer. These measurements show that our strategy is effective: we introduce a transport unit into the polymer that accepts the hole and does not influence the absorbing unit.

4.4.2 Triarylamine as hole acceptor in MR2/6

Having established that hole transfer from chromophore to hole transport unit takes place in MR3/4:PCBM blends, we now turn to the polymers with dithienylquinoxaline structure as donor-acceptor unit, the copolymer MR2/8 and the terpolymer MR2/6 with a charge transfer absorption at 500-600 nm. Figure 4.8 shows the transient absorption surfaces of the polymer:PCBM blends at short time delays. We note that the absorption bleach only extends up to 600 nm; at longer wavelengths a broad photoinduced absorption is found. This blue shift of the ground state bleach in MR2/6 compared to MR3/4 hinders a direct observation of the bleach being overwhelmed by photoinduced absorption after hole transfer (as observed in the previous section) as the photoinduced absorption of the charged species overlaps much less strongly with the absorption bleach. This means that although holes transfer from the chromophore to the triarylamine in MR2/6, the net transient signal in the ground state absorption bleach region does not become negative. To gain insight into the hole transfer process we compare the kinetics of the ground state bleach (between 550 and 560 nm) of MR2/6 and MR2/8 making the assumption that the cross-section of the charge-induced

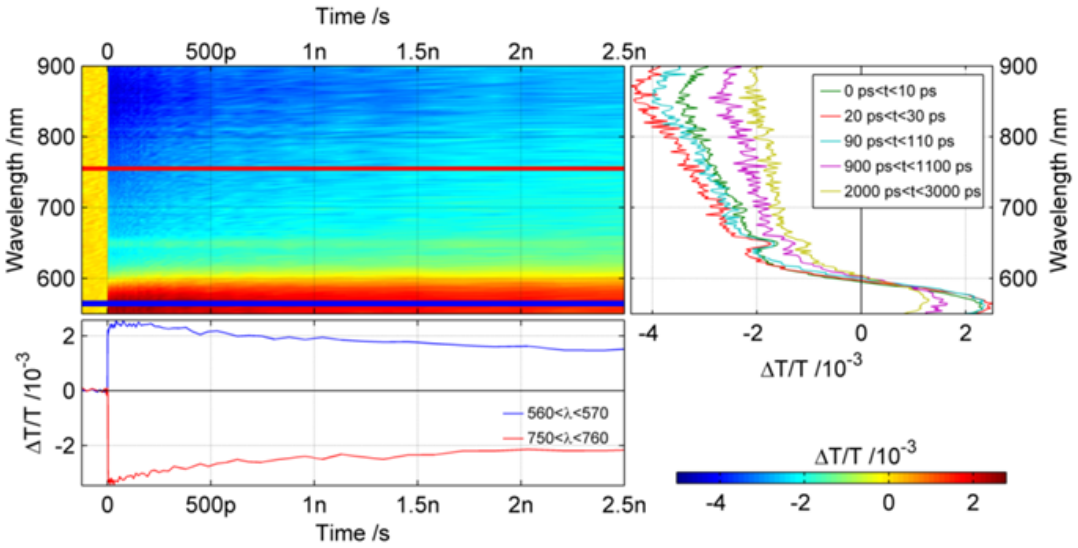

(a) MR2/8:PCBM blend

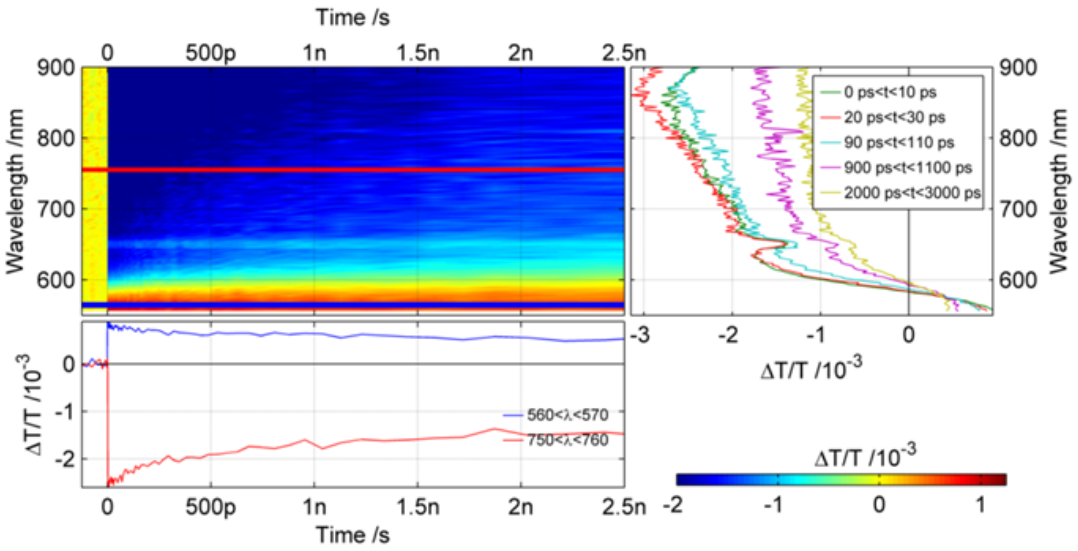

(b) MR2/6:PCBM blend

Figure 4.8: Transient absorption surface of (a) MR2/8:PCBM 1:2 and (b) MR2/6:PCBM 1:2 blend thin films in the short time range up to 2.5 ns after excitation at 510 nm. For both surfaces spectra at different delay times are shown on the right-hand side of the surface and below kinetic traces at selected wavelength ranges.

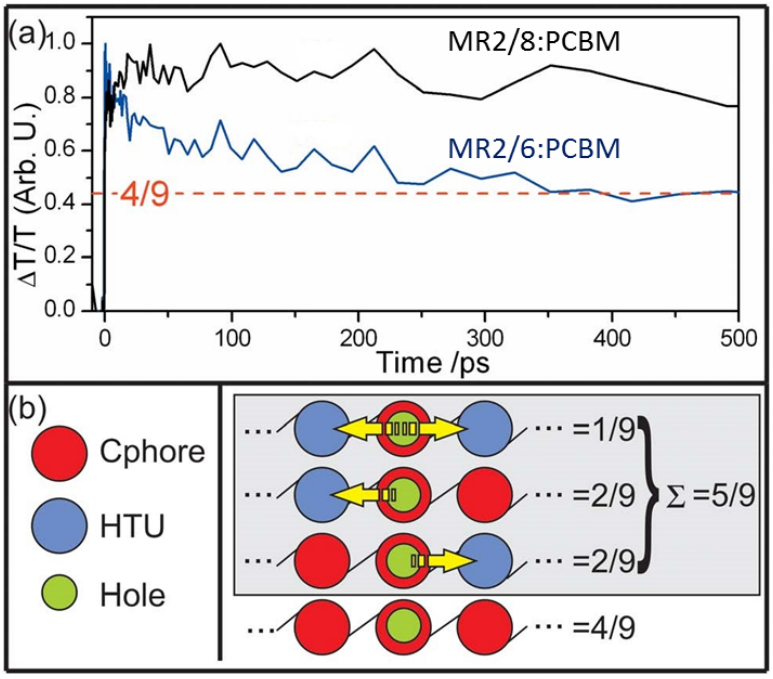

Figure 4.9: Panel (a) compares the kinetics of the ground state bleach (550-560 nm) of MR2/8 and MR 2/6 after excitation at 510 nm. While the bleach stays roughly constant for the copolymer (slight increase and decrease due to spectral diffusion and recombination), it decays by 5/9th in the first 500 ps for the terpolymer as the holes are transferred from the chromophores neighboring a triarylamine unit. Panel (b) illustrates the probability of the excited chromophore (Cphore) having at least one directly adjacent hole transport unit (HTU).

absorption is small in that region for both polymers. Figure 4.9(a) shows the kinetics in the first 500 ps, the time range when we observed the hole transfer in MR3/4. The normalized kinetics of the ground state absorption bleach in MR2/8:PCBM stay roughly constant during that time. At early times, the signal increases slightly, likely due to diffusion of the excited-state species to the lower lying energy states in the inhomogeneously broadened density of states. In contrast, the ground state bleach in MR2/6 decreases significantly during the first 500 ps indicating that holes are being transferred away from the chromophore to the triarylamine unit in the terpolymer. Taking into account that MR2/6 is a sta-

tistical terpolymer with a ratio of 2:1 of chromophore and hole transport unit and making the assumption that the coupling process obeys Bernoullian statistics, we can calculate the probability of a photoinduced-hole-bearing chromophore being directly adjacent to at least one hole transport unit as 5/9. This is illustrated in figure 4.9(b). As the bleach signal of MR2/6 decays by that value in the first 500 ps (as shown in figure 4.9(a)) we conclude that all holes which are created on chromophores neighboring a hole transport unit transfer to the neighboring hole transport unit in that time range. Those holes created on chromophores surrounded by two other chromophoric units have not yet reached a hole transport unit in the first 500 ps, but might do so on the timescale of approximately a nanosecond after a few hops.

4.5 Analysis of solar cell devices

Having established that the general concept of separating the units responsible for absorption and hole transport using a terpolymer design is feasible, as the optical properties of the donor-acceptor unit remain unchanged and the hole transfer to the triarylamine unit takes place on a timescale of 500 ps, we will now investigate whether the concept is beneficial for solar cell performance.

4.5.1 Solar cell performance of optimized devices

After an extensive optimization of the processing conditions and the donor:acceptor ratio, a reproducible procedure to obtain maximum efficiencies for the three MR polymers was determined. The solar cell devices were prepared as described in section 3.1.1. For preparation of the active layer the MR polymer and PCBM were dissolved in chlorobenzene in a 1:2 ratio at a total concentration of 25 mg/ml and stirred overnight at 80 °C. The active layer was spincoated at 1000 rpm resulting in a film thickness of 100 nm. Annealing did not improve the device performance. Figure 4.10 shows the IV curves of the optimized devices, table 4.3 summarizes the characteristic values.

In both MR2/6 and MR3/4, the inclusion of the triarylamine leads to a net decrease in the device efficiency. The decrease in efficiency is significantly smaller

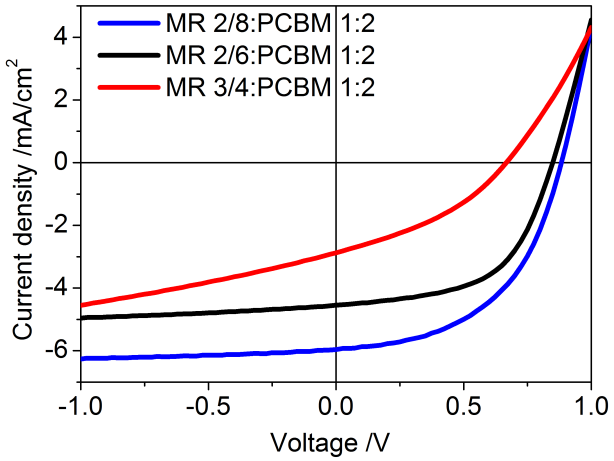

Figure 4.10: IV curves of optimized solar cell devices with co- and terpolymers blended with PCBM and spin coated from chlorobenzene. The corresponding characteristic values are listed in table 4.3.

	Efficiency %	V_{OC} V	I_{SC} mA/cm^2	FF
MR2/8	2.8	0.89	5.3	0.60
MR2/6	2.3	0.84	5.1	0.54
MR3/4	0.7	0.66	3.0	0.36
APFO-Green 5	2.2	0.61	8.2	0.44

Table 4.3: Solar cell performance of co- and terpolymers as donor materials mixed with PCBM in a 1:2 ratio (3:7 for APFO-Green 5). Data for colpolymer APFO-Green 5 are taken from the literature.[104]

from MR2/8 to MR2/6 than from APFO-Green 5 to MR3/4. The decrease in V_{OC} from the polymers with dithienylquinoxaline to the polymers with dithienylthienopyrazine is due to the higher HOMO level of the polymers with red-shifted absorption (see table 4.2). The following sections show that this decrease in efficiency upon incorporation of the triarylamine is not due to morphology or absorption being unfavorable, but that trap-assisted recombination limits the device performance.

4.5.2 Morphology

The morphology of thin films of polymer:PCBM blends prepared identically to the optimized solar cell devices was investigated with atomic force microscopy (AFM). AFM is a surface sensitive technique on the nanometer scale that mechanically probes the surface by scanning it with a sharp tip and measuring the deflection of that tip. Here, the measurement was done in tapping mode with a Dimension 3100 CL. The height images are shown in figure 4.11. The surface roughness is low for all polymers and the intermixing seems to be very high as phase separation on a large scale is not observable. MR2/6 and MR3/4 blends show almost identical surface images, we therefore conclude that the performance differences are not caused by differences in morphology.

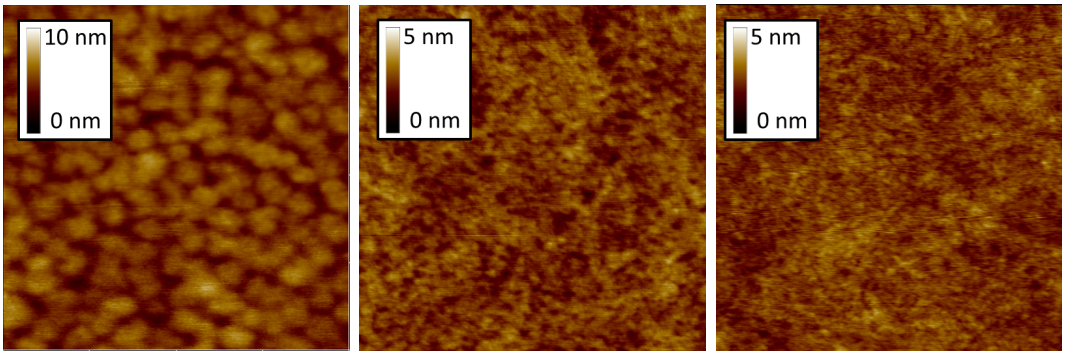

(a) MR2/8:PCBM (b) MR2/6:PCBM (c) MR3/4:PCBM

Figure 4.11: AFM images of (a) MR2/8:PCBM 1:2, (b) MR2/6:PCBM 1:2 and (c) MR3/4:PCBM 1:2 blend thin films. The size of the images is $1 \times 1\,\mu$m.

4.5.3 Internal quantum efficiency

Discrepancies in extinction coefficients between different donor-acceptor units could also explain the performance differences. This possibility can be ruled out by investigating the IQE of the polymer:PCBM blends, which is a measure of the number of electrons generated relative to the number of absorbed photons (see section 3.1.2.2); that means optical properties do not affect the IQE.

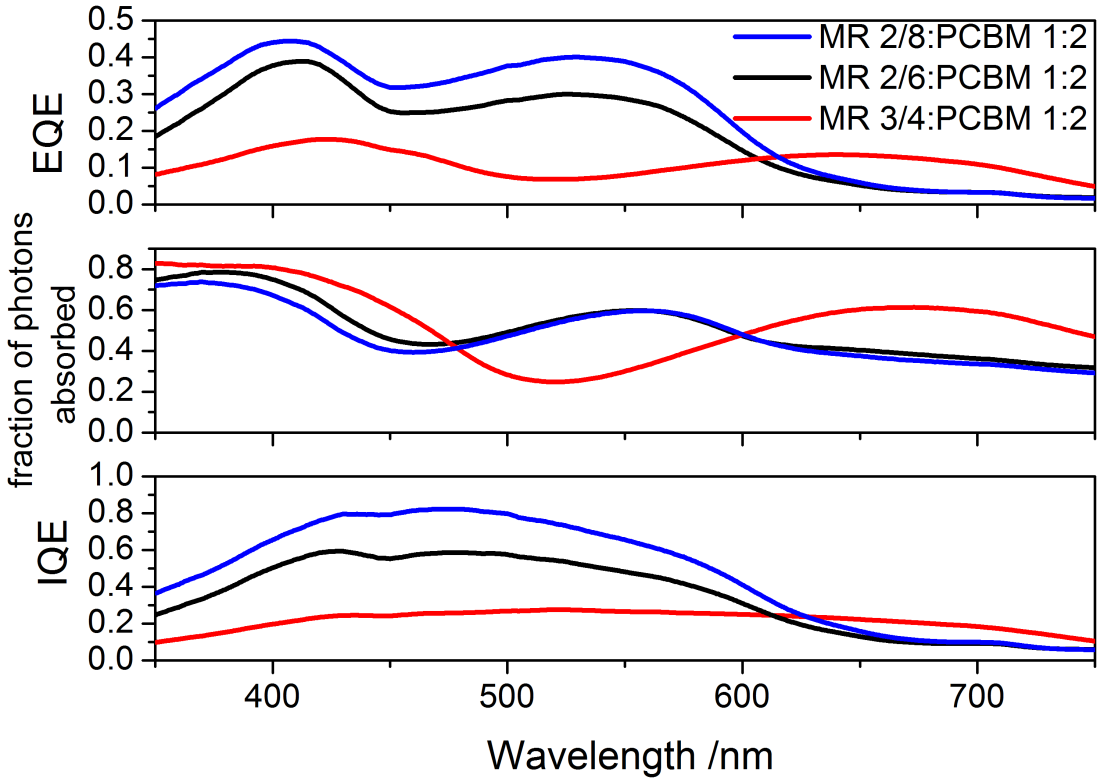

Figure 4.12: The first panel shows the measured external quantum efficiency of the three polymer:PCBM blends in optimized solar cells, the second panel the total number of photons absorbed by the blend (as calculated with a transfer matrix approach). From these data the internal quantum efficiency as shown in the lower panel is calculated. The IQE is distinctly different for the different polymers leading to the conclusion that electronic and not optical processes are responsible for differences in device performance.

EQE, fraction of absorbed photons and IQE are shown in figure 3.3 for all three MR polymer:PCBM blends. The fraction of absorbed photons was calculated with a transfer matrix approach as discussed in section 3.1.2.2.[81] The IQE is flat in the wavelength region from 400 to 600 nm for MR2/6 and MR2/8 and from 400 to 700 nm for MR3/4 indicating that the photons absorbed in that wavelength region have the same probabilities to generate free charge carriers, respectively. However, this plateau is distinctly lower for MR3/4 at about 25%,

i.e. only one quarter of the absorbed photons generate free charge carriers. This ratio is considerably higher for MR2/6 and MR2/8, with an IQE of about 60% and 80% respectively. This analysis ascertains that a low extinction coefficient is not the reason for limited solar cell performance of MR3/4 and MR2/6, but electronic processes of charge generation and recombination distinctly lower the IQE.

4.6 Charge generation and recombination

In order to further elucidate the performance differences of the terpolymers with the triarylamine and the copolymers without, we now investigate charge generation and recombination processes. We use fluence dependent transient absorption measurements on the timescale from 1 ns to 10 μs to study how the charge recombination rate depends on the density of charge carriers. As shown in figure 2.17 on page 33 we can distinguish between free charges and geminate pairs or trapped charges by the excitation intensity dependence of their decay. Recombination of charges that never move outside their Coulomb interaction with one another and recombination that is limited by carrier detrapping occurs at the same rate irrespective of the carrier density while recombination of free charges proceeds more quickly at higher charge densities.[36]

Figure 4.13 shows the normalized photoinduced absorption after excitation at 1, 5 and 10 μJ/cm^2 for the polymer:PCBM blends. For the MR2/8:PCBM blend faster recombination is observed for the higher excitation fluence, indicating the presence of free charges. This is not the case for the MR2/6 and MR3/4 blends, where the normalized decay shows little dependence on excitation fluence, non-geminate recombination of free charges is not the dominant factor here.

As the recombination of geminate pairs is usually observed on shorter timescales than the intensity independent recombination here, we assume that the recombination process is limited by carrier detrapping. A faster detrapping rate in MR2/6:PCBM leads to faster recombination, but also to a higher short circuit current compared to MR3/4:PCBM. This detrapping behavior is investigated further in a pulsed LED experiment as described in section 3.2. Here, the sample is illuminated with square pulses of light for 290 μs at various intensities from 0.1

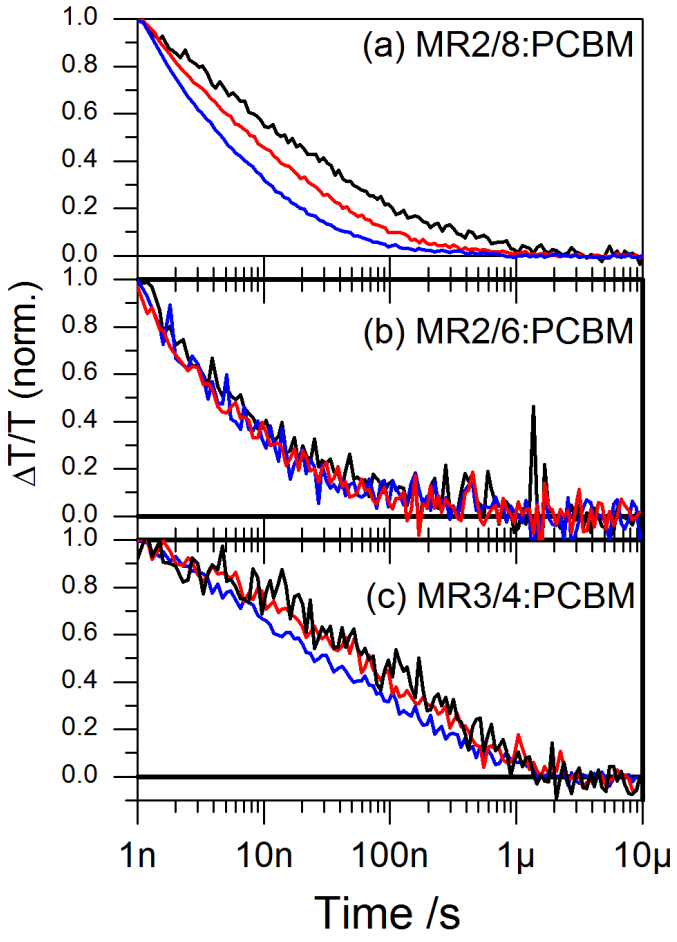

Figure 4.13: Normalized decay of the photoinduced absorption (700-850 nm) after excitation at 532 nm with 1, 5 and 10 μJ/cm^2 for blends of (a) MR2/8, (b) MR2/6 and (c) MR3/4 with PCBM. For MR2/8, the rate of charge recombination is excitation intensity dependent, indicating that free charge carriers were generated. This is not the case for MR2/6 and MR 3/4, indicating that trap-assisted recombination is dominant for the terpolymers.

to 0.7 equivalent suns. This is done in pulsed mode, i.e. the LED is switched on for 290 μs, then off for 710 μs, then switched on again for 290 μs and so on. As shown in figure 4.14(b), the MR3/4 blend shows a peak in current shortly after the illumination is turned on at higher illumination intensities. This is typical of displacement current due to trap filling.[84] After the light is turned off, we

find a 30 μs current tail due to slow detrapping. Both of these features indicate that long-lived trapped states play a significant role in the device characteristics. These features are much less pronounced in MR2/6:PCBM blends, as shown in figure 4.14(a), wherein a smaller displacement current peak and less current after turn-off, that lasts only 5 μs, is observed.

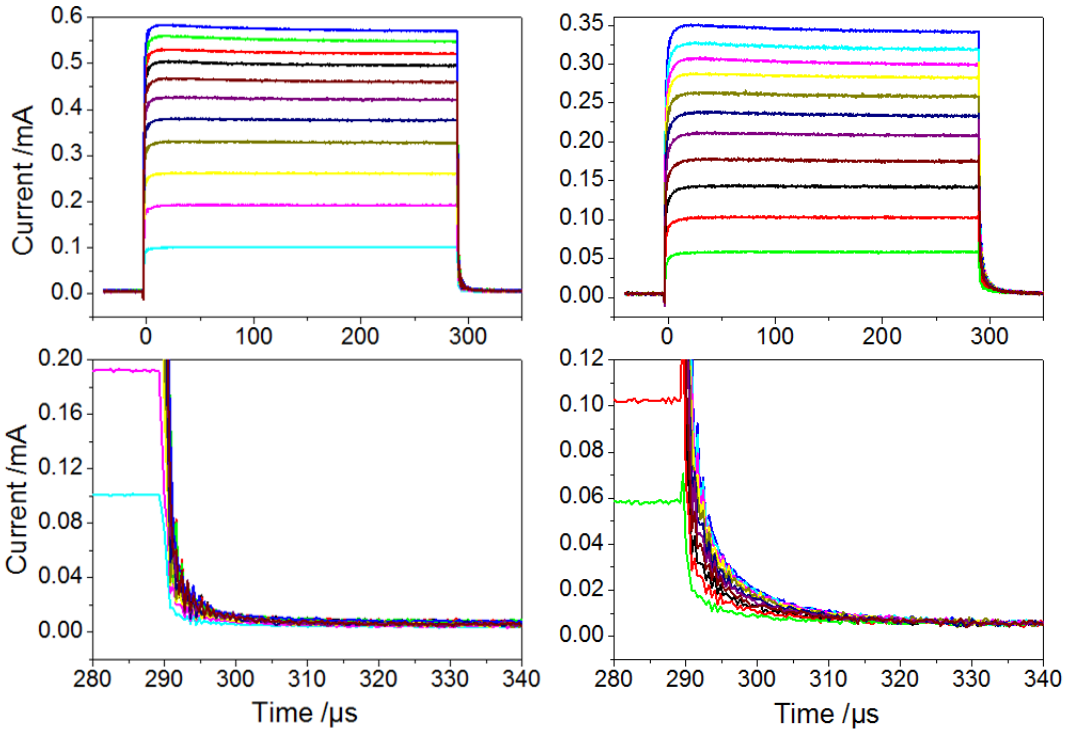

(a) MR2/6:PCBM (b) MR3/4:PCBM

Figure 4.14: Pulsed LED experiment for a) MR2/6:PCBM and b) MR3/4:PCBM, the lower image is an enlargement of the extraction current after switching off the LED. The sample was illuminated for 290 μs with illumination intensities ranging from 0.1 to 0.7 suns.

4.7 Conclusions

In conclusion, we have demonstrated that by using a terpolymer structure, we can separate the optical and transport properties of a polymer onto different monomeric units. After introduction of the triarylamine unit for transport, we found that the absorption of the donor-acceptor unit remained unchanged, and with transient absorption spectroscopy we could show that the hole is indeed transferred from the chromophore onto the triarylamine. In principle, this allows an independent optimization of absorption properties, without affecting transport properties. However, in the statistical terpolymer design we used, we found that the device performance deteriorates after the inclusion of the triarylamine hole transport unit. Using transient absorption spectroscopy and a pulsed LED experiment we showed that trap-assisted recombination limits the device performance. This introduces a clear challenge, indicating that a sufficient network of hole transport units for efficient transport is not achieved with the 1/3 content of triarylamine monomers in the polymer backbones. Increasing the content of hole transport units is a possible solution, however this would further decrease the effective absorption strength of the polymer necessitating thicker active layers and imposing further demands for efficient charge transport. Using hole transporting segments that have a strong tendency to pack would be another way to overcome the problem of trapping within the terpolymer. Thus interchain hole transport would be favored. If longer hole transporting segments were used, i.e. the terpolymer not being statistical but with a certain block length of hole transport units, intrachain hole transport could be improved. Despite this clear challenge of hole trapping, the general approach of independent optimization is promising and provides a valuable route to clearly controlling structure-function relationships in materials for organic electronics. Using terpolymer designs, guiding excited state flow within the polymer backbone is realizable. The control of excited state location that we demonstrated here has significant potential for enhancing the ability to engineer photoactive materials for organic solar cells.

Chapter 5

Charge Generation with Varying Ratio of Amorphous/Crystalline Donor Material

This chapter presents an ultrafast photophysical investigation of charge generation and recombination processes in five samples with varying ratios of semi-crystalline and amorphous PPE-PPV copolymers as donor material in a blend with PCBM. These samples exhibit considerable differences in organic solar cell performance with power conversion efficiencies ranging from 4.0 to 0.4%. Using transient absorption spectroscopy on the short timescale we find that exciton quenching is efficient in all samples. However, geminate recombination on the sub 1 ns timescale is a significant loss mechanism for the samples with higher amorphous content. We then move on to transient absorption experiments on the long timescale and fit the data with a model based on concomitant geminate recombination of CT states and non-geminate recombination of free charge carriers to quantify the recombination dynamics for all samples. We obtain a distinctly higher effective Langevin recombination coefficient for the amorphous samples, indicating that non-geminate recombination is an additional charge carrier loss channel here. Finally, we observe that the total CT state recombination on the short and long timescale follows the quantum efficiencies of the samples. We therefore conclude that CT state recombination is the dominant loss mechanism in all samples and that increasing the amount of amorphous polymer leads to

an increased number of bound charge pairs and a smaller amount of free charge carriers.

5.1 Introduction

The morphology of the active layer of bulk heterojunction solar cells is crucial for the device performance. Morphology optimization needs to be carried out with regard to different length-scales, from phase separation and crystallinity to domain purity and interfacial order (see section 2.2.1.3). In the case of the well-known donor material P3HT it was found that structural ordering, i.e. crystallization, is vital for its performance.[110] Well-ordered phases of both donor and acceptor are known to yield superior charge transport properties.[111, 112] Several methods for aggregating P3HT in solution [113, 114] and post-casting methods, such as thermal annealing [51, 115], mechanical rubbing [116] or slow drying [117], were developed to improve crystallinity and thus device performance. However, the best device performance was found in samples that contain both fibers and less ordered P3HT.[114, 118] This can be explained with an enhanced driving force for exciton dissociation in an amorphous and disordered mixed phase of donor and acceptor material as proposed by Durrant and coworkers.[119, 120] Therefore, an ideal morphology should contain disordered phases for exciton dissociation and ordered phases for charge transport.[40, 121] One possible pathway to achieve both amorphous and crystalline phases is ternary blending, where two different polymers are mixed with PCBM. This has been done, for instance, with a mixture of regioregular and regiorandom P3HT and PCBM, where a slight increase in power conversion efficiency was observed.[122]

In the following we investigate the ternary blending of amorphous and semi-crystalline anthracene-containing poly(p-phenylene-ethynylene)-alt-poly(p-phenylene-vinylene) (PPE-PPV) copolymers (AnE-PVs) with PCBM. The backbone of both donor materials is the same, however, they differ in their side chains, which leads to one of them being semi-crystalline (AnE-PVab) while the other is completely amorphous (AnE-PVba). Different ratios between the semi-crystalline and the amorphous polymer were investigated in terms of their solar cell performance and morphology.[123] This chapter investigates the samples in terms of

their charge generation and recombination properties in order to elucidate the influence of semi-crystalline and amorphous parts on the free charge generation efficiency.

5.2 Materials and organic solar cell devices

This section introduces the materials investigated in the chapter and their absorption and charge transport properties. Also, the solar cell devices with different ratios between the polymers are introduced. The samples presented in this chapter were prepared by Christian Kästner in the group of Harald Hoppe at Illmenau University of Technology and published in [123].

5.2.1 Molecular structures and absorption

The molecular structures of the AnE-PV copolymers are shown in figure 5.1, their synthesis can be found in [124]. Wide-angle scattering experiments have shown that AnE-PVab (figure 5.1(a)) is semi-crystalline while AnE-PVba (figure 5.1(b)) is amorphous.[125] For the bulk heterojunction solar cell PCBM was used as acceptor material (see figure 4.4 for its molecular structure).

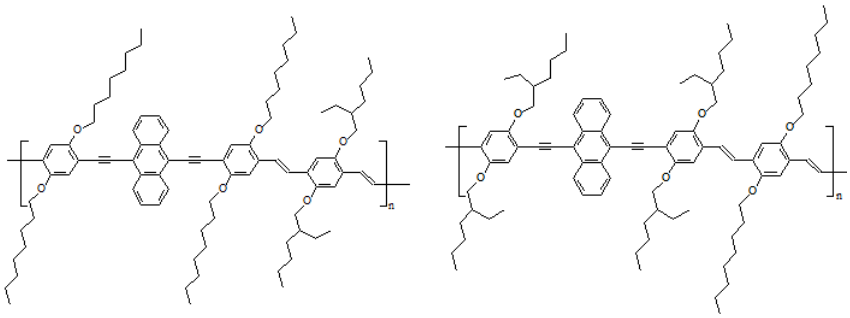

(a) AnE-PVab (b) AnE-PVba

Figure 5.1: Molecular structures of (a) the semi-crystalline AnE-PVab and (b) the amorphous AnE-PVba.

The absorption spectra of AnE-PV:PCBM 2:3 blends are presented in figure 5.2(a). Here, the ratio of AnE-PVab and AnE-PVba was varied in steps of 10 wt%. There is a clear difference between the completely amorphous sample (100% ba) with a broad absorption peak around 520 nm and the semi-crystalline polymer (0% ba) with a red-shifted absorption peak around 550 nm and an additional peak around 580 nm due to $\pi - \pi$ stacking. All ternary blends in between appear to be composites of these absorption spectra according to their relative mixing ratio.

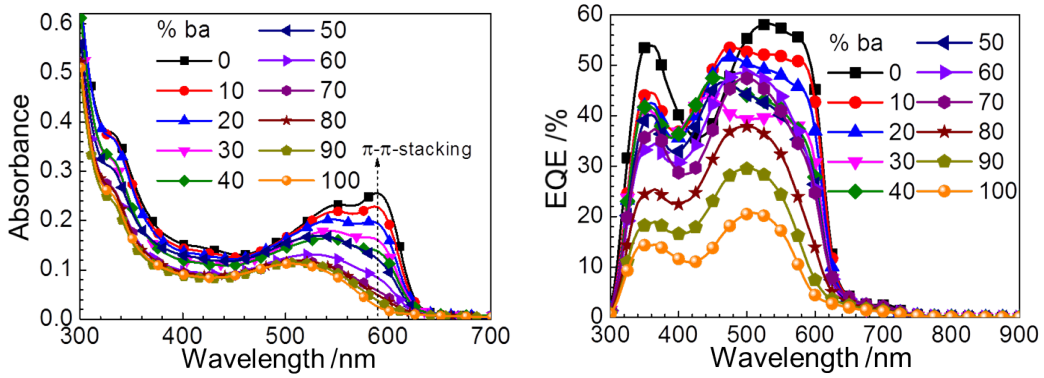

(a) Blend absorbance

(b) EQE

Figure 5.2: Panel (a) shows the absorbance of different ternary AnE-PV:PCBM 2:3 blends, which contain a varying weight percentage of the amorphous AnE-PVba as indicated in the graph. With an increasing content of the semi-crystalline AnE-PVab the absorption is red-shifted and more structured. Panel (b) shows the EQE of the solar cell devices depending on the amount of amorphous AnE-PVba. Adapted from [123] with permission of The Royal Society of Chemistry.

5.2.2 Solar cell performance

Bulk heterojunction solar cell devices are prepared with the AnE-PV:PCBM 2:3 blends with varying AnE-PVab:AnE-PVba ratios. The photovoltaic parameters are shown in figure 5.3 as a function of the amount of amorphous AnE-PVba relative to the semi-crystalline AnE-PVab. Variations are found in all parameters

with a general trend of better performance for the more semi-crystalline samples. The completely amorphous sample shows the lowest characteristic values for all parameters. However, the highest short circuit current and the highest fill factor is found for the sample with 10% amorphous polymer content. Also, the open circuit voltage increases progressively with amorphous polymer content until a maximum is reached for the sample with 50% of both polymers. Variations of an order of magnitude are found in the power conversion efficiency, from 4% for the sample with 10% amorphous polymer, to 0.4% for the sample with only amorphous polymer. Figure 5.2(b) shows the EQE for the solar cell devices. Consistent with the short circuit current of the devices, the EQE is higher with decreasing content of amorphous polymer both in the regions where PCBM (300-400 nm) and the polymers (400-620 nm) absorb. However, with a small amount of amorphous polymer in the mixture the smaller maximum in the EQE spectrum is compensated by an additional contribution in the region where the amorphous polymer absorbs.

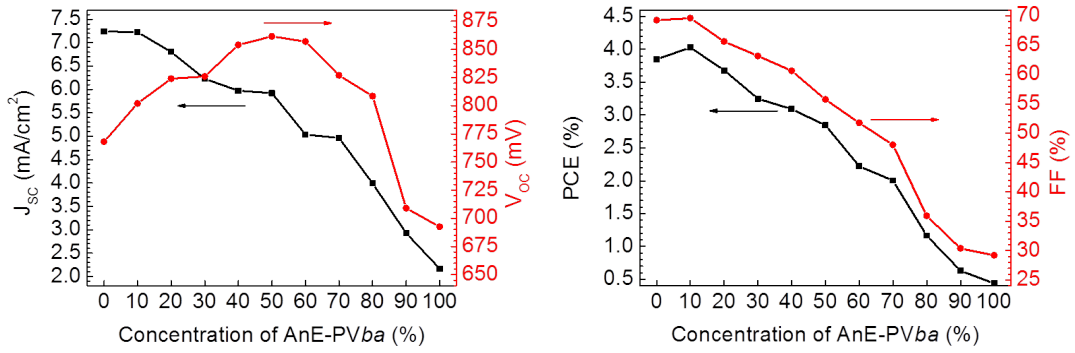

(a) (b)

Figure 5.3: Solar cell performance of blends with different mixing ratios of AnE-PVab and AnE-PVba. The total AnE-PV:PCBM ratio is 2:3. Panel (a) shows J_{SC} and V_{OC}, panel (b) the efficiency and the fill factor versus increasing content of the amorphous AnE-PVba. Reproduced from [123] with permission of The Royal Society of Chemistry.

In the following section we will investigate the reasons for these major dif-

ferences in solar cell performance. We do this using transient absorption spectroscopy on the short and long timescale. We investigate five different samples, with a ratio of semi-crystalline:amorphous polymer of 100:0 (Sample 1), 90:10 (Sample 2), 50:50 (Sample 3), 10:90 (Sample 4), and 0:100 (Sample 5). Their figures of merit are summarized in table 5.1. The samples investigated in the TA experiment are prepared in the same way as the solar cell blends, but consist only of the photoactive blend layer on a quartz glass substrate.

Material	**sample name**	η [%]	V_{OC} [V]	J_{SC} [mA/cm^2]	**FF**
only AnE-PVab	S1	3.9	0.77	7.2	0.69
90% AnE-PVab, 10% AnE-PVba	S2	4.0	0.80	7.2	0.70
50% AnE-PVab, 50% AnE-PVba	S3	2.8	0.87	5.7	0.55
10% AnE-PVab, 90% AnE-PVba	S4	0.6	0.65	3.0	0.30
only AnE-PVba	S5	0.4	0.61	2.2	0.29

Table 5.1: Organic solar cell performance for samples S1 to S5 containing different ratios of AnE-PVab and AnE-PVba. The total AnE-PV:PCBM ratio is 2:3 for all samples.

5.2.3 Morphology

Figure 5.4 shows the AFM tapping mode topography images of the five samples investigated in the TA experiment (AnE-PV:PCBM blends). It is clearly evident that the phase separation decreases upon increasing content of the amorphous polymer. While Sample 1 and Sample 2 exhibit a rough topography indicating pronounced phase separation of polymer and PCBM, Sample 4 and Sample 5 exhibit a smooth surface indicating strong intermixing of the components. The AFM image of Sample 3, with 50% of both polymers, shows an intermediate morphology with distinct phase separation but small domains.

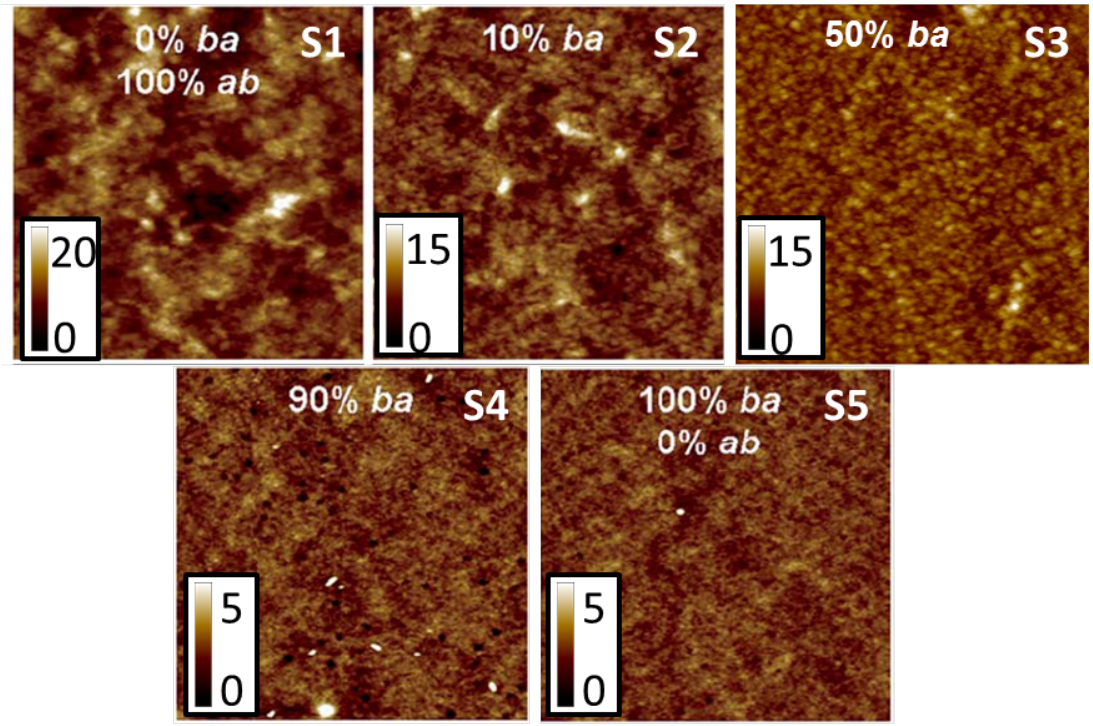

Figure 5.4: AFM topography images of AnE-PV:PCBM blends with varying ratio of AnE-PVab and AnE-PVba. The size of the images is $2.5 \times 2.5 \mu m$. The unit of the scale bar is nanometers. Adapted from [123] with permission of The Royal Society of Chemistry.

5.3 Sub-nanosecond charge generation and recombination

In order to compare the exciton quenching efficiency and early CT state recombination in the different samples, we carried out transient absorption experiments on the short timescale (1 ps to 4 ns). We excited the sample with an excitation wavelength of 400 nm, in a wavelength region where the absorbance of all samples is similar. Both polymer and PCBM absorb in that wavelength region. The obtained transient absorption spectra at different time delays are shown in figure 5.5.

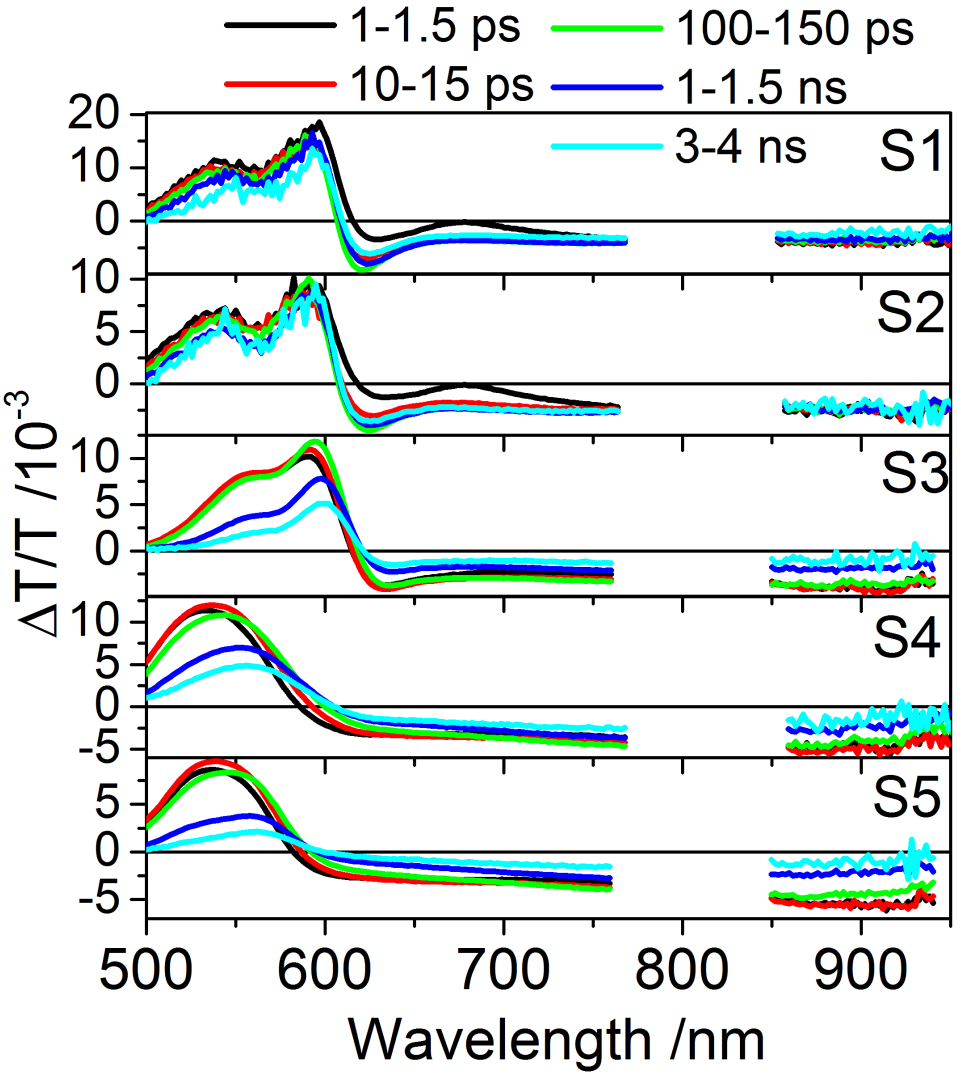

Figure 5.5: Evolution of the transient absorption spectra for all 5 samples (excitation wavelength 400 nm). The data around 800 nm is not shown as it is overlaid by the second order reflection of the excitation pulse. Sample 1 and 2 exhibit stimulated emission in the first few picoseconds and very little decay in the time-range of the experiment. This is different for Sample 3, 4 and 5 where both decay and red-shift of the absorption bleach are observed.

Exciton quenching. Sample 1 and Sample 2, with 0 and 10% content of amorphous polymer respectively, exhibit a distinct peak due to stimulated emission around 680 nm. It is also slightly apparent in Sample 3, but not in the samples with mainly amorphous polymer content. However, the stimulated emission disappears quickly, after about 10 ps it is gone in all cases. We therefore conclude that exciton quenching in all blends is efficient as all excitons are quenched in less than 1 ps for the mainly amorphous samples and less than 10 ps for the more crystalline samples. The stimulated emission observed for Sample 1 and Sample 2 is in agreement with the morphology shown in the previous section. The domain phases are found to be larger in the samples with a higher semi-crystalline polymer content, therefore it takes longer for the excitons to diffuse to the interface where they are quenched. Increasing the content of amorphous polymer decreases the domain size, therefore exciton quenching takes place on the sub-picosecond timescale which we cannot resolve in our experiment.

Red-shift of ground-state bleach. Taking a closer look at the spectral shape of the ground-state bleach of the different samples in figure 5.5, we observe a significant red-shift for the samples with $\geq$ 50% amorphous polymer content (Sample 3, 4 and 5). It is most evident for Sample 5 with only amorphous AnE-PVba in the blend. Here, the GSB maximum red-shifts from 530 nm to 560 nm in the first 3 ns, which is equal to a shift by 125 meV. This relaxation of the ground-state bleach is caused by hole polarons on the polymer that shift to lower and lower energy sites. It indicates that there is a large energetic disorder. Charge carriers are initially created in higher energy levels and subsequently relax to states of lower energy within the DOS. We therefore conclude that the energetic disorder is considerably higher in the samples with $\geq$ 50% amorphous polymer content and we will investigate in the following whether this is beneficial for charge carrier separation.

Sub-nanosecond CT state recombination. Investigating the loss in signal height in Sample 1 and Sample 2 over the whole time-range, we find that both the ground-state bleach between 500 and 600 nm and the broad photoinduced absorption between 650 and 950 nm show very little decay in the time-range up to

3 ns. This means that almost no excited-state population is lost on that timescale in these samples. This is different for Sample 3, 4 and 5, where we find a considerable decay of both ground-state bleach and photoinduced absorption. Figure 5.6(a) shows a comparison of the decay dynamics of the PIA signal between 875 and 925 nm measured at similar excitation intensities for all five samples. The data is normalized to 10 ps when exciton quenching is complete in all samples. The amount of signal left after 2 ns directly correlates to the external quantum efficiencies (see figure 5.2(b)). For the samples with the highest quantum efficiencies (55-60%), Sample 1 and 2, about 90% of the PIA signal is left. For Sample 3 with a medium quantum efficiency (~45%), the PIA signal decays to about 70%. For Sample 4 and 5, with the lowest quantum efficiencies at 28 and 20%, about 50% and 30% of the PIA signal is left respectively.

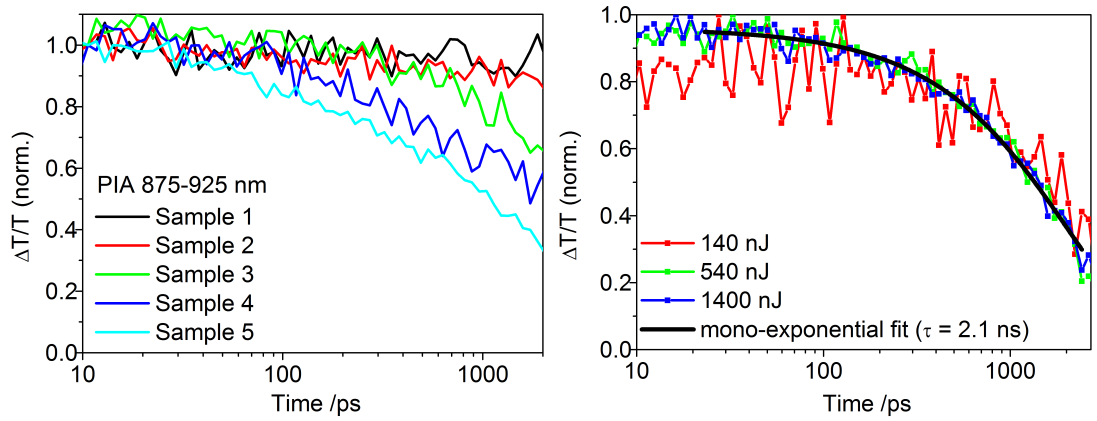

(a) Kinetics PIA

(b) Kinetics GSB Sample 5

Figure 5.6: Panel (a) shows the evolution of the PIA signal (875-925 nm) for all five samples in the first 2 ns. The differences in signal loss on that timescale correlate with the quantum efficiencies of the solar cell devices. Panel (b) shows the evolution of the ground-state bleach signal for Sample 5 after excitation at 400 nm. The evolution of the maximum of the GSB signal is plotted here to track only the decay process without an influence of spectral relaxation. The data at different excitation intensities is shown in colored dots. A mono-exponential decay function is fitted to the data and shown with a black line.

In order to learn about the charge carrier density dependence of the signal

loss on the early timescale, we conducted transient absorption experiments at different excitation intensities. Figure 5.6(b) shows the intensity dependence of the ground-state bleach decay for Sample 5. Here, we track the maximum of the GSB signal and not a given wavelength region, as the maximum red-shifts with time due to spectral relaxation. We find that the signal decay is not dependent on excitation intensity. This points to a geminate recombination mechanism of charge carriers. Excitons are efficiently quenched at the interface, however, a significant fraction of the resulting charge-transfer states are not split into free charges, but are still coulombically bound at the interface and cannot escape their mutual attraction. They recombine geminately on the sub-nanosecond timescale. A mono-exponential fit to the sub 3 ns decay of the GSB reveals a decay rate of $k = 4.8 \cdot 10^8 \mathrm{s}^{-1}$, corresponding to a lifetime of 2.1 ns. This decay rate and thus the interfacial CT state lifetime is very similar to decay rates observed in regiorandom or as-cast regioregular P3HT:PCBM blends,[36, 126] and PCDTBT:PCBM blends [109], indicating that CT state recombination on that timescale is not unusual in polymer blends with a high content of amorphous polymer.

However, even though this early charge carrier loss due to interfacial CT state recombination explains a large amount of quantum efficiency loss, we expect further charge carrier recombination at later times, as the quantum efficiency is still lower than the signal loss due to geminate recombination on the early timescale. Therefore, we will investigate further loss processes on the longer timescale in the next section.

5.4 Charge recombination on the ns-ms timescale

Transient absorption experiments on the ns-ms timescale were carried out in order to investigate further loss processes on the longer timescale and further elucidate the differences between the semi-crystalline and amorphous samples. Figure 5.7 presents the transient absorption spectra obtained at different time delays after excitation at 532 nm. All samples exhibit a ground-state absorption bleach in the wavelength region up to 620 nm, and a broad photoinduced absorption extending into the near infrared. Comparing the spectra at 1-2 ns and 10-20 ns we find for all samples a huge loss in signal, somewhat surprisingly it is even more evident

for the samples with better solar cell performance (Sample 1, 2 and 3). In the following we will take a closer look at the kinetics of the photoinduced absorption signal, in order to analyze the recombination dynamics more quantitatively.

Figure 5.8 shows the kinetics in the photoinduced absorption region between 700 and 900 nm for all samples. Different excitation intensities ranging from 4.5 to 80 μJ/cm^2 were used. All samples exhibit intensity-dependent decay kinetics indicating that non-geminate recombination occurs on the nanosecond to microsecond timescale. The solid black lines present fits to a model for charge recombination that was developed by Howard and coworkers [36] and will be introduced in the following. The model assumes that after 1 ns, the time resolution of the experiment, the charge carrier population is split into two pools: interfacial charge-transfer states and free charge carriers (see section 2.2.1.2). The CT states recombine geminately to the ground state (GS) while the spatially separated (free) charge carriers (SCC) recombine non-geminately. There is no interconversion between the two pools. The following rate equations describe the population dynamics in the system:

$$\frac{\mathrm{d}}{\mathrm{d}t}CT = -k_{CT\rightarrow GS}CT \tag{5.1}$$

$$\frac{\mathrm{d}}{\mathrm{d}t}SSC = -\gamma SSC^{\lambda+1} \tag{5.2}$$

$$\frac{\mathrm{d}}{\mathrm{d}t}GS = k_{CT\rightarrow GS}CT + \gamma SSC^{\lambda+1} \tag{5.3}$$

Here, $k_{CT\rightarrow GS}$ is the monomolecular decay rate, γ is the non-geminate recombination rate, and $(\lambda+1)$ is the recombination order. The ground state is repopulated via two decay channels, either from the geminate recombination of interfacial CT states or the non-geminate recombination of free charge carriers. Solving the differential equations yields the evolution of the GS population as

$$GS(t) = N_0(1-f)(1-[exp(-k_{CT\rightarrow GS}t)]) + N_0 f - (\lambda\gamma t + (fN_0)^{-\lambda})^{-1/\lambda} \tag{5.4}$$

where N_0 is the initial excited state density and f the fraction of non-geminate recombination. We use the solution of the rate equations to globally fit the recombination dynamics for all five samples. We assume that the charge-density is uniform across the film and that the free charge carriers and the charge-transfer

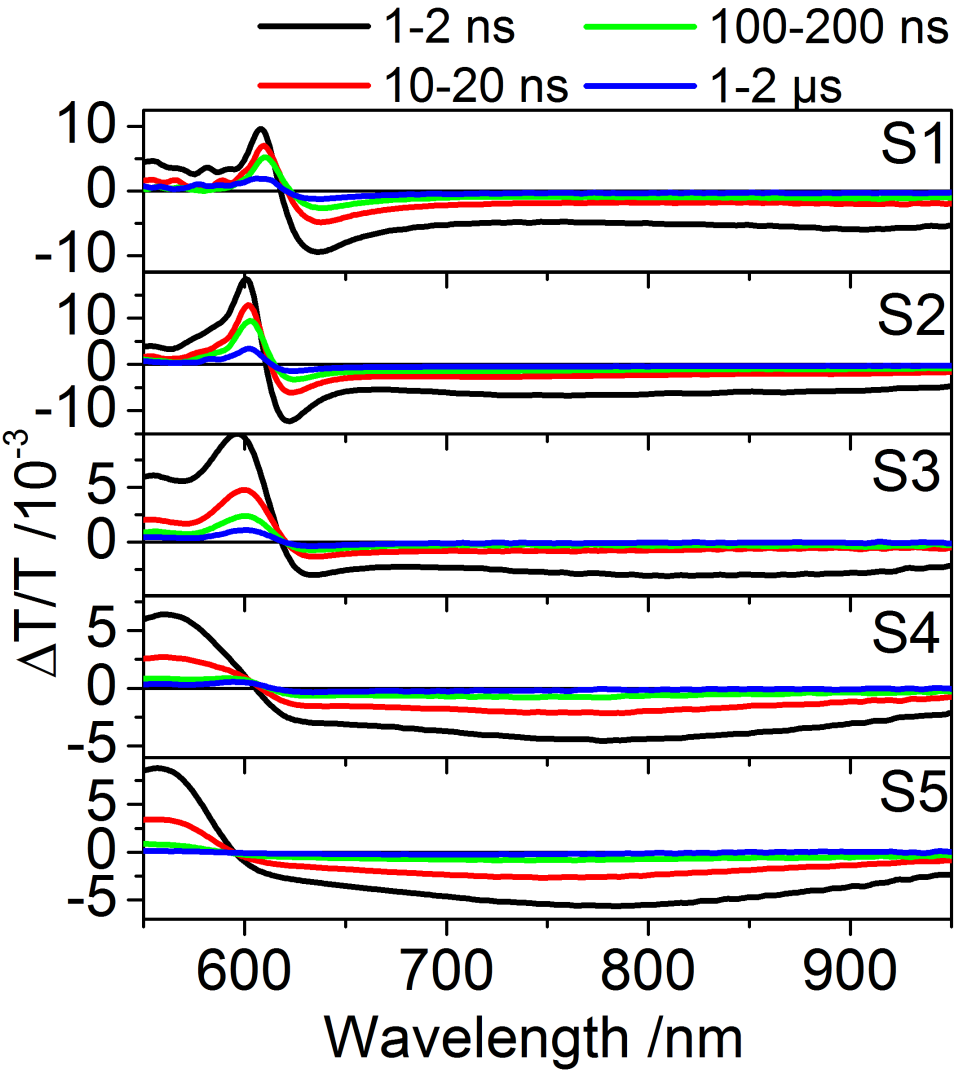

Figure 5.7: Evolution of the transient absorption spectra for all 5 samples (excitation wavelength 532 nm, excitation intensity 22 μJ/cm^2) at time delays specified in the graph. All samples exhibit significant signal loss in the first 20 ns.

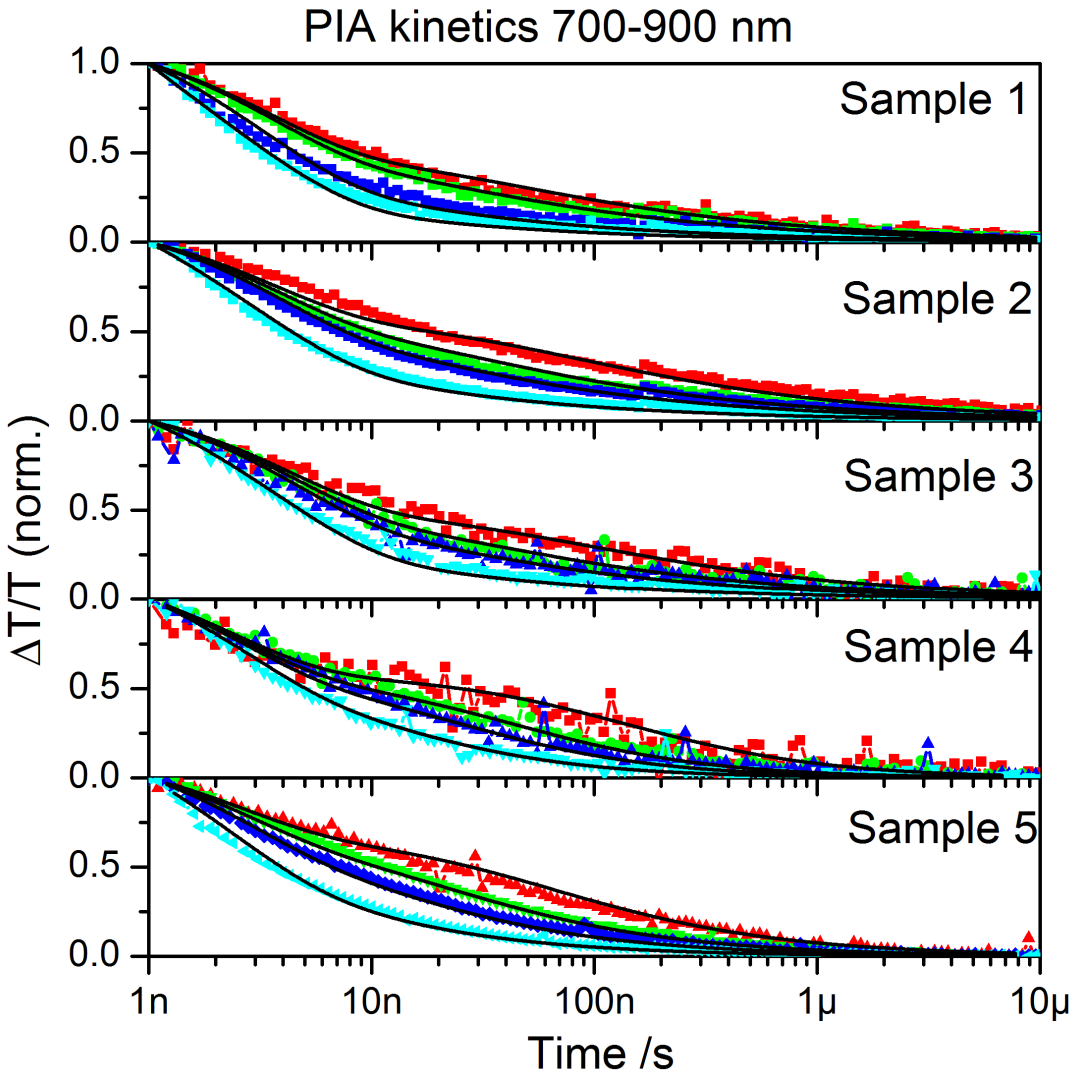

Figure 5.8: Normalized decay dynamics (ns-ms time-range) of the charge-induced absorption between 700 and 900 nm for pump fluences ranging from 4.5 to 80 μJ/cm^2. The data is shown with colored dots. At higher fluences the decay is faster due to accelerated non-geminate recombination of free charge carriers. The solid lines represent fits to our analytical model of charge recombination.

states have equal absorption cross-sections. Except for the initial excitation density (i.e. N_0), all parameters are shared among the different intensities for each sample. As we can see in figure 5.8 the data is well represented by the fit. Table 5.2 presents the parameters along with their standard deviation as extracted from the global fit. For better comparison, the effective Langevin recombination coefficient (the γ where $\lambda + 1 = 2$) at a charge carrier density roughly corresponding to an illumination with one sun ($n = 5 \cdot 10^{15} cm^{-3}$) is calculated. Solving $\gamma_{eff} \cdot n^2 = \gamma_{fit} \cdot n^{\lambda+1}$ for γ_{eff} we obtain $\gamma_{eff} = \gamma_{fit} \cdot n^{\lambda-1}$ and the effective solar cell recombination coefficients presented in table 5.2.

Parameter	**Sample 1**	**Sample 2**	**Sample 3**	**Sample 4**	**Sample 5**
f	0.59±0.01	0.57±0.01	0.51±0.01	0.58±0.01	0.68±0.01
$\gamma/(cm^3)^{\lambda}s^{-1}$	$(1.6 \pm 1.5) \cdot 10^{-32}$	$(7 \pm 5) \cdot 10^{-31}$	$(5 \pm 3) \cdot 10^{-27}$	$(2.8 \pm 1.8) \cdot 10^{-12}$	$(1.5 \pm 0.4) \cdot 10^{-17}$
$\lambda + 1$	3.20 ± 0.01	3.10 ± 0.01	2.99 ± 0.02	2.08 ± 0.02	2.39 ± 0.01
k/s^{-1}	$(1.9 \pm 0.1) \cdot 10^8$	$(1.7 \pm 0.1) \cdot 10^8$	$(2.4 \pm 0.1) \cdot 10^8$	$(4.3 \pm 0.3) \cdot 10^8$	$(4.2 \pm 0.2) \cdot 10^8$
γ_{eff}/cm^3s^{-1}	$1.1 \cdot 10^{-13}$	$1.4 \cdot 10^{-13}$	$1.8 \cdot 10^{-11}$	$5.0 \cdot 10^{-11}$	$2.0 \cdot 10^{-11}$

Table 5.2: Parameters along with standard deviation extracted from a global fit of the model described above to the photoinduced absorption kinetics (700-900 nm) in the long delay measurement. For the quality of the fit see figure 5.8. The parameters were shared for all excitation intensities for each sample. f is the fraction of non-geminate recombination, γ is the non-geminate decay constant, λ+1 is the order of non-geminate decay, k is the geminate recombination rate, and γ_{eff} is the effective (λ+1 = 2) bimolecular decay constant at a charge density of $5 \cdot 10^{15}$ cm^{-3}.

We want to begin with discussing the parameters extracted for the least efficient sample, Sample 5 with only amorphous polymer content. The fraction of non-geminate recombination is highest for that sample at approximately $f = 2/3$. This is due to the fast CT state decay found on the sub-nanosecond timescale, leading to the situation that most of the interfacial CT states have already decayed within the instrument response time of the long time experiment here. Moreover, in solar cell devices, non-geminate recombination is expected to reduce the photocurrent further as the effective Langevin recombination coefficient is relatively high at $2.0 \cdot 10^{-11}$ cm^{3}s^{-1} (compare with as-cast P3HT:PCBM

$1.5 \cdot 10^{-12}\,\mathrm{cm^3 s^{-1}}$ [36]). This is in agreement with the low fill factor (around 0.3) found for the amorphous samples. It is unlikely that sub-nanosecond recombining CT states are split by the internal field, so we hypothesize that the field dependence of the photocurrent is caused by the competition between extraction and non-geminate recombination.

Turning to the samples with higher crystalline content, we find that the fraction of geminate recombination is higher in these samples. However, we found almost no signal decay on the short timescale, therefore we conclude that CT states (or geminate pairs) are longer-lived than in the amorphous samples. This is confirmed by a lower rate of geminate recombination, at about $1.7 \cdot 10^8\,\mathrm{s^{-1}}$, i.e. an inverse rate of 6 ns. The effective Langevin recombination coefficient is about two orders of magnitude smaller at around $1 \cdot 10^{-13}\,\mathrm{cm^3 s^{-1}}$ than in the amorphous samples, pointing to a more efficient extraction of the free charge carriers in a solar cell device. This is in agreement with the high fill factors (around 0.7) which show that the free carriers are swept out efficiently at most internal fields. A similar value for the effective Langevin recombination coefficient was found for annealed P3HT:PCBM films with γ=$2.2 \cdot 10^{-13}\,\mathrm{cm^3 s^{-1}}$, one order of magnitude smaller than for as-cast P3HT:PCBM.[36] The smaller effective Langevin recombination coefficients in the semi-crystalline samples can be explained by the additional thermodynamic driving force created by the polymer crystallinity that aids the separation of charge carriers and their transport from the interface towards the bulk. In the more amorphous samples the higher disorder reduces the energetic difference between the interface and the bulk, therefore charge carriers approach the interface more easily and recombine.[127]

From this analysis of the long-delay data we conclude that more free charge carriers are left in the samples with more amorphous content, however, their extraction is severely limited by the high Langevin recombination coefficient. In the samples with mainly semi-crystalline polymer, charge-transfer states are found to decay on the intermediate 3-10 ns timescale, leading to a greater signal loss compared to the amorphous samples on that timescale. However, the free charge carriers can be extracted efficiently due to their smaller recombination coefficient.

5.5 Unification of short and long timescale charge recombination

Having established that geminate recombination is an important charge carrier loss mechanism on the short and long timescale, we now want to unify the losses on both timescales and compare them with the quantum efficiencies of the different samples. As a rough estimate, we determine the charge carrier loss on the sub 1 ns timescale from the amount of $\Delta T/T$ signal left after 1 ns in the PIA kinetics of the short delay measurement (see figure 5.6(a)). The geminate charge pairs that recombine on the early timescale are too strongly-bound to be extracted into an external circuit in an organic solar cell device. The obtained value accounts for the total amount of charge carriers (both bound and free) left after 1 ns. We then multiply this value with f, the fraction of non-geminate recombination, to get the total fraction of free charge carriers. The obtained number is a measure of the amount of excitons that form free charge carriers that can be extracted. The other excitons form CT states (or geminate pairs) that decay geminately and do not contribute to the photocurrent. Table 5.3 summarizes the obtained values and compares them with the maximum EQE value for all samples. To simplify the comparison, the values are also shown in figure 5.9. The EQE values clearly follow the fraction of free charge carriers for all samples. We therefore conclude that CT state recombination is the dominant quantum efficiency loss mechanism in these samples. The amount of CT state recombination changes with the mixing ratio of the two polymers, and clearly increases with increasing amorphous polymer content. However, as the fraction of free charge carriers is distinctly higher than the EQE values for Sample 4 and 5, and along with these samples having a significantly lower fill factor, we conclude that free charge carrier recombination is an additional loss mechanism further reducing the quantum efficiency. This is due to their relatively high effective Langevin recombination coefficient as discussed above.

Parameter	Sample 1	Sample 2	Sample 3	Sample 4	Sample 5
ΔT/T after 1 ns	0.95	0.95	0.8	0.63	0.51
f	0.59	0.57	0.51	0.58	0.68
$f\times$ ΔT/T(1 ns)	0.56	0.54	0.41	0.37	0.35
max EQE	0.6	0.55	0.45	0.3	0.28

Table 5.3: This table shows a comparison between the ratio of free charge carriers and the maximum external quantum efficiency value for all five samples. The ΔT/T value after 1 ns is extracted from the PIA kinetics in the short delay measurement shown in figure 5.6(a). This value accounts for the geminate recombination of CT states on the early timescale which we cannot resolve from the long time measurement as it is in the instrument response time. The fraction of free charge carriers on the long timescale (f) is obtained from the fit described in the preceding section. Both values are multiplied to obtain the total amount of free charge carriers and compared to maximum EQE values extracted from figure 5.2(b).

5.6 Conclusions

In this chapter we have analyzed the transient absorption data on the short and long timescale for five samples with different ratios of semi-crystalline and amorphous polymer content. All samples exhibit efficient exciton quenching. We find distinctly higher CT state recombination on the sub 1 ns timescale for the samples with higher amorphous polymer content indicating that a high amount of the initially created charge carriers are tightly bound at the interface and recombine quickly. The effective Langevin non-geminate recombination coefficient was also found to be higher in the samples with mainly amorphous polymer leading to further quantum efficiency reduction due to non-geminate recombination of free charge carriers. The quantum efficiency values for all five samples follow the total amount of CT state recombination, indicating that this is the dominating quantum efficiency loss mechanism and the main difference between the samples, with higher non-geminate recombination also decreasing the EQE and the fill factor of the samples with mainly amorphous polymer content.

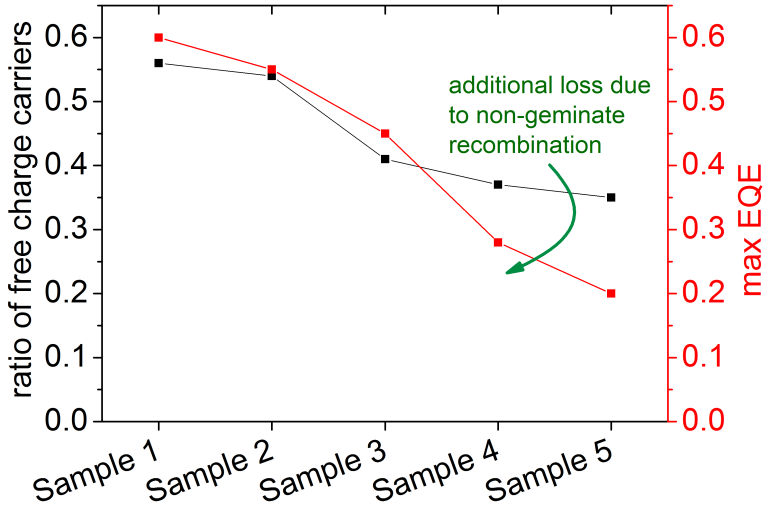

Figure 5.9: This graph shows the amount of free charge carriers on the left-hand axis (in black) as calculated from the PIA kinetics in the short and long delay measurements. The maximum EQE of the samples is shown on the right-hand axis (in red). We can clearly see that the values are very similar, indicating that geminate CT state recombination is the dominant loss mechanism. For Sample 4 and 5, non-geminate recombination of free charge carriers is an additional loss channel.

In conclusion, we found that free charge carrier generation does not improve upon adding amorphous polymer; the sample with only semi-crystalline content exhibited the highest fraction of free charge carriers. This is in agreement with the gradually decreasing EQE values upon addition of amorphous polymer. The only figure of merit that is improved up to a content of 50% amorphous polymer is the open circuit voltage. This could be explained by the amorphous regions breaking up the crystallinity and thus hindering the holes from relaxing into the lowest energy levels. Thus, the amount of energy that can be extracted per hole is higher. However, the increased V_{OC} does not offset the enhanced charge carrier losses, therefore the addition of amorphous polymer leads to a net efficiency decrease.

Chapter 6

Efficiency Limiting Processes in Polymer-Polymer Solar Cells

Organic solar cells with polymers as both donor and acceptor materials are generally limited by low quantum efficiencies. This chapter studies the photophysical processes in a blend of the well-known donor material P3HT and the naphthalenediimide based acceptor material P(NDI2OD-T2). The goal is to investigate the reasons for the low quantum efficiency by following the cascade of processes necessary for free charge generation. First, exciton quenching is examined and is found to be completely efficient for excitation of P3HT but only 50% efficient for excitation of the P(NDI2OD-T2) phase. Using transient absorption spectroscopy, the charge-transfer state generation and recombination on the subnanosecond timescale is investigated. Geminate CT states that recombine on that timescale are found to be a major loss channel both for excitation of the donor and the acceptor material. Subsequently, charge recombination processes on the 1 ns to 1 ms timescale are studied. The transient absorption data is analyzed with multivariate curve resolution to identify different components and their kinetics. It is found that free charges move back to the interface bleaching the absorption of interfacial states in the near infrared. Having established the charge generation and loss processes in the P3HT:P(NDI2OD-T2) system, four samples with different processing conditions leading to different efficiencies are compared, the main difference is found in the CT state recombination on the early timescale. Finally, the chapter concludes with an analysis of the interfacial morphology of

the samples. The photoinduced spectra are influenced by Stark effects which allow conclusions to be drawn about the orientation of polymer chains in interfacial regions. This is confirmed by structural measurements which reveal that free charges are generated at the interface of P3HT and P(NDI2OD-T2) crystals that are oriented face-to-face.

6.1 Introduction

Fullerene derivatives, especially $PC_{61}BM$ and $PC_{71}BM$, have been widely used as electron acceptor materials in organic solar cells. Bulk heterojunction solar cells with blends of a low-bandgap donor material with PCBM have achieved power conversion efficiencies exceeding 8%.[8, 9] The advantages of fullerene materials include their ability to form a nanoscale network with donor materials, their strong electron accepting properties and their high and isotropic electron mobilities.[52] However, the small extinction coefficient of fullerenes at longer wavelengths, the high price and challenging synthesis, and the metastable morphology of polymer:fullerene blends motivates the search for alternative electron-accepting materials.[128, 129]

A new acceptor material has to fulfill manifold requirements:[128, 130]

- Appropriate bandgap ideally complimentary to the donor material, and high extinction coefficient for optimal light harvesting over a broad spectral region.
- High electron mobility to facilitate charge transport to the electrode.
- Optimized HOMO and LUMO levels to achieve efficient charge separation and high V_{OC}.
- Solubility in common solvents to realize solution-based processing of blends with the donor material.
- Favorable phase separation properties and morphology in a blend with the donor material.

- Formation of interfaces with the donor material which favor charge carrier separation.

Conjugated polymeric acceptor materials present an important alternative to fullerenes as they offer great flexibility in optimizing energy gaps for maximum absorption and efficient charge separation depending on the choice of donor material. However, the 2% power conversion efficiencies obtained with polymer:polymer solar cells significantly lag behind polymer:fullerene solar cells.[131–135] The main reason for this performance difference is the low EQE, as shown in figure 6.1. EQE values have not exceeded 50% for polymer-polymer solar cells, a value that was reached by polymer:fullerene solar cells already ten years ago. Recently, Polyera announced the fabrication of a polymer-polymer solar cell with a certified efficiency of 6.4%, demonstrating the potential of polymers as acceptor materials.[136]

The aim of this chapter is to investigate the efficiency limiting processes in a polymer-polymer solar cell. Here, the polymeric electron acceptor material is the naphthalenediimide based donor-acceptor copolymer P(NDI2OD-T2) (see next section for details).[137] Figure 6.2 presents a comparison between optimized bulk heterojunction solar cells based on a blend of the donor material P3HT with either PCBM or P(NDI2OD-T2) as acceptor material. The V_{OC} is around 0.56 V for both acceptors and the fill factor is slightly higher for P(NDI2OD-T2) compared to PCBM (65% vs 60%). However, I_{SC} is substantially lower for the P(NDI2OD-T2) blend, this is in line with the EQE shown in figure 6.2(b). While the EQE exceeds 70% for P3HT:PCBM, it stays below 20% for P3HT:P(NDI2OD-T2). In the following sections we will investigate the reasons for the low photocurrent generation yield, mainly using transient absorption spectroscopy, in order to determine the limitations of charge generation in polymeric acceptors and guide further optimization of polymer:polymer blend systems.

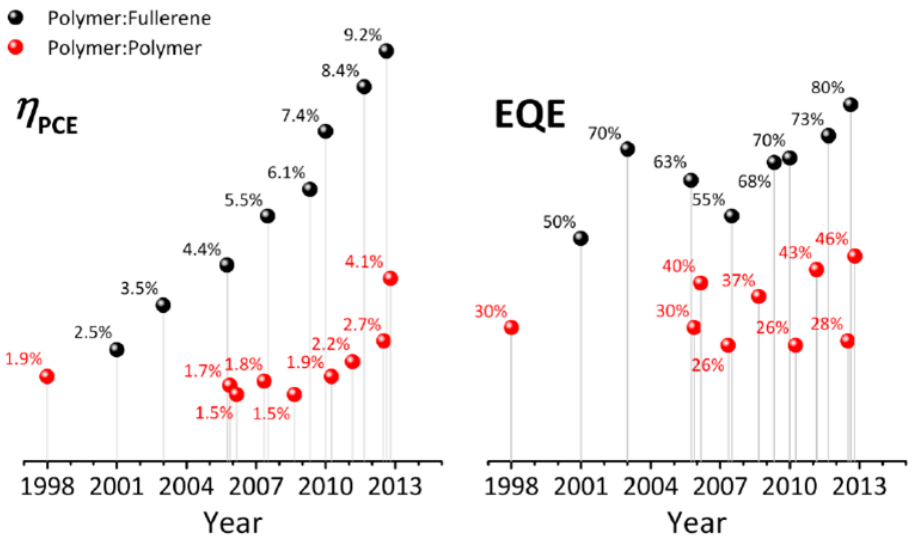

Figure 6.1: Comparison of selected published results for polymer:fullerene and polymer:polymer bulk heterojunction solar cells. While the power conversion efficiency of polymer:fullerene solar cells has steadily risen in the last 10 years, maximum power conversion efficiencies have remained at around 2% for polymer:polymer blends. The main reason for this is that the EQE has remained low, i.e. below 50%, a value that was already reached in the beginning of polymer:fullerene cells more than 10 years ago. Figure courtesy of Marcel Schubert.

6.2 Materials and experimental details

6.2.1 P3HT and P(NDI2OD-T2)

The molecular structures of the donor polymer poly(3-hexylthiophene) (P3HT) and the acceptor polymer poly([N,N'-bis(2-octyldodecyl)-naphthalene-1,4,5,8-bis-(dicarboximide)-2,6-diyl]-alt-5,5'-(2,2'-bithiophene)) (P(NDI2OD-T2), commercial name: ActivInk^{TM} N2200) are shown in figure 6.3. P(NDI2OD-T2) was synthesized by Polyera Corporation. The molecular weight determined by GPC is M_n=26,200 g/mol and M_w=85,200 g/mol. Highly regioregular P3HT was purchased from Rieke Metals (Sepiolid P200 from BASF, regioregularity >98%). The molecular weight determined by GPC is M_n=17,500 g/mol and M_w=32,700 g/mol.

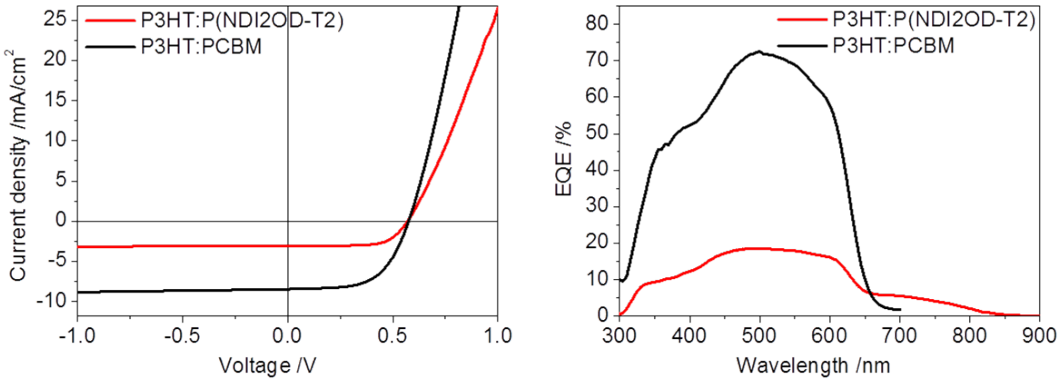

(a) (b)

Figure 6.2: Comparison of solar cell devices with P3HT as donor material and either PCBM or P(NDI2OD-T2) as acceptor material. Figure (a) shows the IV curves, figure (b) presents the EQE of the devices. P3HT:PCBM data courtesy of Fabian Etzold, P3HT:P(NDI2OD-T2) data courtesy of Marcel Schubert.

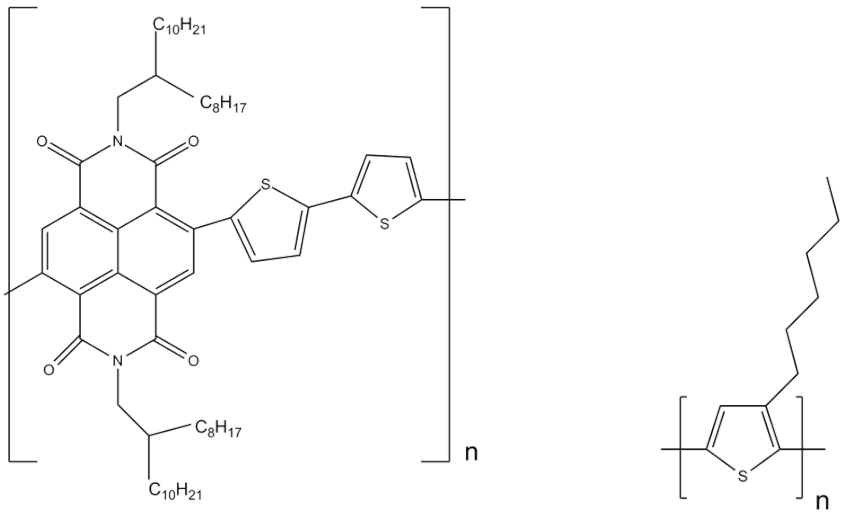

(a) P(NDI2OD-T2) (b) P3HT

Figure 6.3: Molecular structures of the repeat units of (a) P(NDI2OD-T2) and (b) P3HT.

P(NDI2OD-T2) was first reported in Nature in 2009 by Facchetti and coworkers. In that publication it was used as an n-channel material in a complementary-logic circuit with P3HT as p-channel material. Remarkably high electron mobilities up to 0.85 cm^2/Vs were observed for P(NDI2OD-T2) in organic thin film transistors.[137] The field effect hole mobility of P3HT is on the order of 0.01-0.1 cm^2/Vs.[138]

Regarding the absorption properties, P3HT and P(NDI2OD-T2) match very well for the application as donor and acceptor material in bulk heterojunction organic solar cells as their absorption spectra cover different regions of the solar spectrum. This is shown in figure 6.4. P(NDI2OD-T2) exhibits two broad absorption peaks around 400 and 700 nm, while P3HT covers the wavelength region in between. Combining both materials in a blend, the complete solar spectrum from the visible to the near infrared is covered.

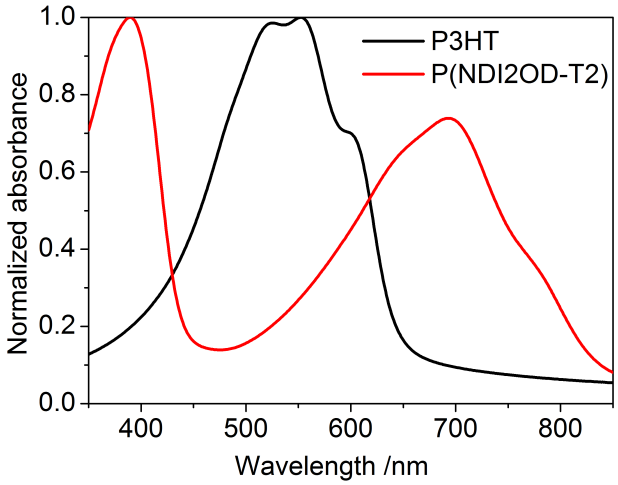

Figure 6.4: Absorption spectra of P3HT and P(NDI2OD-T2). Combining both materials, the wavelength region from 300 to 800 nm is covered, thus making the harvesting of a large part of the solar spectrum possible.

6.2.2 Solar cell performance

The solar cell performance of bulk heterojunction solar cells with P3HT:P(NDI-2OD-T2) blends depends hugely on the choice of solvent and processing conditions. A detailed analysis was carried out by Schubert and coworkers and can be found in [139]. In this thesis, four different samples were investigated. For two samples the P3HT:P(NDI2OD-T2) (1:0.75) blend was spin-cast from a 50:50 solvent mixture of para-xylene (Xy) and chloronaphthalene (CN). Spin-coating was done from a hot solution (>80°C) for 5 s only, then the sample was transferred onto a hot plate and dried at 200°C (Sample 1) and 80°C (Sample 2), respectively. For the other two samples (Sample 4 and Sample 5) the blend was spin-cast from chloroform, Sample 5 was subsequently annealed at 150°C. The device structure of the solar cells was ITO/PEDOT:PSS(35 nm)/blend/Sm(20 nm)/Al(100 nm). Their performance is summarized in table 6.1, figure 6.5 presents the IV-curves and the EQE of the devices. The most efficient device was obtained with the solvent mixture Xy:CN 50:50 and drying at 200°C (Sample 1), the least efficient device was obtained from chloroform without further treatment (Sample 4). Fill factors are high for all samples, and the performance is mainly limited by the low photocurrent. The most efficient sample has EQE values below 20%, while the least efficient has EQE values below 3%.

	Solvent	Treatment	Efficiency %	V_{OC} V	I_{SC} mA/cm^2	FF
Sample 1	Xy:CN	dried 200°C	1.29	0.57	3.1	0.69
Sample 2	Xy:CN	dried 80°C	0.44	0.57	1.1	0.67
Sample 4	CF	as cast	0.11	0.47	0.4	0.58
Sample 5	CF	annealed 150°C	0.38	0.47	1.4	0.58

Table 6.1: Solar cell performance of P3HT:P(NDI2OD-T2) (1:0.75) blends spin cast from different solvents (CN: chloronaphthalene, Xy: para-xylene, CF: chloroform). Data courtesy of Marcel Schubert.

The samples investigated in the TA experiment were prepared as described above, but consisted only of the photoactive blend layer on a quartz glass sub-

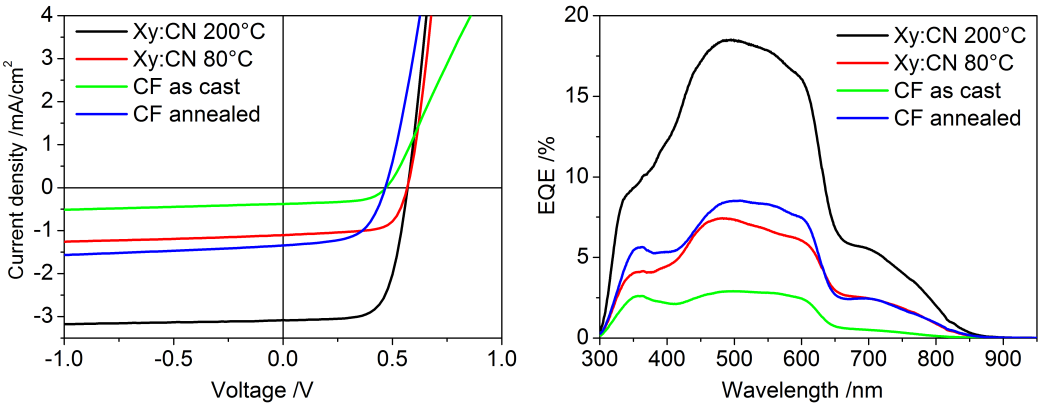

(a) (b)

Figure 6.5: Comparison of solar cell devices with P3HT:P(NDI2OD-T2) (1:0.75) as photoactive blend layer and varying processing conditions. Panel (a) shows the IV curves, panel (b) presents the EQE of the devices. Data courtesy of Marcel Schubert.

strate. All sample preparation was carried out by Marcel Schubert at the University of Potsdam.

6.3 Exciton formation and quenching

As discussed in section 2.2.1 the charge generation process follows a cascade of distinct processes, each potentially severely impacting the overall quantum efficiency of the device. In order to determine the origin of the low photocurrent in the P3HT:P(NDI2OD-T2) devices we will now follow these steps and analyze them individually.

The first step in this cascade is the absorption of photons. Due to the relatively large active layer thickness of 300 nm, almost 100% of the photons at the P3HT absorption maximum for the samples spin-cast from Xy:CN are absorbed (see figure 6.6(a)). For the samples spin-cast from chloroform, the number of absorbed photons is lower but still over 80%. Therefore, we conclude that the majority of incoming photons form excitons inside the active layer, and absorption is not a severe limitation for the photocurrent nor does the change in absorption explain

the order of magnitude loss of EQE between the samples. This is also confirmed by the low IQE values (maximum values of 16%) as shown in figure 6.6(b) for the most efficient sample.

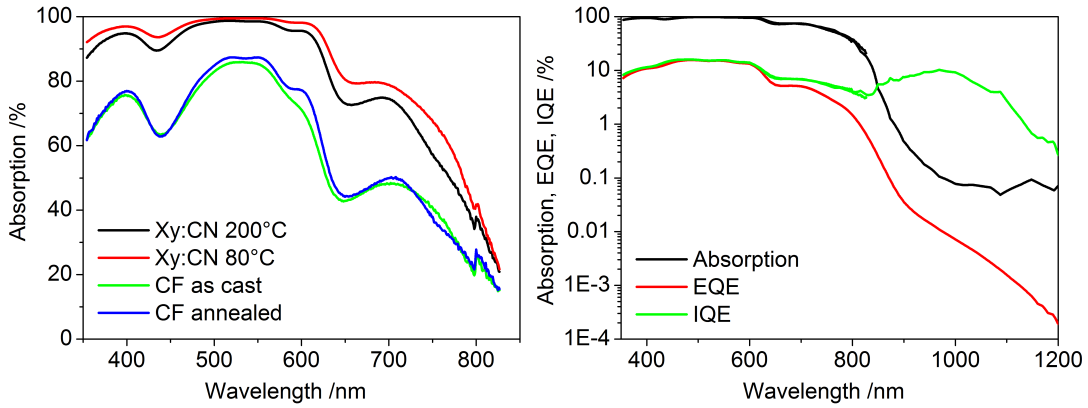

(a) (b)

Figure 6.6: Panel (a) shows the absorption of the four samples as determined with photothermal deflection spectroscopy (PDS). The approximation is used that the beam passes through the sample twice and interference effects are neglected. Panel (b) shows absorption, EQE, and IQE of Sample 1. Data courtesy of Koen Vandewal.

The next step in the cascade is the quenching (by charge transfer) of excitons created after photon absorption. In P3HT:P(NDI2OD-T2) blends this exciton can be created either on the donor or the acceptor material. The efficiency of each of these processes can be probed by measuring the decrease of the PL of the donor (acceptor) in presence of an acceptor (donor).[33] To investigate the PL quenching efficiency for donor and acceptor material separately, the sample is excited either at 500 nm or at 700 nm, to selectively excite P3HT or P(NDI2OD-T2). The results are summarized in table 6.2. For the blends spin-cast from Xy:CN, if an exciton is formed on the acceptor, it has only a 50% probability to be quenched at an interface; meaning that there is a 50% loss in quantum efficiency in the first step after photon absorption on the acceptor (P(NDI2OD-T2)). However, this is not the case for photons absorbed on the donor (P3HT) where the quenching efficiency is over 95% for all samples. The samples spin-cast from chloroform exhibit PL

quenching efficiencies around 90% upon excitation of the acceptor in addition to the quenching efficiency reaching almost 100% upon excitation of the donor. Looking at the IQE spectrum presented in figure 6.6(b) for Sample 1, we see that the IQE in the red part of the spectrum where the absorption is dominated by the acceptor, is significantly lower than in the blue part of the spectrum where the absorption is dominated by the donor. This increased IQE for photons absorbed in the donor is consistent with the photoluminescence quenching results. However, the IQE is significantly lower than the photoluminescence quenching over the entire spectral region meaning that a problem in the cascade subsequent to exciton quenching must be the dominant loss mechanism for photons absorbed on the donor and an additional significant loss mechanism for photons absorbed on the acceptor.

			QE P3HT	QE P(NDI2OD-T2)
Sample 1	Xy:CN	dried 200°C	96%	55%
Sample 2	Xy:CN	dried 80°C	95%	48%
Sample 4	CF	as cast	97%	86%
Sample 5	CF	annealed 150°C	99%	94%

Table 6.2: PL quenching efficiency (QE) of P3HT:P(NDI2OD-T2) blends after selective excitation of donor or acceptor material. Data courtesy of Marcel Schubert.

6.4 Charge-transfer states and ultrafast geminate recombination

The next step in the quantum efficiency cascade is the separation of the interfacial state that is created after exciton quenching. Recent results suggest that the initial population of charge-transfer states follows one of two pathways on the ultrafast timescale, either into free charges or to relaxed CT states (see section 2.2.1.2).[44] The latter population tends to undergo geminate recombination in a

solar cell and therefore is a quantum efficiency loss channel. In order to gain insight into the role of charge-transfer states in determining the quantum efficiency of our samples we combine the techniques of photothermal deflection spectroscopy (PDS) and transient absorption spectroscopy to accurately determine the quantum efficiency of charge separation in directly created charge-transfer states, along with the population flows on the early timescales initiated by photons absorbed on the donor or on the acceptor. We focus on a detailed analysis of the most efficient sample (Sample 1) in this section, and later compare the results with the other samples (section 6.6).

6.4.1 Implications of IQE on CT state splitting efficiency

First we consider in more detail the internal quantum efficiency shown in figure 6.6(b) for the most efficient device (Sample 1) measured from the visible absorption of P3HT, then P(NDI2OD-T2), down to the near infrared absorption of the directly excited interfacial charge-transfer state at wavelengths greater than 850 nm. The IQE was obtained by measuring PDS on samples that were prepared in the same way as the solar cells. The PDS measurements were done by Koen Vandewal in the group of Alberto Salleo. The IQE spectrum has a maximum of around 16% at wavelengths below 650 nm where P3HT dominates the absorption. This drops, as discussed in the section above, to roughly 7% in the region between 650 and 830 nm where P(NDI2OD-T2) is primarily responsible for the photon absorption. Importantly, the IQE then increases again in the sub-bandgap region at wavelengths around 1000 nm where the very weak sample absorption is explained by direct excitation of the interfacial charge-transfer states.[140–142] The IQE of the directly excited CT states is approximately the same as the IQE in the high energy region corresponding to P3HT absorption. This result is consistent with previous investigations of the P3HT:PCBM system which revealed that the internal quantum efficiency of a directly excited CT state was equal to the internal quantum efficiency based on absorption by the P3HT.[140] However, in the current case the internal quantum efficiency is much lower compared to P3HT:PCBM irrespective of the state excited.

To gain more insight into what leads to the low quantum efficiency in these blends, we now turn to ultrafast transient spectroscopy to investigate the flow of excitons into charge-transfer states and how these charge-transfer states then either split into free charges or recombine geminately at the interface. As a first step in this analysis, we present a comparison of the transient absorption surfaces measured for a pristine P(NDI2OD-T2) film, the P3HT:P(NDI2OD-T2) photovoltaic blend after selective excitation of only the lower-bandgap P(NDI2OD-T2) (using an excitation pulse with a wavelength of 800 nm), and finally the same P3HT:P(NDI2OD-T2) photovoltaic blend after excitation of primarily the P3HT component (using an excitation pulse with a wavelength of 530 nm) (see figure 6.7).

6.4.2 CT state formation and recombination after excitation of P(NDI2OD-T2)

In this section we determine the kinetics of charge-transfer state formation and recombination after P(NDI2OD-T2) excitation. In figure 6.8 we show the transient absorption in the region between 525 and 550 nm where P3HT shows an absorption bleach, while P(NDI2OD-T2) excitons show a photoinduced absorption (see also figure 6.7). As P(NDI2OD-T2) excitons move to the interface and create charged states, the P3HT absorption will start to be bleached, making the transient absorption signal move to the positive. This is indeed what we see in the time region of interest marked A in figure 6.8. Fitting the evolution to the positive of the transient absorption signal to a single exponential in this time region of interest yields the violet line and an inverse rate of 0.96 ± 0.04 ps. It was previously observed that the luminescence lifetime of P(NDI2OD-T2) in film is at least 40 ps.[143] If we consider that the luminescence and charge-transfer states were to come from a single pool, our observation that the rate of quenching is at least 40 times faster than the natural rate of decay of the luminescent state would imply that the luminescence should be almost entirely quenched. However, we have previously observed in the steady state luminescence quenching experiments presented in section 6.3 that for excitation of the P(NDI2OD-T2) only about 50% of the luminescence is quenched (see table 6.2). These observations

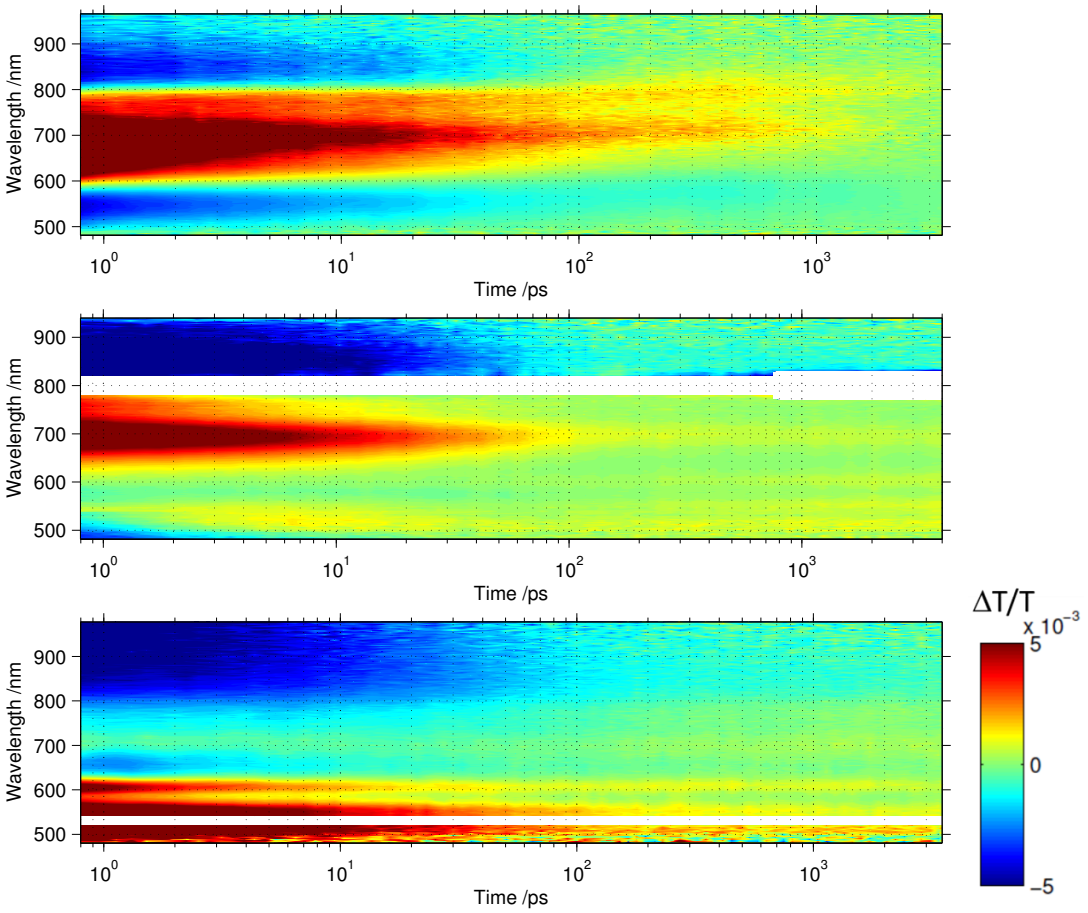

Figure 6.7: Transient absorption surfaces of pristine P(NDI2OD-T2) (first panel), the photovoltaic blend of P3HT:P(NDI2OD-T2)(Sample 1) after selective excitation of the lower bandgap P(NDI2OD-T2) with a 800 nm excitation pulse (second panel), and of the same photovoltaic blend of P3HT:P(NDI2OD-T2) after predominant excitation of the P3HT with a 530 nm excitation pulse (third panel). The redder colors show stronger absorption bleach, bluer colors show stronger photoinduced absorption and green is zero.

lead to the first important conclusion from the transient data: excitation of the P(NDI2OD-T2) leads to two separate population pools. One of these is quenched efficiently by charge transfer with an inverse rate of around 1 ps while the other is not so efficiently quenched and must account for the P(NDI2OD-T2) emission observed under steady-state illumination of the photovoltaic blend.

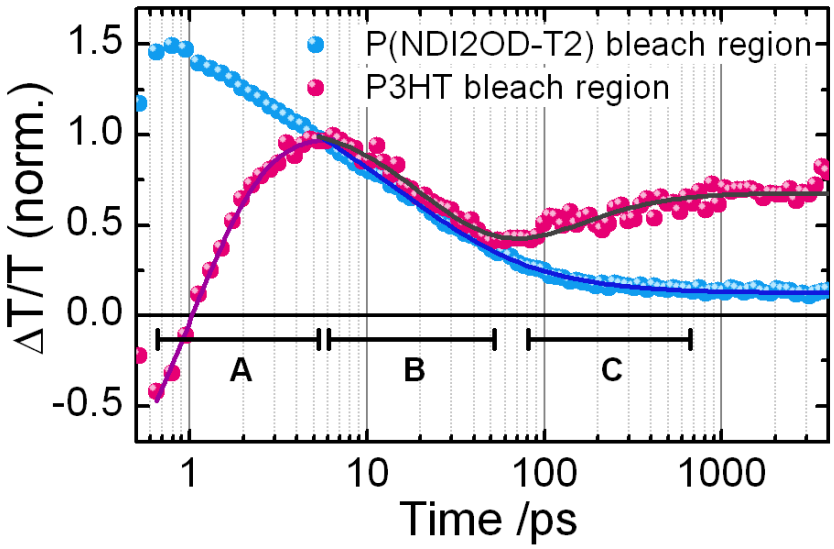

Figure 6.8: Evolution of transient absorption in the blend after selective excitation of P(NDI2OD-T2) with a 800 nm excitation pulse, in the region of the P3HT bleach (525-550 nm, pink spheres) and in the region of the P(NDI2OD-T2) bleach (675-725 nm, blue spheres). Time regions of interest A, B, and C are marked in which the kinetics in the photovoltaic blend are dominated by charge transfer, CT state recombination, and decay of residual excitons respectively. The solid lines are fits to the data (markers) as described in the text.

Looking at the dynamics of the P3HT bleach in the time regions of interest B and C in figure 6.8, we can make another qualitative conclusion. If the charge-transfer state population after exciton quenching were to remain constant (meaning the P3HT bleach would remain the same) and the P(NDI2OD-T2) 'exciton' population were to decrease, the net signal observed in this wavelength region would increase as the photoinduced absorption of the P(NDI2OD-T2) 'ex-

citons' which were masking the P3HT bleach would be removed. We see such behavior in time region C. However, before that occurs the observed TA signal moves towards zero (moving in the direction of negative values) in the time region B. This decrease in P3HT bleach can only be accounted for by a decrease in the population of excited states on the P3HT, or explicitly put, by CT state recombination. So qualitatively we make a second important conclusion, that following the CT state formation, some fraction of the CT states recombine surprisingly quickly diminishing the P3HT bleach on a sub-hundred picosecond timescale. This ultrafast CT state recombination will reduce the device quantum efficiency.

In order to quantify how much this fast CT state recombination effects quantum efficiency we use the following simple model to concurrently fit the transient signals observed in the regions of the P3HT and P(NDI2OD-T2) bleaches. We estimate (in accordance to the conclusion above) that the initial photoexcitations are split into two population pools, one of which creates CT states and/or free charges and one of which is dominated by long-lived P(NDI2OD-T2) excitations which decay without undergoing charge transfer. Furthermore, the first pool is further split into two sub-pools (in accordance to the qualitative conclusion made above); one of which is CT states which recombine quickly, and the other of which are longer-lived charge-separated states that do not recombine on this short timescale. We start our modeling at 5 ps when charge transfer is already complete, and the first population pool is at its maximum. We then assume that the decay of the CT states in the first subpool of population 1, and the decay of the P(NDI2OD-T2) excitations in population 2 can both be parametrized by a stretched exponential function. The evolution of the transient signals can then be written as:

$$\Delta \mathrm{T/T}_i = A_i \left(p_{1a} e^{-\left(\frac{t}{\tau_1}\right)^{b_1}} + p_{1b} \right) + B_i e^{-\left(\frac{t}{\tau_2}\right)^{b_2}} \tag{6.1}$$

where A and B are constants relating to the splitting of the population between the pools and the absorption cross section of each pool in each wavelength range, the remaining parameters are shared between the wavelength regions: p_{1a} represents the fraction of the pool 1 that recombines with a rate described by τ_1 and b_1, p_{1b} represents the fraction of the population that is long-lived, and τ_2 and b_2 represent the decay of the long-lived P(NDI2OD-T2) excitations. The results of

this global fit are shown as the red and dark blue lines in figure 6.8, and it is clear that the population evolutions in this simple model can accurately reproduce the observed transient absorption data. The extracted parameters are shown in table 6.3. A and B are not directly physically interpretable, as they contain information regarding initial population, the cross-sections, and our normalization, however the other parameters are all directly interpretable. The negative sign for B in the P3HT bleach region confirms that the P(NDI2OD-T2) excitations have a photoinduced absorption in this region, as observed in the pure film in the first panel of figure 6.7. We find that only roughly 30% of the CT states formed create long-lived species, with the majority decaying on the sub-hundred picosecond timescale. Combining these results with the steady state quenching observations we can approximate the upper bound of the IQE as 0.50 (due to incomplete quenching) multiplied by 0.30 (due to fast CT state recombination), which yields an estimate of 0.15. This is still roughly a factor of 2 larger than the observed IQE in the P(NDI2OD-T2) region, indicating perhaps that not all the long-lived charged states of population 1 are free charges that are extracted in a device. Nonetheless, the combination of incomplete quenching and fast CT state recombination explain the majority of the quantum efficiency loss after excitation of P(NDI2OD-T2). So we can robustly explain the principle loss channels limiting the EQE after P(NDI2OD-T2) excitation.

	p_{1a}	p_{1b}	τ_1/ps	b_1	τ_2/ps	b_2	A	B
P3HT	0.7±0.1	0.3±0.1	17±2	0.8±0.1	8±4	0.4±0.1	2.2±0.4	-3.3±0.7
NDI							0.4±0.1	1.3±0.3

Table 6.3: Parameters extracted from fitting the bleach regions of P3HT and P(NDI2OD-T2) with equation 6.1. The fit is shown in figure 6.8. Except for A and B all parameters are shared.

6.4.3 CT state formation and recombination after excitation of P3HT

We now turn to investigate the excitation flows following excitation of the P3HT in the photovoltaic blend (excitation wavelength 530 nm), and check whether sub-nanosecond CT state recombination also strongly limits the EQE in this case. In figure 6.9 we show the normalized transient absorption spectra measured at various time delays after excitation.

Two interesting features are immediately apparent upon examination of the data. First in the spectral region marked 'A' in figure 6.9 we see at short time a contribution of the stimulated emission of P3HT. This decays quickly (within a few picoseconds), leaving a net negative signal that is a superposition of the charge carrier induced absorption and the bleach of the P(NDI2OD-T2). By roughly 200 ps we see that the positive double peak at around 700 and 780 nm of the P(NDI2OD-T2) bleach is apparent; and the features from this point on are caused by long-lived charge carriers. This signal only becomes positive after several hundred picoseconds, perhaps when the charge carriers in the P(NDI2OD-T2) (negative polarons) reach the more ordered regions of the polymer. Along this line, the earliest time spectrum after P3HT excitation shows a clear shoulder in region 'B' which is known to arise from intrachain absorptions in ordered P3HT regions. As the P3HT excitons move to the interface and create charge carriers this bleach due to excited states in an ordered P3HT region decreases. This suggests that the interfacial region is less ordered (on average) than where the P3HT excitons are created within the domains. However, on the timescale of 30 ps this bleach returns, likely as there is some return of mobile charge carriers to the ordered regions of the P3HT. These interesting observations suggest that both polymers are more disordered in the interfacial regions where charge carriers are generated, a fact that could well have some influence on the charge carrier separation, and that we will discuss later in relation to the long-time TA measurements.

In order to get a rough estimate of the charge carrier population decay we can look at the signal kinetics at wavelengths greater than 870 nm which are least affected by the disorder-related peak shifting. We present this in figure 6.10,

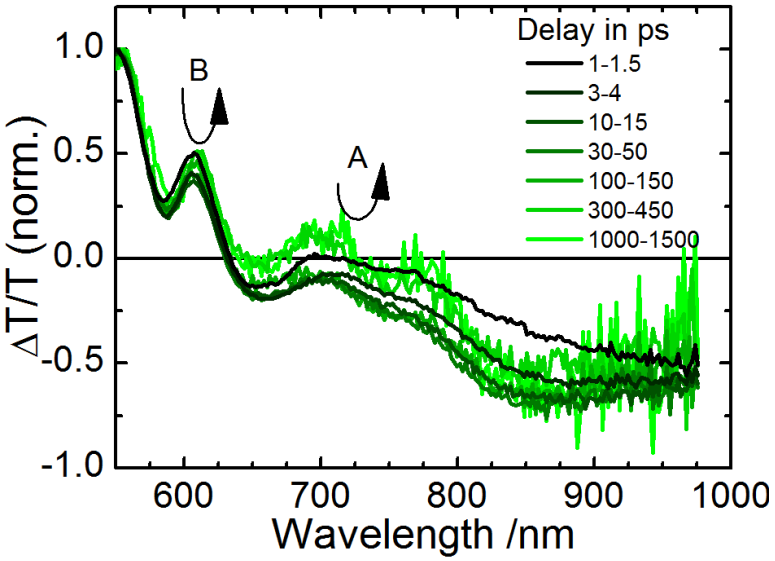

Figure 6.9: Evolution of the transient absorption spectra (normalized to the maximum P3HT bleach) of the photovoltaic blend after excitation of the P3HT component (excitation wavelength 530 nm) . The region labeled A shows an initial decrease of the P3HT stimulated emission on a timescale of a few picoseconds, followed by an increase of the P(NDI2OD-T2) bleach on the long timescale as the excitons move to more ordered regions of the polymer. A similar evolution is seen in the bleach of the ordered P3HT region marked with B. Here, the P3HT excitons move from ordered phase regions to disordered interfacial regions on the same few picosecond timescale of the stimulated-emission quenching; then the bleach of the ordered P3HT regions gradually recovers, perhaps as charges move back away from the interface.

where we show the average photoinduced absorption between 870 and 950 nm as a function of time (normalized to its value after 10 ps when charge carrier formation is complete judged by the disappearance of the P3HT stimulated emission signature). We see that a very significant fraction of the signal decays, indicating that a significant fraction of the charge carriers created from P3HT excitons recombine on an ultrafast timescale. In this behavior, they are similar to charge carriers created via P(NDI2OD-T2) excitons. Due to the pronounced shifting of excitons and later charge carriers between ordered and disordered regions after P3HT excitation, we cannot precisely quantify the fraction of charge-carriers created from P3HT excitons that quickly recombine. We can say that, as shown in figure 6.10, the PIA signal decays within a few hundred picoseconds to 15% of its value after charge transfer is complete. This is a clear indication that charge carrier dynamics are broadly similar after P3HT excitation and P(NDI2OD-T2) excitation, and certainly consistent with fast charge carrier recombination also being the dominant loss mechanism of the IQE in the P3HT absorption region. In conclusion, we can clearly say that losses on the order of 70–85% in the interfacial CT state (as suggested by the steady-state spectroscopy) are reasonable, and that we can directly observe the sub-nanosecond CT state recombination that leads to this loss.

6.5 Free charge recombination: observing the return to the interface

Having established that ultrafast geminate recombination of charge-transfer states on the sub-hundred picosecond timescale is the dominant loss mechanism limiting quantum efficiency, we now turn to investigate the processes on the longer timescale in order to find additional loss mechanisms that further limit the photocurrent. We do this using transient absorption spectroscopy in the long delay range with various excitation intensities at an excitation wavelength of 532 nm. At 532 nm mainly P3HT is excited. As we have observed in the previous sections, spectral features of the two blend components overlap over the whole spectral range. For example in the region between 700 and 800 nm the photoinduced

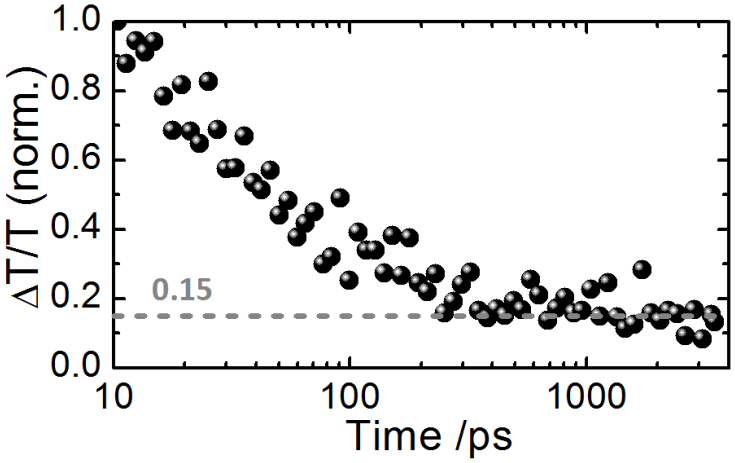

Figure 6.10: Evolution of the photoinduced absorption between 870 and 950 nm after excitation of the P3HT component of the blend. The signal decreases significantly, consistent with significant recombination of CT states on the sub 200 ps timescale.

absorption of P3HT and the ground state bleach of P(NDI2OD-T2) lie on top of each other, making the net signal small and making it difficult to distinguish between different species, and hard-modeling analysis impossible. However, using the multivariate curve resolution as introduced in section 2.4.2 we can successfully find physically reasonable decomposition of the data which reveal how free charges move back to the interface and recombine. This is confirmed by additional TA measurements in the NIR between 1200 and 1700 nm where we observe the bleach of interfacial states. The analysis in this section is again shown only for Sample 1, however, the analysis was also carried out for the other samples and an analysis of the differences between the samples will be presented in section 6.6.2.

6.5.1 Disentangling long-lived components

6.5.1.1 Workflow of MCR analysis

Following the workflow shown in figure 2.20 on page 42, we first carry out evolving factor analysis on the individual intensities of the fluence series. This is shown in figure 6.11(a) for the 255 nJ fluence. For all fluences we find that the matrix is

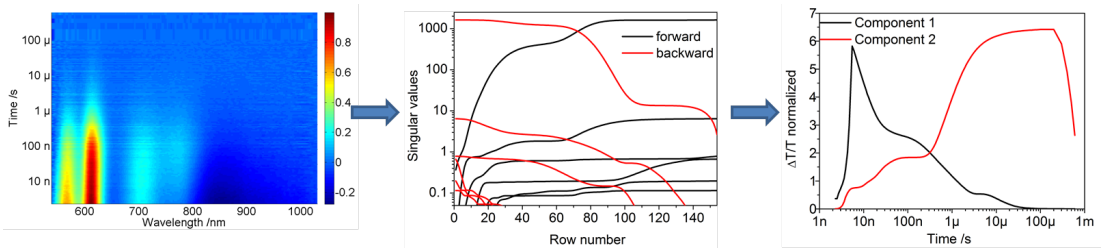

(a)

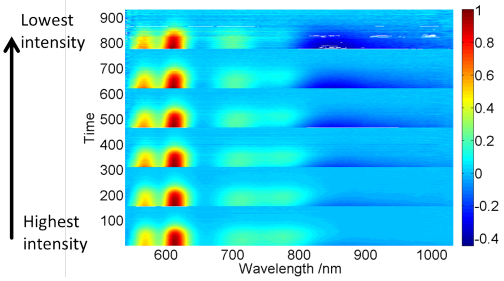

(b)

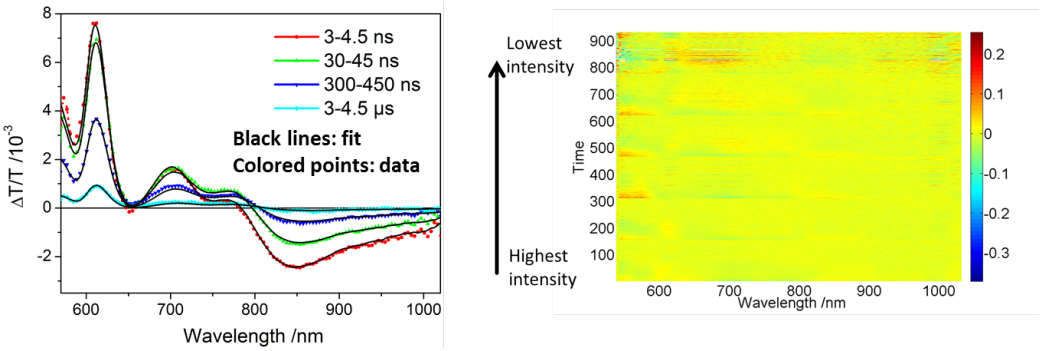

(c)

Figure 6.11: MCR analysis of the most efficient sample (Sample 1). Panel (a) shows the data surface for excitation at 255 nJ on the left-hand side. Evolving factor analysis is carried out to determine the number of components in the system (central panel) and from that an initial guess for the concentration profile of two components is made (panel on the right). From MCR analysis of that dataset we obtain an initial estimate of the spectra that can then be used for the analysis of the augmented dataset shown in panel (b), which contains a fluence series with six different intensities ranging from 840 to 74 nJ. Panel (c) demonstrates that the obtained fit is very good, on the left-hand side spectra at selected timepoints are compared with the simulated data, on the right-hand side a surface plot of the difference between the measured and the simulated data is shown.

rank 2 at early times. However, in the backward-going EFA, the data matrix can be described by only one singular value for a long time. Therefore it can be concluded that only one single species accounts for the absorption left at long-time. Thus we know the number of relevant components, that is 2, and we can identify an important constraint for the following analysis, that is the concentration of one species is 0 at late times (species 2). This constraint is equivalent with the constraint that one spectrum is known: the spectrum that is left at long times is the spectrum of one component (species 1). From evolving factor analysis we also obtain an initial guess for the concentrations. The optimization process incorporating the constraint that the concentrations should be non-negative and the known spectrum is carried out for the 255 nJ fluence. The resulting spectra are used as an initial guess for the MCR analysis on the whole fluence series. To that end we use an augmented transient absorption surface which is generated by placing the individual surfaces on a common wavelength axis and an extended time axis with the fluences decreasing in excitation intensity. The fluence series surface is shown in figure 6.11(b). All intensities are normalized to their maximum value respectively. The MCR-ALS optimization process is now carried out with the whole fluence series, including the non-negativity constraint and the known spectrum. Figure 6.11(c) demonstrates the quality of the fit. A comparison between spectra at selected timepoints with the simulated data shows good agreement (left-hand side). The surface plot of the difference between the measured and the simulated data shows that the error is due to noise and not due to systematic deviations (right-hand side).

The obtained resolved spectra and concentration profiles are now reviewed in terms of their linear transformation ambiguity using the method presented in section 2.4.2.4.

6.5.1.2 Results of MCR analysis

Figure 6.12(a) shows the resolved spectra and concentration profiles obtained from MCR-ALS on the augmented data surface of Sample 1. We know that the spectrum of species 1 is correct, as it is the only species left at late times. Thus we also know the (normalized) population evolution of species 2. However, we still

have to investigate how the spectrum of species 2 and the population evolution of species 1 can be changed by mixing. We can do that by running a linear sweep of c from positive to negative values (see equation 2.27 on page 47, $b = 0$). Rotating the data obtained directly from the analysis (figure 6.12(a)) to negative values makes the model more sequential, as demonstrated in figure 6.12(b). At values $c < -1$ the kinetics of species 1 become negative for the lowest fluence, violating the non-negativity constraint of the concentration profiles. Rotating to positive values makes the model more parallel as shown in figure 6.12(c). The spectra and concentration profiles shown in figure 6.12 are all mathematically equally correct solutions of the data matrix. However, we want to find the unique physically correct solution.

6.5.1.3 Physical interpretation of results

By carefully considering the spectra and the corresponding kinetics, we aim to come close to the actual decomposition C_a and S_a. It is immediately apparent that the spectra for species 2 in figure 6.12(c) do not make physical sense as they are almost mirror images of the spectrum for species 1. As both species bleach the P3HT and the P(NDI2OD-T2) absorption, we expect to find similar bleach features in both spectra. For the spectra in figure 6.12(a) the P3HT bleach is shifted from one species to the other which also makes the solution physically improbable. The spectra in figure 6.12(b) with a rotation value of $c = -1$ is more physically sensible: The P3HT bleach of both species is very similar, and also a P(NDI2OD-T2) bleach feature around 700 nm is found for both species. The populations are still always positive, which is not the case for rotation to more negative c values.

For easier visibility, our best estimate (based on the rotational analysis) of the actual spectra and augmented kinetics is shown again in figure 6.13. The main difference between the spectra is found at wavelengths greater than 750 nm: Here, species 2 exhibits a broad photoinduced absorption while species 1 has an additional bleach feature which extends into the NIR. Taking a closer look at the normalized kinetics for all excitation fluences, shown in figure 6.14, we find that

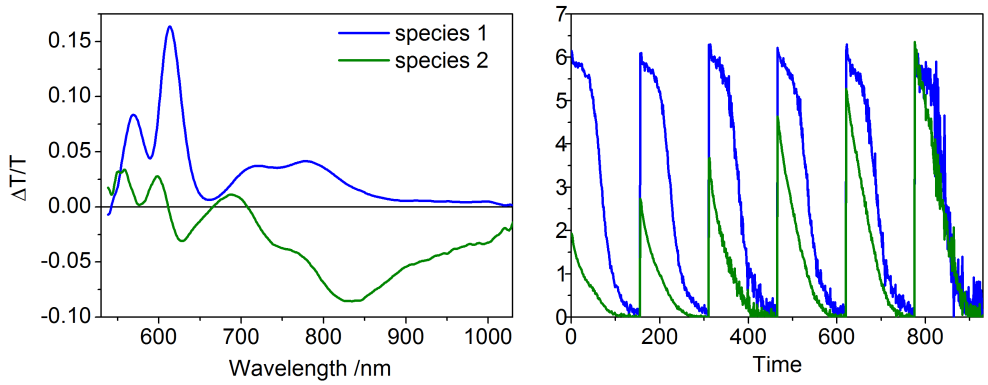

(a) $c = 0$

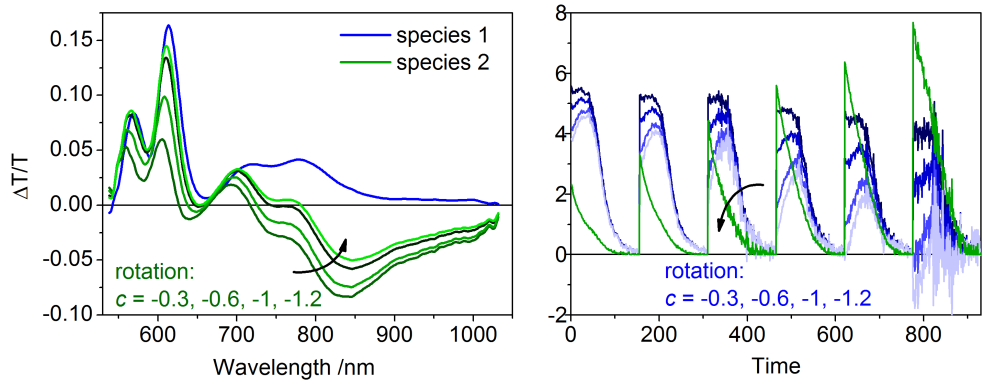

(b) Rotation $c < 0$

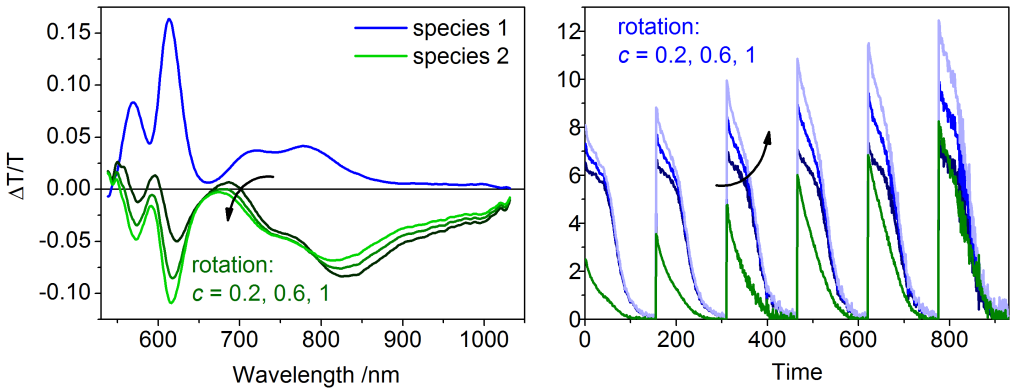

(c) Rotation $c > 0$

Figure 6.12: Spectra and kinetics obtained from MCR-ALS analysis on the fluence series of Sample 1 for different rotation values as indicated in the graphs. The kinetics of the different fluences are shown on an extended time axis with the highest fluence first and the lowest fluence last.

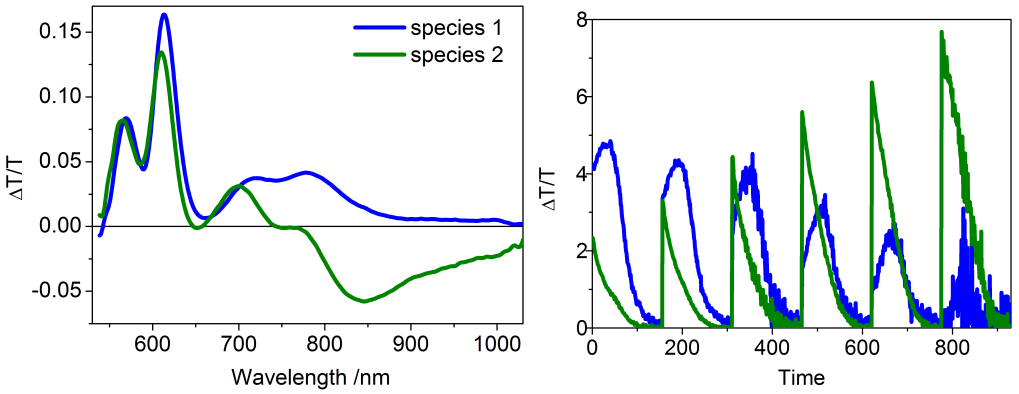

(a) Spectra (b) Kinetics

Figure 6.13: Actual decomposition of measured data found by rotating the solution from MCR-ALS by a value of $c = -1$. Panel (a) shows the spectra of species 1 and 2, panel (b) shows the corresponding augmented kinetics with the excitation intensity decreasing along the x-axis.

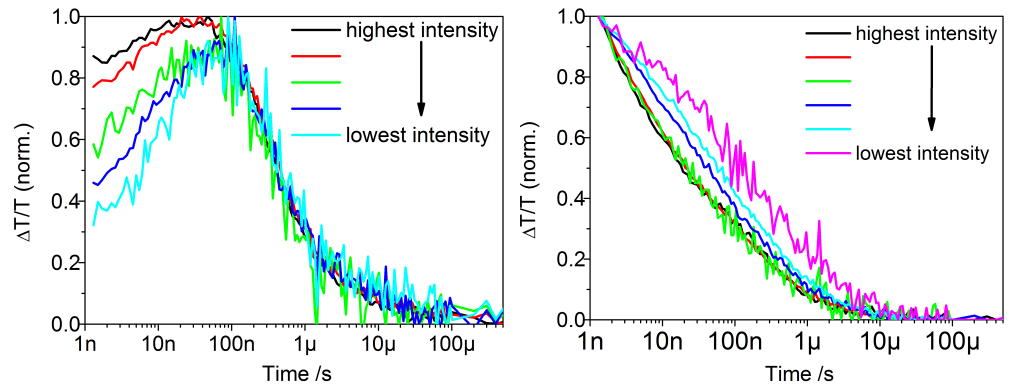

(a) Species 1 (b) Species 2

Figure 6.14: Normalized kinetics for both species as shown in figure 6.13 for a rotation value of $c = -1$.

the kinetics of species 2 (figure 6.14(b)) are excitation intensity dependent, therefore we conclude that this species is free charges. The kinetics of species 1 (figure 6.14(a)) exhibit a rise time that is dependent on intensity and subsequently, after about 50-100 ns, an intensity independent decay. We assign this species to interfacial states that are created by free charges moving back to the interface. Interestingly, we observe the bleach of the interfacial state absorption as $\Delta T/T$ moves from negative to positive for the wavelength region up to 1050 nm. This is in agreement with PDS measurements (as presented in figure 6.6(a)) where the interfacial CT state absorption in the P3HT:P(NDI2OD-T2) blend gives an absorption tail extending into the NIR. At higher charge densities, the recapture of free charges to the interface takes place faster. Recombination of these charges trapped at the interface is intensity independent and slow (on a timescale of 100 μs), perhaps opposite charges tend to be trapped at low-energy sites both at the interface but offset from one another horizontally. The increased disorder at the interface compared to the bulk material might keep the charges at the extraordinarily low-energy sites and hinder them from hopping away again. We will see in the next section that direct evidence of the return of free carriers to the interface and the bleaching of interfacial states is also found in the NIR transient absorption experiments extending up to 2000 nm.

6.5.2 Evidence of interfacial states in the infrared TA

Transient absorption experiments were carried out in the wavelength region between 1200 and 1700 nm in order to check whether the return of free carriers to the interface could be directly observed by alteration of the CT state bleach in the NIR. Figure 6.15(a) shows the transient absorption spectra at time delays between 1 ns and 4.5 μs after excitation at 532 nm. The first spectrum at a time delay of 1-1.5 ns shows a broad photoinduced absorption over the whole spectral range. This can be assigned to the PIA of free charge carriers. Surprisingly for the infrared region, the spectrum becomes positive after about 2 ns and keeps rising to more positive values on a timescale of several 10s of nanoseconds depending on the excitation intensity. This rise to a net positive signal in the NIR is direct evidence that interfacial states are formed by free charges returning to

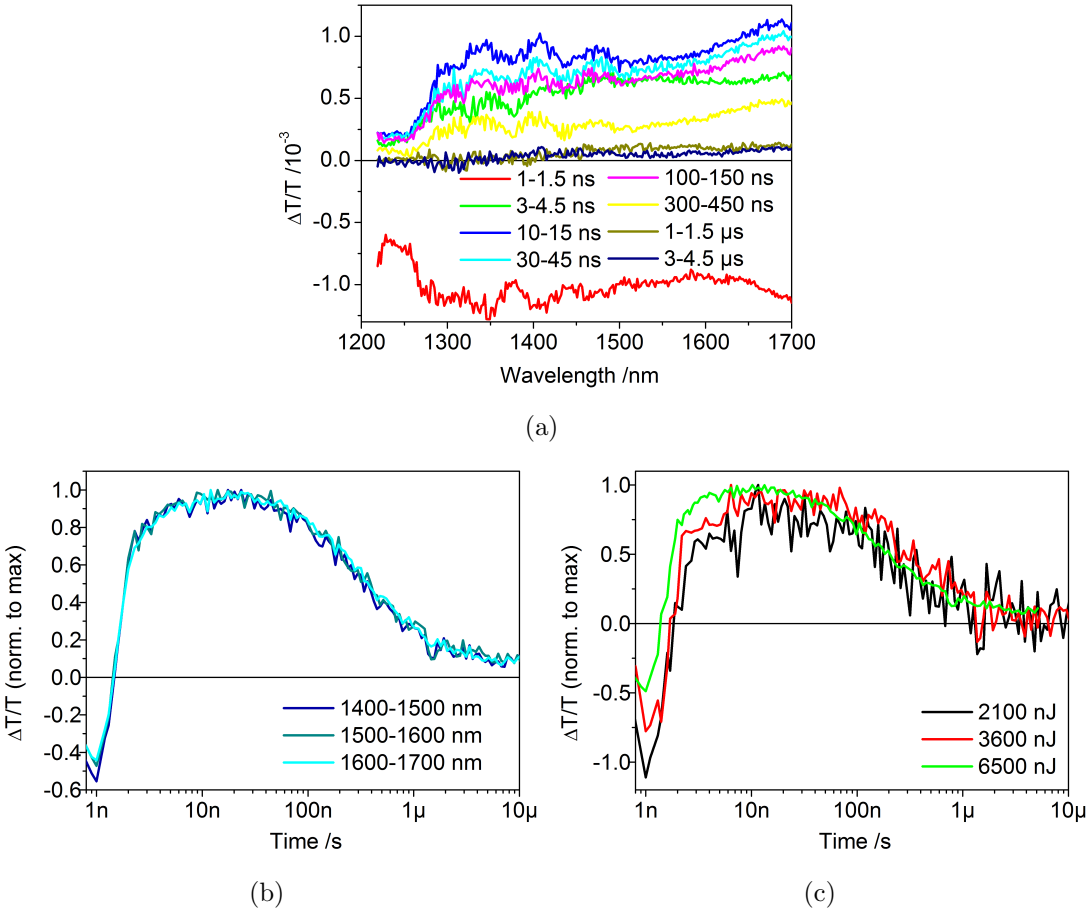

Figure 6.15: Transient absorption measurements in the NIR for the P3HT:P(NDI2OD-T2) blend (Sample 1) after excitation at 532 nm. Panel (a) shows the spectra at time delays specified in the graph. Panel (b) demonstrates that the kinetics are the same over the whole wavelength region. Panel (c) shows the integrated kinetics between 1400 and 1700 nm at different intensities, normalized to the maximum.

the interface as proposed in the preceding section. No other features can explain an absorption bleach at such long wavelengths. Figure 6.15(b) shows that independent of the wavelength region a bleach arises and the kinetics are very similar, indicating a wide variety of low energy states exist near the interface. Normalizing to the maximum (figure 6.15(c)) shows again that the decay kinetics are intensity independent while the rise time is dependent on intensity (compare

figure 6.14(a) for the same results in the visible wavelength range). The kinetics in the infrared directly relate to the kinetics found for the interfacial state in the visible wavelength range providing strong support that our decomposition of the visible data reveals a good approximation of the actual concentration and spectra profiles.

6.5.3 Implications of return to interface for solar cell devices

Taking a closer look at the return of the charge carriers to the interface in both the visible and near infrared dynamics, we find that we can distinguish two time regions. In the timescale below 5 ns we find a very fast $\Delta T/T$ signal rise independent of the excitation intensity, while on a longer timescale (up to several hundred nanoseconds) the signal rise time is intensity dependent and slower. For the measurements in the near infrared (see figure 6.15(c)), the normalized $\Delta T/T$ of the interfacial bleach is >0.5 after less than 3 ns independent of the excitation intensity. Similarly, the kinetics of the interfacial states extracted from visible measurements, shown in figure 6.14(a), show a normalized $\Delta T/T$ of >0.4 already in the time resolution of the experiment (about 1 ns) independent of the excitation intensity. The following signal rise depends on intensity in both measurements (NIR and VIS), the maximum signal is reached after 20 ns at the highest intensity measured, but only after 110 ns at the lowest intensity measured.

We therefore conclude that two different mechanisms, one geminate and fast, the other non-geminate and slower, are responsible for the return of the charge carriers to the interface on the >100 ps timescale. The two mechanisms are schematically depicted in figure 6.16. Judging from the contribution to the kinetics, about 40–50% of the charges left after 100 ps have not fully escaped their mutual Coulomb attraction, and hop back to the interface under each others influence on the sub 5 ns timescale (a geminate process, see figure 6.16(a)). The remaining charge carriers (about 50–60%) have escaped their Coulomb attraction and become truly independent free charge carriers. Their return to the interface then depends on coming again under the influence of an opposite charge carrier, exactly like normal non-geminate recombination (see figure 6.16(b)). The rate

of this process depends on the charge density, therefore occurs at a rate that depends on the excitation intensity. At the lowest intensities we measure, which still create charge densities somewhat above that expected in a solar cell under steady-state solar illumination, the rate of the return of free charge carriers to the interface through this non-geminate process is on the order of 100 ns. We note, that as previously discussed, once formed, the interfacial states lead to charge carrier recombination, but that process is slow, likely as the opposite charge carriers are located in low energy sites slightly laterally offset from each other.

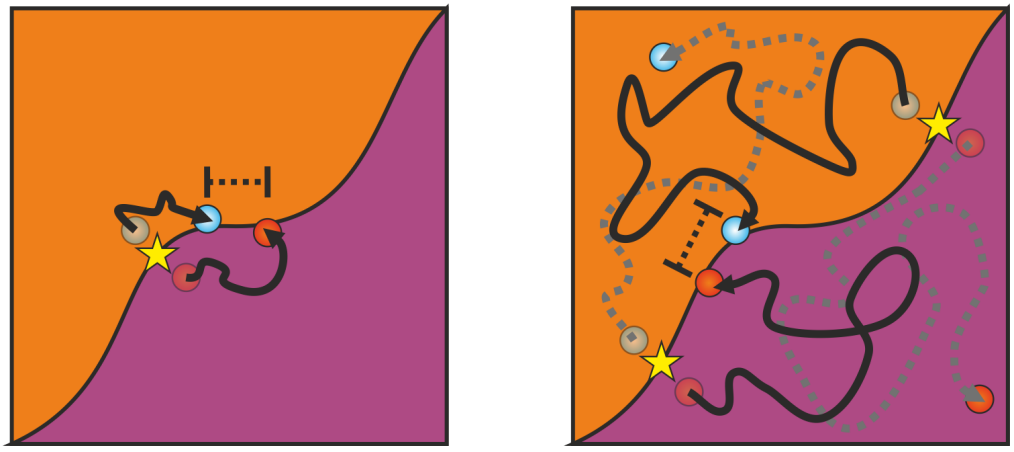

(a) geminate (b) non-geminate

Figure 6.16: Schematic illustration of the recombination mechanisms involving interfacial states. The geminate filling of the interfacial states shown in panel (a) takes place on the sub 5 ns timescale and originates from charges that have not fully escaped their mutual Coulomb attraction. The non-geminate filling of the interfacial states shown in panel (b) originates from free charges and takes place on a timescale of about 100 ns dependent on excitation intensity. About 40–50% undergo the geminate process, about 50–60% the non-geminate. Recombination from the interfacial states is slow as the charges are laterally offset from each other.

In order to identify the influence of the return of charge carriers to the interface on solar cell performance, we calculate the transit time $t_{transit}$ of a charge carrier in a solar cell device with $t_{transit} = \frac{d}{\mu \cdot F}$, where d is the active layer thickness, μ is

the charge carrier mobility, and F is the field. We use an active layer thickness of 300 nm [139] and a mobility of μ=0.05 cm^2/Vs (see section 6.2.1), and obtain a transit time of 30 ns at V_{OC}. The non-geminate formation of interfacial states from free charge carriers occurs on a timescale greater than 100 ns. Therefore, in a solar cell the rate of extraction is much faster than the rate of recombination, and the free carriers will be swept out efficiently at most internal fields. This is consistent with the very high fill factor of the devices. The high fill factor implies that there is little dependence of the photocurrent on the field within the device. This further implies that there is no significant mechanism of free charge carrier generation that is field dependent. Thus, the interfacial states created by geminate return to the interface appear not to be split by the field within the device. This would mean that this channel of geminate formation of interfacial charge states is an additional quantum efficiency loss mechanism, that further reduces the photocurrent by a factor of around 0.5 on top of the ultrafast charge-transfer state recombination.

6.5.4 Temperature dependence of return to the interface and recombination

In order to gain more insight into the cause of the return of free carriers to the interface and the subsequent recombination, we investigated the process also at low temperature. At lower temperature, the average mobility of charge carriers decreases. A second effect of low temperatures is an increase in the density dependence of the mobility which can be explained taking into account the broad density of states caused by disorder. At higher temperatures charges occupying sites in the low-energy tail of the DOS still exhibit reasonable mobilities as they can make thermally assisted hops to higher sites in the DOS. At low temperatures however, this thermal assistance is lost and the mobility of the charges in tail states becomes considerably lower than that of states higher in the DOS.[55, 70]

Figure 6.17 presents spectra and kinetics of a transient absorption experiment at the same excitation intensities at room temperature (RT) and liquid nitrogen temperature (ca. 80 K). The spectra, shown in the upper panel, differ between the two temperatures: At 80 K the spectra are more structured as less vibronic

levels are accessible and the features are also red-shifted compared to the RT measurement as higher energy-levels are not accessible. We now turn to look at three different wavelength regions: First, the P3HT bleach shows an increased recombination in the first 100 ns at low temperatures with very little intensity-dependence. We therefore ascribe the recombination to geminate charge carriers which are not able to escape each others attraction due to their reduced mobility. It is possible that at room temperature these are the sites that lead to the intensity independent built up of interfacial states. However, charge carriers created higher in the DOS can efficiently create free charge carriers at low temperatures. After about 1 μs, more signal is left in the 80 K measurement. This signal can be ascribed to the free charges, which exhibit slower non-geminate recombination and also an increased charge-carrier density dependence. The second panel shows the kinetics of the lower energy spectral feature of the P(NDI2OD-T2) bleach to which charges at the interface play a significant role (compare the spectrum of species 1 in figure 6.13(a)). These interfacial states are filled up slightly faster at 80 K, this is in agreement with the charges not being able to escape each other as far as at room temperature. In the photoinduced absorption region above 900 nm (third panel) a slower rise time is observed for the low temperature signal. The slower recombination of free charge carriers contributes to this, but another significant contribution is likely the lower absorption bleach of interfacial states in that wavelength region, as at low temperature the absorption of the interfacial state population is expected to be red-shifted out of this wavelength range.

In conclusion, we find that at low temperature charges cannot escape the interface as well as at room temperature due to their reduced mobility. Therefore, the attraction of the opposite charges is still higher and interfacial states are populated more quickly. However, the charges which overcome the attraction at the interface and are dissociated in their respective phases are longer lived and their recombination kinetics exhibit a distinct intensity dependence. This picture is consistent with our analysis of the room temperature data, and supports our interpretation that the fast return to the interface of some charge carriers due to their motion in the static disorder and Coulomb attraction leads to an additional quantum efficiency loss channel.

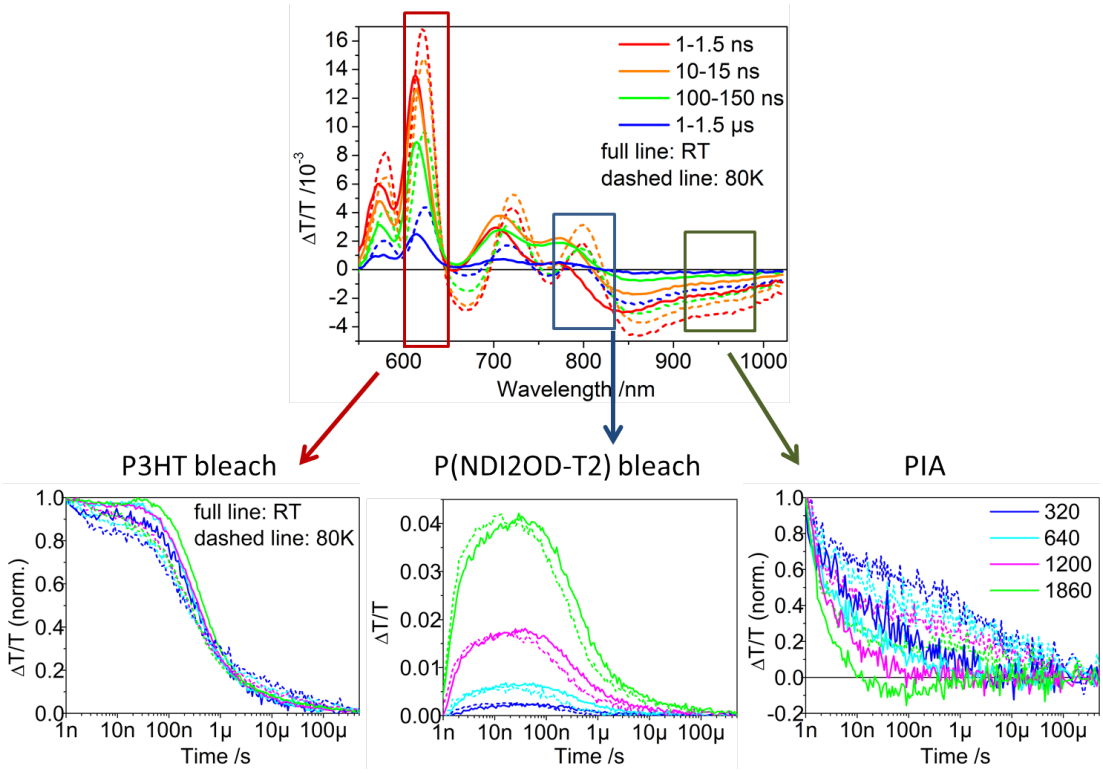

Figure 6.17: Transient absorption fluence series measurement of Sample 1 after excitation at 532 nm at room temperature (291 K) and liquid nitrogen temperature (80 K). The sample was excited at 320, 640, 1200 and 1860 nJ. The upper panel shows a comparison of the spectra at different time delays specified in the panel after excitation at 320 nJ. The kinetics for three different spectral regions are shown in the lower panels: P3HT bleach normalized (RT: 605-625 nm, 80 K: 610-630 nm), P(NDI2OD-T2) bleach (RT: 760-780 nm, 80 K: 780-805 nm), PIA normalized (RT&80 K 925-975 nm). In each panel the room temperature measurement is shown with full lines, the 80 K measurement with dashed lines.

6.5.5 Summary of long time recombination dynamics

From the analysis of transient absorption data in the 1 ns to 1 ms time-range we conclude that the charge carriers left after 1 ns recombine through interfacial states. The interfacial states can be observed due to their absorption bleach in the near infrared. Two different regimes of charge carriers returning to the interface can be distinguished, one geminate and fast, the other one non-geminate and slower. In solar cell devices, the geminate mechanism decreases the quantum efficiency by about 40–50%. Recombination of the charge carriers in interfacial states is intensity independent and takes up to several 100 μs as the charges are trapped at different sites, not necessarily close to each other.

6.6 Comparison of samples

After our detailed analysis of the charge generation and loss mechanisms for the most efficient sample (Sample 1) in section 6.4 and 6.5, we now take a closer look at the less efficient samples introduced in section 6.2.2. We will see that charge-transfer state recombination on the sub 100 ps timescale is the main loss channel for all samples, and that an even greater proportion of CT state recombination in the chloroform-processed samples negates the theoretically possible quantum efficiency gain from the better PL quenching.

6.6.1 CT state recombination on the short timescale

To compare the different CT state generation and recombination dynamics after P(NDI2OD-T2) excitation, transient absorption experiments on the picosecond timescale were carried out. The samples were excited at 800 nm, the same excitation intensity was chosen for all samples. Figure 6.18(a) presents a comparison of the normalized kinetics of the P3HT bleach (525-550 nm). The same kinetics were already shown in figure 6.8 for Sample 1, and three time regions of interest, marked with A, B, and C, and dominated by charge transfer, CT state recombination, and decay of residual excitons respectively, were identified. Comparing that

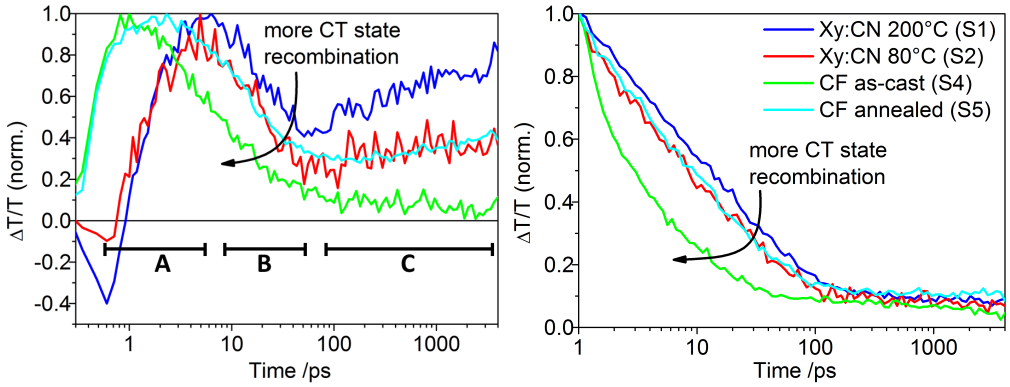

(a) P3HT bleach

(b) P(NDI2OD-T2) bleach

Figure 6.18: Comparison of the normalized kinetics for the P3HT bleach (525-550 nm) and the P(NDI2OD-T2) bleach (675-725 nm) after excitation at 800 nm for all four samples. In panel (a) the time regions of interest are marked with A, B, and C to enable comparison with figure 6.8.

with Sample 2, which was also spin-coated from a xylene:chloronaphthalene mixture, but dried at lower temperature, we find that the same regions can be identified. This is in agreement with a similar quenching efficiency for P(NDI2OD-T2) excitons in both samples as shown in table 6.2. The charge transfer kinetics in region A are the same for both samples. However, the kinetics are different in the time regions B and C. More CT state recombination leads to a greater drop in the P3HT bleach in the first 100 ps and it also overshadows more the signal rise due to exciton recombination in time region C. In the P(NDI2OD-T2) bleach region (see figure 6.18(b)), increased CT state recombination leads to a greater total amount of signal decay. We therefore conclude that more tightly bound charge-transfer states, which recombine on the sub-hundred picosecond timescale, and less free charges are generated from exciton quenching in this blend.

For the samples spin coated from chloroform, Sample 4 and 5, the exciton quenching is different. For both samples a PL quenching efficiency around 90% was observed after P(NDI2OD-T2) excitation (compare table 6.2). The quenching is also much faster, which can be determined from the kinetics in figure 6.18(a), where the P3HT bleach is at its maximum already after 1 ps for S4 and 2 ps

for S5. This indicates that the domains are much smaller or less pure in the chloroform-cast blends. Charge-transfer state recombination on the sub 100 ps timescale is also evident for S4 and S5, and the amount of recombination found on that timescale compares well with the efficiencies, with S4 having less than 10% signal left after 100 ps. Moreover, no rise of the P3HT bleach is found for Sample 4, indicating that the excitons are quenched much faster than in the other samples. The fast charge-transfer state recombination in Sample 4 is also seen in the dynamics of the P(NDI2OD-T2) bleach, shown in figure 6.18(b). For all four samples, only little signal is left after 1 ns as the P(NDI2OD-T2) bleach is overlaid by a photoinduced absorption from charges on P3HT.

6.6.2 Free charges and interfacial states on the long timescale

Having established that the amount of charge-transfer state recombination on the sub 100 ps timescale correlates with the efficiencies of the 4 samples, we now turn to look at the longer timescale to investigate whether recombination processes of free charges differ. As all samples have overlapping bleach and PIA signals, we carried out MCR-ALS analysis, as described in section 6.5.1 for Sample 1. We found that for all samples, two species were sufficient to describe the dataset, and show our best estimates of their actual spectra in the left panels of figure 6.19. Identical to the results for Sample 1, one species was found to have an intensity dependent rise time and an intensity independent decay while the other species exhibited an intensity dependent decay. The panels on the right of figure 6.19 show a comparison of the kinetics for each species for the same fluence. The kinetics of the formation and recombination of the interfacial state, as shown in the upper panel, is very similar for all 4 samples. A fraction of the free charge carriers, however, seem to live distinctly longer in Sample 1, as shown in the lower panel. This could also contribute slightly to the higher efficiency of Sample 1 and is consistent with the high fill factor.

We observe that the spectra of the species change between the samples. In the next section we look closely at these spectra to see what they imply about the charge generating interfaces.

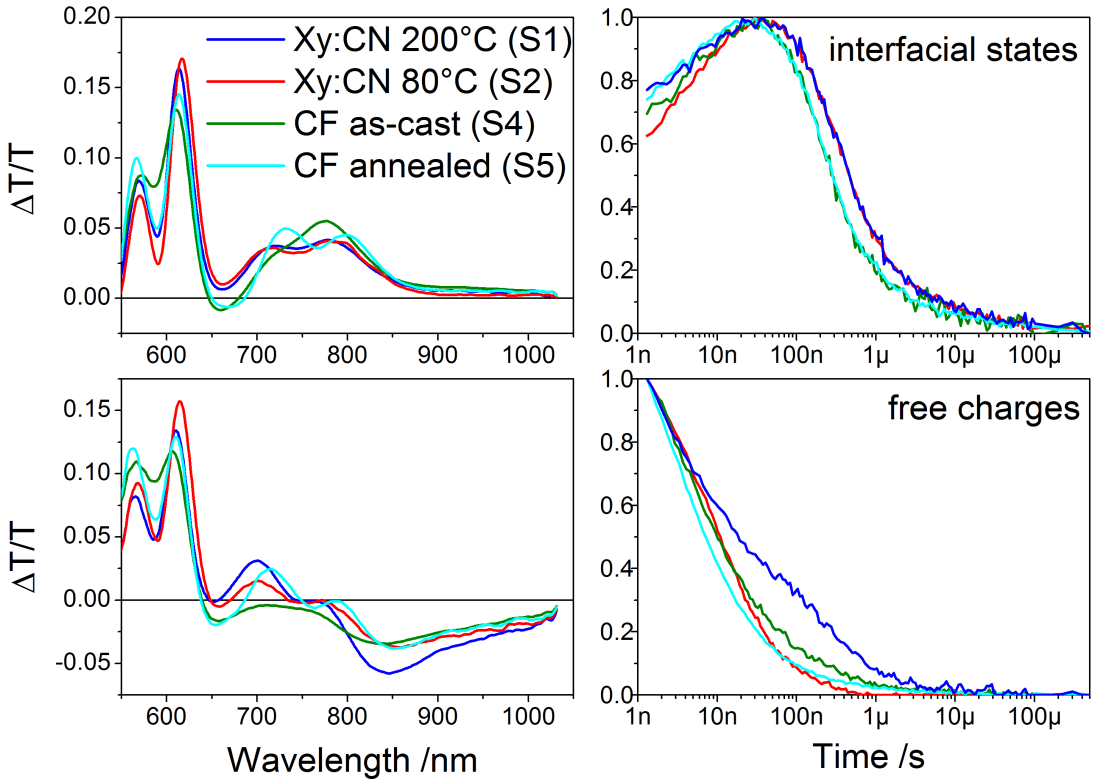

Figure 6.19: Comparison of the spectra and kinetics obtained from MCR analysis for all four samples. The upper panels show the spectra of the long-lived interfacial states and the corresponding kinetics, the lower panels show the spectra of the free charges and their population evolution (fluence: 950 nJ).

6.7 Structure of the interfacial region

Having discussed the recombination mechanisms that are responsible for the low photocurrent in the P3HT:P(NDI2OD-T2) devices, we now want to take a closer look at the spectra of charge and interfacial state which are present on the longer timescale. As we will see, these spectra contain information about the structure of the interface which we can correlate with information from scattering-based structural characterization experiments.

6.7.1 Stark effect influencing TA spectra

The spectra obtained for the long-lived states from MCR-ALS analysis (shown in the left panels of figure 6.19) exhibit features that cannot be explained by simple absorption bleaches. For example, the P(NDI2OD-T2) absorption bleach does not exhibit a broad bleach feature centered around 700 nm as we would expect from the absorption (see figure 6.4) but a two peak structure with maxima around 720 and 780 nm. Similar observations can be made for the P3HT bleach, which also displays a two peak structure with the peaks somewhat red shifted compared to the absorption. Comparing these spectral features with the first derivative of the blend's absorption spectrum reveals good agreement, as shown in figure 6.20. The spectral features of the absorption bleach of the interfacial state and the charge spectrum shown in the uppermost panels are also features of the first derivative of the absorption spectrum shown in the third panel.

Due to its donor-acceptor character with a high partial charge transfer in the excited state, P(NDI2OD-T2) has a large transition dipole moment $\Delta\vec{\mu}$. As discussed in section 2.1.5 (see page 14) the change in transmission $\Delta T/T$ of a species is proportional to the first derivative of its absorption (neglecting potential shifts in oscillator strength) in case of a linear Stark effect with aligned $\Delta\vec{\mu}$ and field. In the present case, the field is a photo-induced field, i.e. the field is due to charges on the donor and acceptor domains. Figure 6.20 shows how we can analyze the influence of the Stark effect in detail. We fit the $\Delta T/T$ spectrum with a weighted addition of the absorption, and its first and second derivative. The second derivative accounts for a random orientation of the transition dipole moments with respect to the field. Thus we obtain the contribution of each of these spectra to the $\Delta T/T$ spectrum. For the charge spectrum we add a Gaussian to represent the negative PIA feature. The quality of the fit is shown in figure 6.21 where the $\Delta T/T$ spectrum is compared to the sum of the weighted absorption and its derivatives for all samples. We find that the spectral features are well represented by the fit.

In conclusion, the ground-state bleach feature of the charge and interfacial state spectra always contain a strong contribution from the first derivative of the absorption spectrum. This leads to the conclusion that the polymer chains in

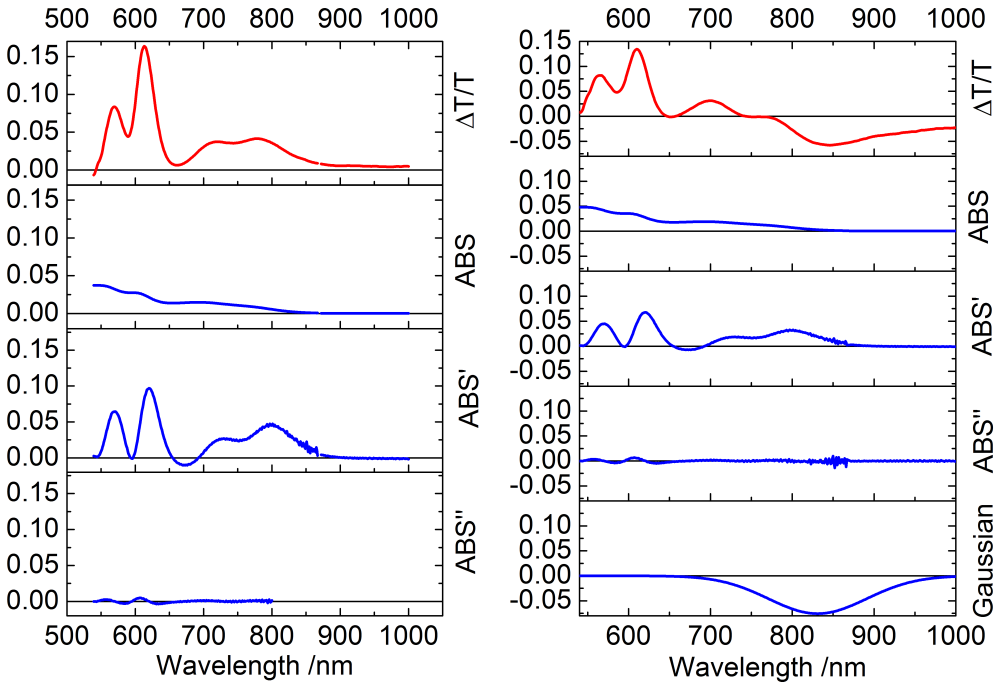

(a) interfacial states

(b) free charges

Figure 6.20: Demonstration of the influence of the Stark effect on the spectral shape of (a) interfacial states and (b) free charges for Sample 1. The spectrum of the species (shown in red in the uppermost panel) is fitted with contributions of the absorption of the blend and its first and second derivative. For the charge a Gaussian is added to represent the PIA.

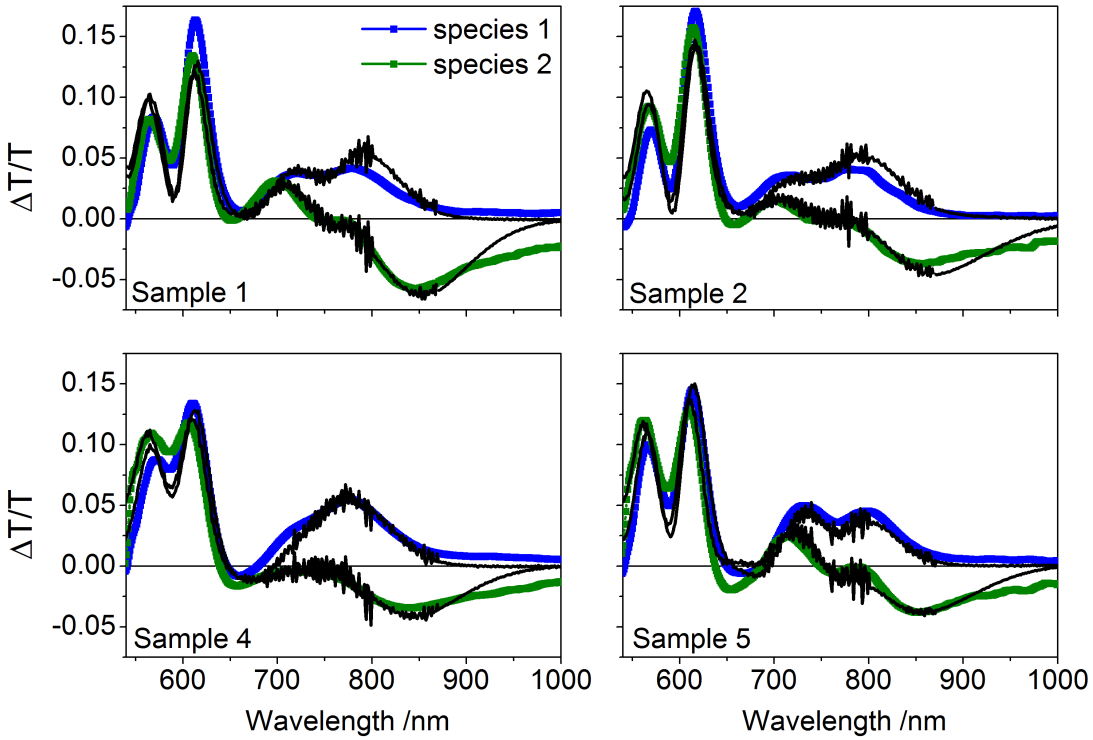

Figure 6.21: Comparison of the spectra of interfacial states (species 1, blue dotted line) and charges (species 2, green dotted line) with the fits (black solid lines) obtained by adding the respective absorption spectrum and its first and second derivative. For the charges a Gaussian is additionally added to represent the PIA. For all four samples the main features are well represented by the fit.

the interfacial regions always have some net alignment relative to the interface such that the transition dipole moment of the chromophore is anti-parallel to the photoinduced electric field. Only a small contribution of the second derivative is found, therefore only few long-lived states are found in randomly oriented interfacial areas. Similar contributions of the first and second derivative are found for all four samples. This indicates that the nanoscale morphology of the interfacial area where long-lived states are formed is similar for all samples. However, as the efficiencies of the samples are very different, the amount of this charge-forming interfacial area could certainly vary between the samples, which would account for the change in efficiency. From this data we conclude with

evidence for the hypothesis that free charge carriers are only generated at specific interfacial areas with a net ordering of the polymers with respect to the interface.

6.7.2 Interfacial structure revealed by GIWAXS

In order to understand the charge generation process in terms of the nanoscale morphology, grazing-incidence wide-angle X-ray scattering measurements (GIWAXS) and resonant soft X-ray scattering measurements (RSOXS) were carried out by Brian Collins in the group of Harald Ade at North Carolina State University. From the analysis of this X-ray data, conclusions about the molecular packing structure and the size and orientation of the P3HT and P(NDI2OD-T2) crystallites can be drawn. A schematic representation of the morphology obtained from that analysis on the most efficient sample is shown in figure 6.22. Excitons are generated in both crystalline and amorphous parts of P3HT and P(NDI2OD-T2). If the exciton is formed in an amorphous part, a strongly bound CT state is created that decays on the sub-hundred picosecond timescale due to the lack of driving force for the dissociation. Also, Förster Resonant Energy Transfer (FRET) of the exciton onto an aggregated P(NDI2OD-T2) can take place. This is called exciton self-trapping,[144] as the exciton cannot leave the aggregated region and undergo charge transfer. Efficient charge generation takes place in regions where P3HT and P(NDI2OD-T2) are oriented with their polymer backbone towards the heterojunction. Here, exciton dissociation is facilitated by the energy gradient between the amorphous and the crystalline regions and further charge separation occurs due to a fast charge delocalization along the $\pi - \pi$ stacking direction.

The same analysis of data obtained by GIWAXS measurements was carried out on the less efficient samples. For the chloroform cast sample (Sample 4) it was found that both P3HT and P(NDI2OD-T2) prefer a face-on orientation relative to the substrate. Annealing the sample results in P3HT being oriented edge-on, while P(NDI2OD-T2) remains face-on (Sample 5). For Sample 2 the orientation of P3HT is both edge-on and face-on, and also the orientation of P(NDI2OD-T2) is less clearly edge-on than in Sample 1.

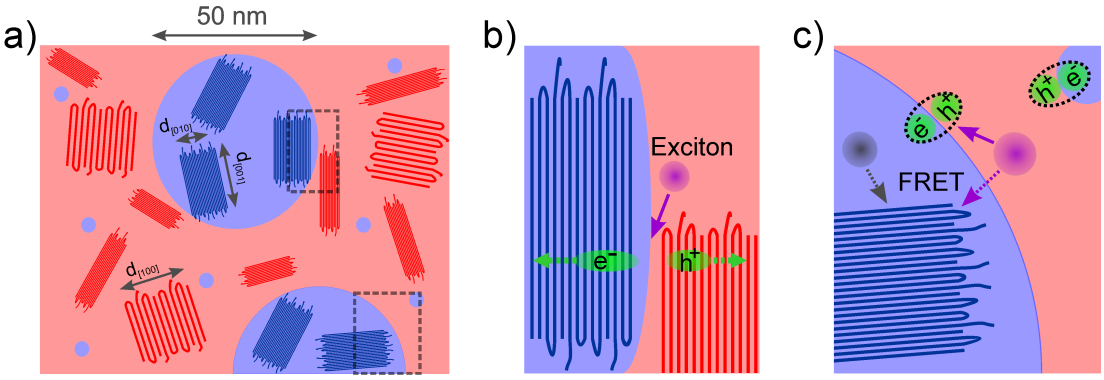

Figure 6.22: Panel a) illustrates the morphology as obtained from GIWAXS, TEM and RSOXS measurements for the most efficient sample. A cross-section in plane with the substrate is shown; blue colors depict P(NDI2OD-T2), red colors depict P3HT. Both amorphous domains (lighter colors) and crystalline areas (darker colors) are present in both materials. Circular P(NDI2OD-T2) domains, about 50 nm in diameter, are embedded in a P3HT matrix. While the P(NDI2OD-T2) domain is pure, small P(NDI2OD-T2) fractions are found in the P3HT domain (blue dots). For P3HT, crystals oriented face-on and edge-on relative to the substrate are found; the face-on crystals having a five times larger lattice spacing compared to the edge-on crystals. Magnifications of two regions (marked with black dashed boxes in a)) are shown in panel b) and c). Panel b) shows a region of charge generation where the P(NDI2OD-T2) and P3HT crystals are oriented with their polymer backbone towards the heterojunction (face-to-face relative to each other, but edge-on relative to the substrate). Panel c) depicts the self-trapping of an exciton (shown in dark blue) on a P(NDI2OD-T2) crystal after Förster Resonant Energy Transfer (FRET) from a disordered region. Charge-transfer state formation after P3HT excitation (shown in pink) in amorphous domains leads to strongly bound CT states that decay on the sub-hundred picosecond timescale. Figure reproduced from [145].

These results found with GIWAXS measurements agree well with our analysis of the Stark-effect influenced spectra presented in the previous section. Both methods lead to the conclusion that an ordered heterojunction is necessary for efficient free charge generation. Moreover, P3HT and P(NDI2OD-T2) need to be ordered with a particular relative orientation, i.e. face-to-face, to enable charge separation. Excitons formed in amorphous regions lead to strongly bound CT states which recombine quickly. Thus, the structure of the interface is the key determining factor to whether free charges or CT states are formed. A comparison of the different orientations between the four samples confirms these conclusions. Samples 2, 4 and 5 contain less of the charge generating interface where P3HT and P(NDI2OD-T2) are oriented face-to-face and therefore exhibit much more sub 100 ps charge-transfer state recombination. Charge transport is also affected by the anisotropy of the oriented crystals. Motion towards and away from the interface tends to be fast, however, lateral motion along the interface for recombination is slow. These results marks a crucial difference to bulk heterojunction solar cells containing a small molecule fullerene (derivative) as an electron acceptor. Fullerenes are isotropic molecules, i.e. they do not have a preferred orientation concerning efficient charge separation and charge transport. This diminishes the role of the interfacial morphology, however mesoscale morphology optimization plays an important role for fullerene containing solar cells as well.

6.8 Conclusions

In this chapter we have studied the charge generation and recombination processes in the polymer-polymer blend P3HT:P(NDI2OD-T2) in order to determine the reason for its low quantum efficiency in solar cell devices. Four samples with different processing conditions were investigated. The photophysical processes that occur after photo-excitation of either P3HT or P(NDI2OD-T2) are schematically shown in figure 6.23. We found that about half of the excitons generated in the P(NDI2OD-T2) phase decay before they are quenched at an interface, which constitutes an important loss channel. However, the main loss channel in P3HT:P(NDI2OD-T2) blends is charge-transfer state recombination on the sub 100 ps timescale, which accounts for a quantum efficiency loss of more than 70%

after either P3HT or P(NDI2OD-T2) excitation even in the most efficient sample. The charge carriers that are left after 100 ps can hop back to the interface and create interfacial states that can be observed due to their absorption bleach in the near infrared. About 40–50% of the interfacial bleach arises in less than 5 ns, independent of the fluence, while the other 50–60% of the interfacial bleach takes around 100 ns to arise at low intensities. Thus the quantum efficiency of a solar cell is decreased by another 40–50% through recombination of interfacial states geminately reformed from mobile charge carriers. However, the free charge carriers that are formed are efficiently extracted almost independently of field as their lifetime (>100 ns) is significantly longer than the solar cell transit time (~30 ns) leading to a high fill factor.

An analysis of the spectra of the long-lived states with respect to Stark effects reveals that these states are formed on polymer chains which exhibit a net alignment relative to the interface such that the transition dipole moment of the chromophore is anti-parallel to the photoinduced electric field. In agreement with that, structural measurements indicate that face-to-face orientation of the P3HT and P(NDI2OD-T2) crystallites at the heterojunction interface is beneficial for free charge generation.

The main difference between the samples with different processing conditions is found in the amount of CT state recombination on the sub 100 ps timescale. Combining photophysical with structural characterization experiments we can show that this is due to a smaller amount of face-to-face orientation at the interface.

Therefore, we establish that in polymer-polymer solar cells the heterojunction interface is a crucial point to be optimized. This is in contrast to fullerenes which are isotropic and therefore allow charge generation and charge transport independent of their orientation towards P3HT. In this case, morphology optimization in terms of phase separation and crystallinity is sufficient. However, in P3HT:P(NDI2OD-T2) blends, the orientation and order of the polymer chains with respect to each other needs to be optimized carefully in addition to the mesoscale morphology optimization in order to control the loss mechanisms described.

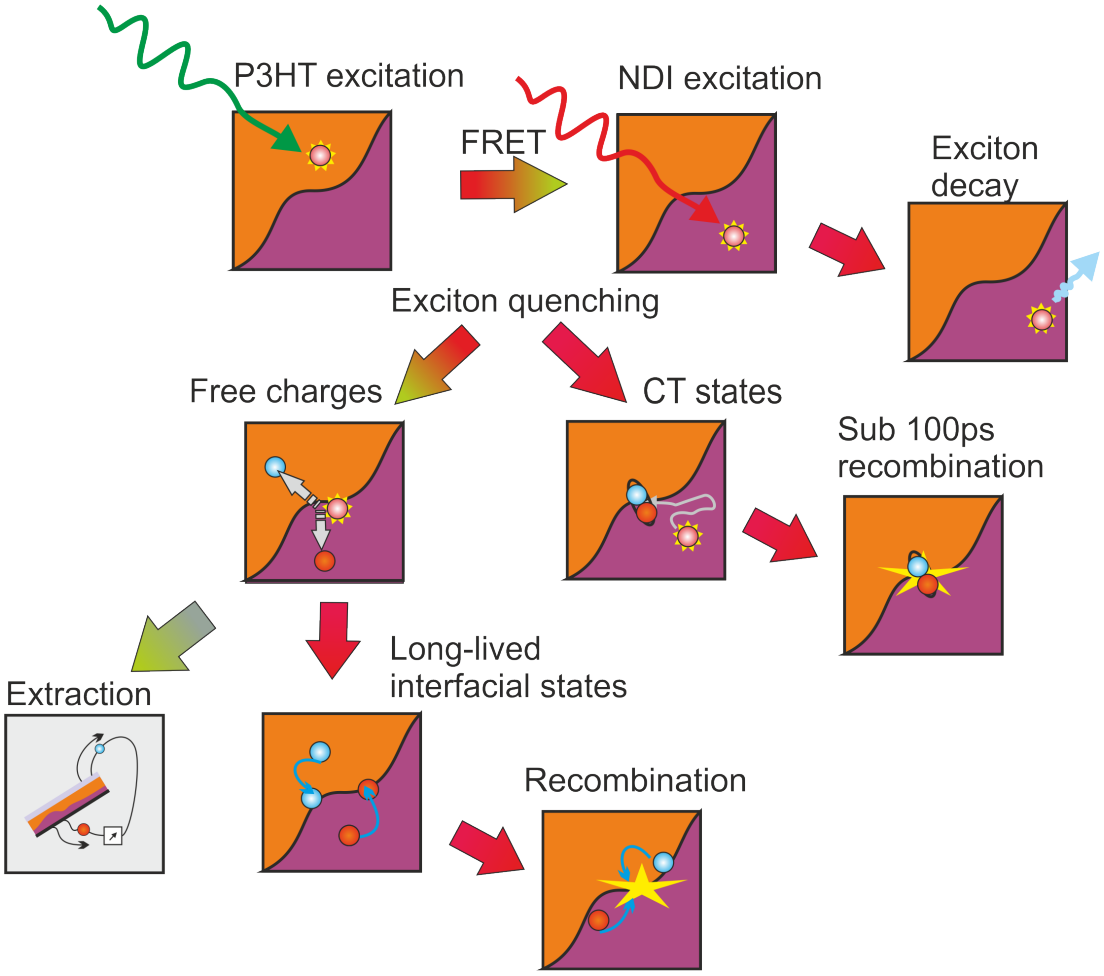

Figure 6.23: Summary of photophysical processes in P3HT:P(NDI2OD-T2) blends. The main loss processes are depicted on the right-hand side of the panel: exciton decay upon P(NDI2OD-T2) excitation, sub 100 ps CT state recombination and recombination through interfacial states.

Chapter 7

Conclusions

The record power conversion efficiency obtained with organic solar cells has increased dramatically over the last decade and has now reached the 10% threshold. [146, 147] However, further improvement is necessary to make organic solar cells a competitive renewable energy technology. To this end, understanding the charge carrier generation and loss processes and establishing structure-function relationships for the photoactive materials is essential.

This thesis investigates three different donor:acceptor systems in terms of their photophysical properties for the application as photoactive materials in organic solar cells. Each of these systems represents a different approach of optimizing materials in terms of light absorption over a broad wavelength range, efficient free charge carrier generation and fast charge carrier transport to obtain higher power conversion efficiencies. Using transient absorption spectroscopy we evaluate these approaches in terms of the charge carrier generation and recombination processes and reveal their virtues and limitations with respect to their application in the photoactive layer of organic solar cells.

In order to analyze transient absorption data, it is necessary to decompose an observed data matrix into the physically true concentration evolutions and spectra of a given number of excited states. We have discussed two techniques to do this: global analysis and a soft-modeling technique followed by an analysis of the linear transformations of the obtained factorization. When a system of equations for the population flows is not rigorously known, we have shown that this second method has very significant value. We have developed a technique

with which the bands of factorizations that satisfy the known physical properties of the system can be found, and the maximum physical insight extracted from the collected datasets without need for rigorous a-priori knowledge of the reaction kinetics. This is demonstrated for transient absorption experiments on the polymer:polymer samples with several overlapping signals, where we successfully obtain a physically reasonable decomposition of transient absorption data which enables us to understand the charge recombination processes.

In chapter 4 we have examined the approach to separate the absorption and the transport properties onto different monomer units of a terpolymer, in order to be able to optimize them separately. We find that it is possible to shuttle the hole from the chromophore unit onto a triarylamine introduced into the polymer backbone to enable the charge transport. This process takes place on a timescale of about 500 ps. However, the device performance deteriorates after the inclusion of the triarylamine, which we find is due to the triarylamine units acting as traps. This challenge could be overcome by designing polymers with hole transporting segments that have a strong tendency to pack and thus facilitate interchain hole transport.

Having shown that guiding excited state flow within the polymer backbone of a terpolymer is realizable, we take a closer look at ternary blend mixtures of an amorphous and a semi-crystalline polymer in chapter 5 to investigate whether the addition of an amorphous polymer aids the charge carrier separation. We find that the contrary is the case: geminate charge recombination on the early timescale is increased and is faster for the samples with increasing amorphous content. In addition to that, non-geminate recombination on the longer timescale also decreases the EQE and the fill factor of the samples with mainly amorphous polymer content. These results suggest that a semi-crystalline structure is required for efficient charge carrier separation.

Chapter 6 introduces a system where a polymer is used as an acceptor material, which exhibits enhanced absorption over the whole wavelength range and excellent charge carrier transport properties. Again, morphology is found to play an important role for the device performance. Sub 100 ps charge-transfer state recombination is the dominant loss mechanism in this system, as free charge carriers can only be generated at interfaces where donor and acceptor polymer are

oriented face-to-face relative to each other. Moreover, about 40–50% of the mobile charge carriers return to the interface as they have not fully escaped their mutual Coulomb attraction, forming interfacial states that recombine slowly as the charge carriers are trapped at different sites. For further development of polymer-polymer solar cells, an optimized control over the microscopic morphology and the crystallinity is required. This could be achieved with polymers with defined molecular weight and low polydispersity.

In conclusion, this thesis contributes to the understanding of photophysical processes in organic solar cells. This understanding and the resulting implications for further photoactive polymer development are important to fully exploit solar irradiation and to develop societally relevant applications of organic solar cells in the future.

References

[1] Intergovernmental Panel on Climate Change (IPCC). *Climate Change 2013: The Physical Science Basis. Working Group I Contribution to the IPCC 5th Assessment Report*, (September 2013).

[2] Dou, L., You, J., Hong, Z., Xu, Z., Li, G., Street, R. A., and Yang, Y. *Advanced Materials* , 10.1002/adma.201302563 (2013).

[3] Bundesministerium für Umwelt, Naturschutz und Reaktorsicherheit; Arbeitsgruppe Erneuerbare Energien-Statistik (AGEE-Stat), (October 2013).

[4] Krebs, F. C. *Solar Energy Materials and Solar Cells* **93**(4), 394 – 412 (2009).

[5] Krebs, F. C., Espinosa, N., Hösel, M., Søndergaard, R. R., and Jørgensen, M. *Advanced Materials* , 10.1002/adma.201302031 (2013).

[6] Li, J., Deng, X., Zhang, Z., Wang, Y., Liu, Y., He, K., Huang, Y., Tao, Q., Quan, L., and Zhu, W. *Journal of Polymer Science Part A: Polymer Chemistry* **50**, 4686–4694 (2012).

[7] Brabec, C. J., Sariciftci, N. S., and Hummelen, J. C. *Advanced Functional Materials* **11**(1), 15–26 (2001).

[8] He, Z., Zhong, C., Su, S., Xu, M., Wu, H., and Cao, Y. *Nature Photonics* **6**(9), 591–595 (2012).

[9] You, J., Chen, C.-C., Hong, Z., Yoshimura, K., Ohya, K., Xu, R., Ye, S., Gao, J., Li, G., and Yang, Y. *Advanced Materials* **25**(29), 3973–3978 (2013).

[10] Liang, Y. and Yu, L. *Polymer Reviews* **50**(4), 454–473 (2010).

[11] Scharber, M., Mühlbacher, D., Koppe, M., Denk, P., Waldauf, C., Heeger, A., and Brabec, C. *Advanced Materials* **18**(6), 789–794 (2006).

[12] Howard, I. A. and Laquai, F. *Macromolecular Chemistry and Physics* **211**(19), 2063–2070 (2010).

[13] www.nobelprize.org, (16.5.2013).

[14] Shirakawa, H., Louis, E. J., MacDiarmid, A. G., Chiang, C. K., and Heeger, A. J. *Journal of the Chemical Society, Chemical Communications* , 578–580 (1977).

[15] Müllen, K. and Wegner, G. *Electronic Materials. The Oligomer Approach.* Wiley-VCH, (1998).

[16] Peierls, R. E. *Quantum theory of solids.* Clarendon Press, Oxford, (1955).

[17] Schwoerer, M. and Wolf, H. C. *Organic Molecular Solids.* Wiley-VCH Verlag, (2006).

[18] Scholes, G. D. and Rumbles, G. *Nature Materials* **5**(9), 683–696 (2006).

[19] Pope, M. and Swenberg, C. E. *Electronic Processes in Organic Crystals and Polymers.* Oxford University Press, (1999).

[20] http://de.wikipedia.org/wiki/Franck Condon-Prinzip, (16.5.2013).

[21] Valeur, B. *Molecular Fluorescence: Principles and Applications.* Wiley-VCH Verlag, (2001).

[22] Förster, T. *Annalen der Physik* **437**(1-2), 55–75 (1948).

[23] Dexter, D. L. *The Journal of Chemical Physics* **21**(5), 836–850 (1953).

[24] Stark, J. *Nature* **92**, 401 (1913).

[25] Boxer, S. G. *The Journal of Physical Chemistry B* **113**(10), 2972–2983 (2009).

[26] Bublitz, G. U. and Boxer, S. G. *Annual Review of Physical Chemistry* **48**(1), 213–242 (1997).

[27] Clarke, T. M. and Durrant, J. R. *Chemical Reviews* **110**(11), 6736–6767 (2010).

[28] Deibel, C. and Dyakonov, V. *Reports on Progress in Physics* **73**(9), 096401 (2010).

[29] Cowan, S. R., Banerji, N., Leong, W. L., and Heeger, A. J. *Advanced Functional Materials* **22**, 1116–1128 (2012).

[30] Banerji, N. *Journal of Materials Chemistry C* **1**, 3052–3066 (2013).

[31] Howard, I. A. *Loss Mechanisms in High Open-Circuit Voltage Organic Solar Cells*. PhD thesis, University of Cambridge, (2009).

[32] Markov, D., Amsterdam, E., Blom, P., Sieval, A., and Hummelen, J. *Journal of Physical Chemistry A* **109**(24), 5266–5274 (2005).

[33] Sariciftci, N. S., Smilowitz, L., Heeger, A. J., and Wudl, F. *Science* **258**(5087), 1474–1476 (1992).

[34] Menke, S. M. and Holmes, R. J. *Energy & Environmental Science* , 10.1039/C3EE42444H (2014).

[35] Bakulin, A. A., Hummelen, J. C., Pshenichnikov, M. S., and van Loosdrecht, P. H. M. *Advanced Functional Materials* **20**(10), 1653–1660 (2010).

[36] Howard, I. A., Mauer, R., Meister, M., and Laquai, F. *Journal of the American Chemical Society* **132**(42), 14866–14876 (2010).

[37] Hwang, I.-W., Soci, C., Moses, D., Zhu, Z., Waller, D., Gaudiana, R., Brabec, C., and Heeger, A. *Advanced Materials* **19**(17), 2307–2312 (2007).

[38] Brabec, C. J., Zerza, G., Cerullo, G., Silvestri, S. D., Luzzati, S., Hummelen, J. C., and Sariciftci, S. *Chemical Physics Letters* **340**(34), 232 – 236 (2001).

[39] Banerji, N., Cowan, S., Leclerc, M., Vauthey, E., and Heeger, A. J. *Journal of the American Chemical Society* **132**(49), 17459–17470 (2010).

[40] Jamieson, F. C., Domingo, E. B., McCarthy-Ward, T., Heeney, M., Stingelin, N., and Durrant, J. R. *Chemical Science* **3**, 485–492 (2012).

[41] Faist, M. A., Kirchartz, T., Gong, W., Ashraf, R. S., McCulloch, I., de Mello, J. C., Ekins-Daukes, N. J., Bradley, D. D. C., and Nelson, J. *Journal of the American Chemical Society* **134**(1), 685–692 (2012).

[42] Tvingstedt, K., Vandewal, K., Gadisa, A., Zhang, F., Manca, J., and Inganäs, O. *Journal of the American Chemical Society* **131**(33), 11819–11824 (2009).

[43] Sreearunothai, P., Morteani, A. C., Avilov, I., Cornil, J., Beljonne, D., Friend, R. H., Phillips, R. T., Silva, C., and Herz, L. M. *Physical Review Letters* **96**, 117403 (2006).

[44] Bakulin, A. A., Rao, A., Pavelyev, V. G., van Loosdrecht, P. H. M., Pshenichnikov, M. S., Niedzialek, D., Cornil, J., Beljonne, D., and Friend, R. H. *Science* **335**(6074), 1340–1344 (2012).

[45] Grancini, G., Maiuri, M., Fazzi, D., Petrozza, A., Egelhaaf, H.-J., Brida, D., Cerullo, G., and Lanzani, G. *Nature Materials* **12**, 29–33 (2013).

[46] Liang, Y., Xu, Z., Xia, J., Tsai, S.-T., Wu, Y., Li, G., Ray, C., and Yu, L. *Advanced Materials* **22**(20), E135–E138 (2010).

[47] Treat, N. D., Brady, M. A., Smith, G., Toney, M. F., Kramer, E. J., Hawker, C. J., and Chabinyc, M. L. *Advanced Energy Materials* **1**(1), 82–89 (2011).

[48] Collins, B. A., Gann, E., Guignard, L., He, X., McNeill, C. R., and Ade, H. *The Journal of Physical Chemistry Letters* **1**(21), 3160–3166 (2010).

[49] Guilbert, A. A. Y., Reynolds, L. X., Bruno, A., MacLachlan, A., King, S. P., Faist, M. A., Pires, E., Macdonald, J. E., Stingelin, N., Haque, S. A., and Nelson, J. *ACS Nano* **6**(5), 3868–3875 (2012).

[50] Ma, W., Tumbleston, J. R., Wang, M., Gann, E., Huang, F., and Ade, H. *Advanced Energy Materials* **3**(7), 864–872 (2013).

[51] Ma, W., Yang, C., Gong, X., Lee, K., and Heeger, A. *Advanced Functional Materials* **15**(10), 1617–1622 (2005).

[52] Mihailetchi, V., Xie, H., deBoer, B., Koster, L., and Blom, P. *Advanced Functional Materials* **16**(5), 699–708 (2006).

[53] Arkhipov, V. I., Heremans, P., and Bässler, H. *Applied Physics Letters* **82**(25), 4605–4607 (2003).

[54] Hodgkiss, J. M., Albert-Seifried, S., Rao, A., Barker, A. J., Campbell, A. R., Marsh, R. A., and Friend, R. H. *Advanced Functional Materials* **22**(8), 1567–1577 (2012).

[55] Mauer, R., Howard, I. A., and Laquai, F. *The Journal of Physical Chemistry Letters* **2**(14), 1736–1741 (2011).

[56] Kniepert, J., Schubert, M., Blakesley, J. C., and Neher, D. *The Journal of Physical Chemistry Letters* **2**(7), 700–705 (2011).

[57] Albrecht, S., Schindler, W., Kurpiers, J., Kniepert, J., Blakesley, J. C., Dumsch, I., Allard, S., Fostiropoulos, K., Scherf, U., and Neher, D. *The Journal of Physical Chemistry Letters* **3**(5), 640–645 (2012).

[58] Jaiswal, M. and Menon, R. *Polymer International* **55**(12), 1371–1384 (2006).

[59] Bässler, H. *physica status solidi (b)* **175**(1), 15–56 (1993).

[60] Blom, P. W. M., de Jong, M. J. M., and van Munster, M. G. *Physical Review B* **55**, R656–R659 (1997).

[61] Miller, A. and Abrahams, E. *Physical Review* **120**, 745–755 (1960).

[62] Coropceanu, V., Cornil, J., da Silva Filho, D. A., Olivier, Y., Silbey, R., and Brédas, J.-L. *Chemical Reviews* **107**(4), 926–952 (2007).

[63] Langevin, P. *Annales De Chimie Et De Physique* **28**, 433 (1903).

[64] Deibel, C., Baumann, A., and Dyakonov, V. *Applied Physics Letters* **93**(16), 163303 (2008).

[65] Juška, G., Arlauskas, K., Stuchlik, J., and Österbacka, R. *Journal of Non-Crystalline Solids* **352**, 1167 – 1171 (2006).

[66] Clark, J., Chang, J.-F., Spano, F. C., Friend, R. H., and Silva, C. *Applied Physics Letters* **94**(16), 163306 (2009).

[67] Shuttle, C. G., O'Regan, B., Ballantyne, A. M., Nelson, J., Bradley, D. D. C., de Mello, J., and Durrant, J. R. *Applied Physics Letters* **92**(9), 093311 (2008).

[68] Shuttle, C. G., Hamilton, R., Nelson, J., O'Regan, B. C., and Durrant, J. R. *Advanced Functional Materials* **20**(5), 698–702 (2010).

[69] Juška, G., Genevičius, K., Nekrašas, N., Sliaužys, G., and Österbacka, R. *Applied Physics Letters* **95**(1), 013303 (2009).

[70] Nelson, J., Choulis, S. A., and Durrant, J. R. *Thin Solid Films* **451-452**, 508 – 514 (2004).

[71] Turchinovich, D. *Lecture Ultrafast Phenomena*, (April 2013).

[72] Keller, U. *Nature* **424**(6950), 831–838 (2003).

[73] Bradler, M., Baum, P., and Riedle, E. *Applied Physics B* **97**(3), 561–574 (2009).

[74] Menzel, R. *Photonics*. Springer, (2007).

[75] Cabanillas-Gonzalez, J., Grancini, G., and Lanzani, G. *Advanced Materials* **23**(46), 5468–5485 (2011).

[76] van Wilderen, L. J. G. W., Lincoln, C. N., and van Thor, J. J. *PLoS ONE* **6**(3), e17373 03 (2011).

[77] de Juan, A., Maeder, M., Martinez, M., and Tauler, R. *Chemometrics and Intelligent Laboratory Systems* **54**(2), 123 – 141 (2000).

[78] Jaumot, J., Gargallo, R., de Juan, A., and Tauler, R. *Chemometrics and Intelligent Laboratory Systems* **76**(1), 101 – 110 (2005).

[79] de Juan, A. and Tauler, R. *Analytica Chimica Acta* **500**, 195 – 210 (2003).

[80] de Juan, A. and Tauler, R. *Critical Reviews in Analytical Chemistry* **36**(3-4), 163–176 (2006).

[81] Burkhard, G. F., Hoke, E. T., and McGehee, M. D. *Advanced Materials* **22**(30), 3293–3297 (2010).

[82] Peumans, P., Yakimov, A., and Forrest, S. R. *Journal of Applied Physics* **93**(7), 3693–3723 (2003).

[83] Pettersson, L. A. A., Roman, L. S., and Inganäs, O. *Journal of Applied Physics* **86**(1), 487–496 (1999).

[84] McNeill, C. R., Hwang, I., and Greenham, N. C. *Journal of Applied Physics* **106**(2), 024507 (2009).

[85] Hwang, I., McNeill, C. R., and Greenham, N. C. *Journal of Applied Physics* **106**(9), 094506 (2009).

[86] Meister, M. *Charge Generation and Recombination in Hybrid Organic/Inorganic Solar Cells*. PhD thesis, Johannes-Gutenberg-Universität Mainz, (2013).

[87] Mangold, H., Howard, I. A., Janietz, S., and Laquai, F. *Applied Physics Letters* **101**(23), 231104 (2012).

[88] Dennler, G., Scharber, M. C., and Brabec, C. J. *Advanced Materials* **21**(13), 1323–1338 (2009).

[89] Kim, Y., Cook, S., Tuladhar, S. M., Choulis, S. A., Nelson, J., Durrant, J. R., Bradley, D. D. C., Giles, M., McCulloch, I., Ha, C.-S., and Ree, M. *Nature Materials* **5**(3), 197–203 (2006).

[90] He, Z., Zhong, C., Huang, X., Wong, W.-Y., Wu, H., Chen, L., Su, S., and Cao, Y. *Advanced Materials* **23**(40), 4636–4643 (2011).

[91] Zhou, H., Yang, L., and You, W. *Macromolecules* **45**(2), 607–632 (2012).

[92] Bundgaard, E. and Krebs, F. C. *Solar Energy Materials and Solar Cells* **91**(11), 954 – 985 (2007).

[93] Kularatne, R. S., Magurudeniya, H. D., Sista, P., Biewer, M. C., and Stefan, M. C. *Journal of Polymer Science Part A: Polymer Chemistry* **51**(4), 743–768 (2012).

[94] Zhou, H., Yang, L., Stuart, A. C., Price, S. C., Liu, S., and You, W. *Angewandte Chemie International Edition* **50**(13), 2995–2998 (2011).

[95] Chu, T.-Y., Lu, J., Beaupr, S., Zhang, Y., Pouliot, J.-R., Wakim, S., Zhou, J., Leclerc, M., Li, Z., Ding, J., and Tao, Y. *Journal of the American Chemical Society* **133**(12), 4250–4253 (2011).

[96] Price, S. C., Stuart, A. C., Yang, L., Zhou, H., and You, W. *Journal of the American Chemical Society* **133**(12), 4625–4631 (2011).

[97] Amb, C. M., Chen, S., Graham, K. R., Subbiah, J., Small, C. E., So, F., and Reynolds, J. R. *Journal of the American Chemical Society* **133**(26), 10062–10065 (2011).

[98] Dou, L., You, J., Yang, J., Chen, C.-C., He, Y., Murase, S., Moriarty, T., Emery, K., Li, G., and Yang, Y. *Nature Photonics* **6**(3), 180–185 (2012).

[99] Nelson, J. *The Physics of Solar Cells*. Imperial College Press, (2003).

[100] Uy, R. L., Price, S. C., and You, W. *Macromolecular Rapid Communications* **33**(14), 1162–1177 (2012).

[101] Laquai, F. and Hertel, D. *Applied Physics Letters* **90**(14), 142109 (2007).

[102] Laquai, F., Wegner, G., Im, C., Bässler, H., and Heun, S. *Journal of Applied Physics* **99**(2), 023712 (2006).

[103] Zhang, W., Smith, J., Hamilton, R., Heeney, M., Kirkpatrick, J., Song, K., Watkins, S. E., Anthopoulos, T., and McCulloch, I. *Journal of the American Chemical Society* **131**(31), 10814–10815 (2009).

[104] Zhang, F., Mammo, W., Andersson, L., Admassie, S., Andersson, M., and Inganäs, O. *Advanced Materials* **18**(16), 2169–2173 (2006).

[105] Gadisa, A., Mammo, W., Andersson, L., Admassie, S., Zhang, F., Andersson, M., and Inganäs, O. *Advanced Functional Materials* **17**(18), 3836–3842 (2007).

[106] Mammo, W., Admassie, S., Gadisa, A., Zhang, F., Inganäs, O., and Andersson, M. R. *Solar Energy Materials and Solar Cells* **91**(11), 1010 – 1018 (2007).

[107] von Hauff, E., Dyakonov, V., and Parisi, J. *Solar Energy Materials and Solar Cells* **87**, 149 – 156 (2005).

[108] Persson, N.-K., Sun, M., Kjellberg, P., Pullerits, T., and Inganäs, O. *The Journal of Chemical Physics* **123**(20), 204718 (2005).

[109] Etzold, F., Howard, I. A., Mauer, R., Meister, M., Kim, T.-D., Lee, K.-S., Baek, N. S., and Laquai, F. *Journal of the American Chemical Society* **133**(24), 9469–9479 (2011).

[110] Yang, X., Loos, J., Veenstra, S. C., Verhees, W. J. H., Wienk, M. M., Kroon, J. M., Michels, M. A. J., and Janssen, R. A. J. *Nano Letters* **5**(4), 579–583 (2005).

[111] Sirringhaus, H., Brown, P., Friend, R., Nielsen, M., Bechgaard, K., Langeveld-Voss, B., Spiering, A., Janssen, R., Meijer, E., Herwig, P., and de Leeuw, D. *Nature* **401**(6754), 685–688 (1999).

[112] McCulloch, I., Heeney, M., Bailey, C., Genevicius, K., MacDonald, I., Shkunov, M., Sparrowe, D., Tierney, S., Wagner, R., Zhang, W., Chabinyc, M. L., Kline, R. J., McGehee, M. D., and Toney, M. F. *Nature Materials* **5**(4), 328–333 (2006).

[113] Kiriy, N., Jhne, E., Adler, H.-J., Schneider, M., Kiriy, A., Gorodyska, G., Minko, S., Jehnichen, D., Simon, P., Fokin, A. A., and Stamm, M. *Nano Letters* **3**(6), 707–712 (2003).

[114] Moulé, A. and Meerholz, K. *Advanced Materials* **20**(2), 240–245 (2008).

[115] Padinger, F., Rittberger, R., and Sariciftci, N. *Advanced Functional Materials* **13**(1), 85–88 (2003).

[116] Hartmann, L., Tremel, K., Uttiya, S., Crossland, E., Ludwigs, S., Kayunkid, N., Vergnat, C., and Brinkmann, M. *Advanced Functional Materials* **21**(21), 4047–4057 (2011).

[117] Li, G., Shrotriya, V., Huang, J., Yao, Y., Moriarty, T., Emery, K., and Yang, Y. *Nature Materials* **4**(11), 864–868 (2005).

[118] Berson, S., DeBettignies, R., Bailly, S., and Guillerez, S. *Advanced Functional Materials* **17**(8), 1377–1384 (2007).

[119] Ohkita, H., Cook, S., Astuti, Y., Duffy, W., Tierney, S., Zhang, W., Heeney, M., McCulloch, I., Nelson, J., Bradley, D. D. C., and Durrant, J. R. *Journal of the American Chemical Society* **130**(10), 3030–3042 (2008).

[120] Westacott, P., Tumbleston, J. R., Shoaee, S., Fearn, S., Bannock, J. H., Gilchrist, J. B., Heutz, S., deMello, J., Heeney, M., Ade, H., Durrant, J., McPhail, D. S., and Stingelin, N. *Energy & Environmental Science* **6**, 2756–2764 (2013).

[121] Jiang, X., Österbacka, R., Korovyanko, O., An, C., Horovitz, B., Janssen, R., and Vardeny, Z. *Advanced Functional Materials* **12**(9), 587–597 (2002).

[122] Campoy-Quiles, M., Kanai, Y., El-Basaty, A., Sakai, H., and Murata, H. *Organic Electronics* **10**(6), 1120 – 1132 (2009).

[123] Kästner, C., Rathgeber, S., Egbe, D. A. M., and Hoppe, H. *Journal of Materials Chemistry A* **1**, 3961–3969 (2013).

[124] Egbe, D. A. M., Türk, S., Rathgeber, S., Kühnlenz, F., Jadhav, R., Wild, A., Birckner, E., Adam, G., Pivrikas, A., Cimrova, V., Knör, G., Sariciftci, N. S., and Hoppe, H. *Macromolecules* **43**(3), 1261–1269 (2010).

[125] Rathgeber, S., Bastos de Toledo, D., Birckner, E., Hoppe, H., and Egbe, D. A. M. *Macromolecules* **43**(1), 306–315 (2010).

[126] Guo, J., Ohkita, H., Benten, H., and Ito, S. *Journal of the American Chemical Society* **132**(17), 6154–6164 (2010).

[127] Etzold, F., Howard, I. A., Forler, N., Cho, D. M., Meister, M., Mangold, H., Shu, J., Hansen, M. R., Müllen, K., and Laquai, F. *Journal of the American Chemical Society* **134**(25), 10569–10583 (2012).

[128] Sonar, P., Fong Lim, J. P., and Chan, K. L. *Energy & Environmental Science* **4**(5), 1558–1574 (2011).

[129] Facchetti, A. *Chemistry of Materials* **23**(3), 733–758 (2011).

[130] Chochos, C. L., Tagmatarchis, N., and Gregoriou, V. G. *RSC Advances* **3**, 7160–7181 (2013).

[131] Zhou, E., Cong, J., Wei, Q., Tajima, K., Yang, C., and Hashimoto, K. *Angewandte Chemie International Edition* **50**(12), 2799–2803 (2011).

[132] He, X., Gao, F., Tu, G., Hasko, D., Hüttner, S., Steiner, U., Greenham, N. C., Friend, R. H., and Huck, W. T. S. *Nano Letters* **10**(4), 1302–1307 (2010).

[133] Mori, D., Benten, H., Kosaka, J., Ohkita, H., Ito, S., and Miyake, K. *ACS Applied Materials & Interfaces* **3**(8), 2924–2927 (2011).

[134] Holcombe, T. W., Norton, J. E., Rivnay, J., Woo, C. H., Goris, L., Piliego, C., Griffini, G., Sellinger, A., Brédas, J.-L., Salleo, A., and Fréchet, J. M. J. *Journal of the American Chemical Society* **133**(31), 12106–12114 (2011).

[135] McNeill, C. R., Abrusci, A., Zaumseil, J., Wilson, R., McKiernan, M. J., Burroughes, J. H., Halls, J. J. M., Greenham, N. C., and Friend, R. H. *Applied Physics Letters* **90**(19), 193506 (2007).

[136] http://www.polyera.com/, (24.7.2013).

[137] Yan, H., Chen, Z., Zheng, Y., Newman, C., Quinn, J. R., Dotz, F., Kastler, M., and Facchetti, A. *Nature* **457**(7230), 679–686 (2009).

[138] Yang, H., LeFevre, S. W., Ryu, C. Y., and Bao, Z. *Applied Physics Letters* **90**(17), 172116 (2007).

[139] Schubert, M., Dolfen, D., Frisch, J., Roland, S., Steyrleuthner, R., Stiller, B., Chen, Z., Scherf, U., Koch, N., Facchetti, A., and Neher, D. *Advanced Energy Materials* **2**(3), 369–380 (2012).

[140] Lee, J., Vandewal, K., Yost, S. R., Bahlke, M. E., Goris, L., Baldo, M. A., Manca, J. V., and Voorhis, T. V. *Journal of the American Chemical Society* **132**(34), 11878–11880 (2010).

[141] Benson-Smith, J., Goris, L., Vandewal, K., Haenen, K., Manca, J., Vanderzande, D., Bradley, D., and Nelson, J. *Advanced Functional Materials* **17**(3), 451–457 (2007).

[142] Vandewal, K., Tvingstedt, K., Gadisa, A., Inganäs, O., and Manca, J. V. *Nature Materials* **8**(11), 904–909 (2009).

[143] Steyrleuthner, R., Schubert, M., Howard, I., Klaumünzer, B., Schilling, K., Chen, Z., Saalfrank, P., Laquai, F., Facchetti, A., and Neher, D. *Journal of the American Chemical Society* **134**(0), 18303–18317 (2012).

[144] Fink, R. F., Seibt, J., Engel, V., Renz, M., Kaupp, M., Lochbrunner, S., Zhao, H.-M., Pfister, J., Würthner, F., and Engels, B. *Journal of the American Chemical Society* **130**(39), 12858–12859 (2008).

[145] Schubert, M., Collins, B. A., Mangold, H., Howard, I. A., Vandewal, K., Schindler, W., Roland, S., Behrends, J., Steyrleuthner, R., Chen, Z., Bittl,

R., Salleo, A., Facchetti, A., Laquai, F., Ade, H., and Neher, D. , submitted (2013).

[146] Scharber, M. and Sariciftci, N. *Progress in Polymer Science* **38**(12), 1929–1940 (2013).

[147] Green, M. A., Emery, K., Hishikawa, Y., Warta, W., and Dunlop, E. D. *Progress in Photovoltaics: Research and Applications* **21**(1), 1–11 (2013).

Nomenclature

$\Delta\vec{\mu}$	change in dipole moment
A	acceptor
AFM	atomic force microscopy
c	speed of light
CN	chloronaphthalene
CT	charge-transfer
D	donor
D-A	donor-acceptor
DOS	density of states
EFA	evolving factor analysis
EL	electroluminescence
EQE	external quantum efficiency
FF	fill factor
FRET	Förster resonant energy transfer
GIWAXS	grazing-incidence wide-angle X-ray scattering
GPC	gel permeation chromatography

GS	ground state
GSB	ground state bleach
HOMO	highest occupied molecular orbital
HTU	hole transport unit
I_{SC}	short circuit current
IC	internal conversion
IQE	internal quantum efficiency
IR	infrared
ISC	intersystem crossing
ITO	indium tin oxide
LED	light emitting diode
LUMO	lowest unoccupied molecular orbital
mpp	maximum power point
NIR	near infrared
OFET	organic field effect transistor
OLED	organic light emitting diode
OSC	organic solar cell
P3HT	poly(3-hexylthiophene)
PCBM	phenyl-C61-butyric acid methyl ester
PDI	perylenediimide
PDS	photothermal deflection spectroscopy
PIA	photoinduced absorption

PL	photoluminescence
PS	polystyrene
QE	quenching efficiency
RSOXS	resonant soft X-ray scattering
RT	room temperature
SE	stimulated emission
SSC	spatially separated charge carriers
SVD	Singular value decomposition
TA	transient absorption
TAA	triarylamine
TDCF	time-delayed collection field
TEM	transmission electron microscopy
V_{OC}	open circuit voltage
Xy	para-xylene

Appendix A

Publications and Conference Contributions

Scientific publications

Scientific publications presented in this work

H. Mangold, I. A. Howard, S. Janietz, F. Laquai, *Controlled energy shuttling in terpolymers enabling independent optimization of absorption and transport properties in organic solar cell materials*, Applied Physics Letters **2012**, 101, 231104.

M. Schubert, B. A. Collins, H. Mangold, I. A. Howard, K. Vandewal, W. Schindler, S. Roland, J. Behrends, R. Steyrleuthner, Z. Chen, K. Fostiropoulos, R. Bittl, A. Salleo, A. Facchetti, F. Laquai, H. Ade, D. Neher, *Correlated donor/acceptor crystal orientation and fast charge-transfer state recombination controls photocurrent generation in all-polymer solar cells*, submitted.

I. A. Howard, H. Mangold, F. Etzold, D. Gehrig, F. Laquai, *Transient absorption data analysis by soft-modeling*, chapter in *Ultrafast Dynamics in Molecules, Nanostructures and Interfaces*, Series in Optics and Photonics: Volume 8, World scientific.

Further scientific publications

P. Anant, H. Mangold, N. T. Lucas, F. Laquai, J. Jacob, *Synthesis and Characterization of Donor-Acceptor Type 4,4'-Bis(2,1,3-benzothiadiazole) based Copolymers*, Polymer **2011**, 52 (20), 4442-4450.

F. Etzold, I. A. Howard, N. Forler, D. M. Cho, M. Meister, H. Mangold, J. Shu, M. R. Hansen, K. Müllen, F. Laquai, *The Effect of Solvent Additives on Morphology and Excited-State Dynamics in PCPDTBT:PCBM Photovoltaic Blends*, Journal of the American Chemical Society **2012**, 134 (25), 10569-10583.

H. Mangold, T. Richter, S. Link, U. Würfel, S. Ludwigs, *Optoelectronic Properties of Hyperbranched Polythiophenes*, Journal of Physical Chemistry B **2012**, 116, 154-159.

Conference contributions

03/2011	Poster presentation at the annual meeting of the German Physical Society (DPG), Dresden, Germany
02/2012	Poster presentation at the Macromolecular Colloquium, Freiburg, Germany
03/2012	Poster presentation at the annual meeting of the DPG, Berlin, Germany
04/2012	Oral presentation at the MRS Spring Meeting, San Francisco, USA
03/2013	Poster presentation at the annual meeting of the DPG, Regensburg, Germany
05/2013	Oral presentation at the International Conference on Hybrid and Organic Photovoltaics (HOPV), Sevilla, Spain
12/2013	Oral presentation at the MRS Fall Meeting, Boston, USA